July 2019

Flow-induced oscillations in floating offshore wind turbines

Daniel Carlson

FLOW-INDUCED OSCILLATIONS IN FLOATING OFFSHORE WIND TURBINES

A Dissertation Presented

by

DANIEL W. CARLSON

Submitted to the Graduate School of the
University of Massachusetts Amherst in partial fulfillment
of the requirements for the degree of

DOCTOR OF PHILOSOPHY

May 2019

Department of Mechanical and Industrial Engineering

FLOW-INDUCED OSCILLATIONS IN FLOATING OFFSHORE WIND TURBINES

A Dissertation Presented

by

DANIEL W. CARLSON

Approved as to style and content by:

Yahya Modarres-Sadeghi, Chair

David Schmidt, Member

Paul Sievert, Member

Sundar Krishnamurty, Department Head
Department of Mechanical and Industrial Engineering

ACKNOWLEDGMENTS

This work is partially supported by the NSF-sponsored IGERT: Offshore Wind Energy Engineering, Environmental Science, and Policy (Grant Number 1068864), and grants from the Massachusetts Clean Energy Center and US Department of Energy.

Over the years completing this work, I have received invaluable support and guidance from my advisor Professor Yahya Modarres–Sadeghi, and he has my deepest gratitude. His patience and wisdom has been paramount in both training and readying me for my ongoing career. It was also an honor to have Professor David Schmidt and Professor Paul Sievert serve on my dissertation committee. Their suggestions and feedback throughout this process has had a great impact on this thesis.

A special thank you to the undergraduate researchers who helped on both this work and the countless projects not discussed here, in particular Michael Andrick, Akhil Borra, Nicholas Capell, Gabrielle Little, Eric McManimon, Nicholas Robinson and Corinna Torabi, plus many others. Thanks also to Rick Winn and Al Rakouskas from the MIE department for helping to machine and instrument all the experiments.

I am also thankful for my numerous labmates including Banafsheh, Pariya, Gary, Suyue, Todd, Tyler, Bridget, and Pieter for their constant friendship and encouragement. You made this journey enjoyable, and it has been great seeing what we could make!

Last but not least, I would like to thank my family for their love and support, and my friends for reminding me who I am.

ABSTRACT

FLOW-INDUCED OSCILLATIONS IN FLOATING OFFSHORE WIND TURBINES

MAY 2019

DANIEL W. CARLSON

B.S.M.E., UNIVERSITY OF MASSACHUSETTS AMHERST

Ph.D., UNIVERSITY OF MASSACHUSETTS AMHERST

Directed by: Professor Yahya Modarres-Sadeghi

The goal of this thesis is to experimentally study the structural dynamics, wake interaction, and fluid forces on the multiple-degree of freedom systems typical of floating wind turbines. Vortex–surface alignment about flexibly-mounted prisms is studied to investigate the response of barges and semi-submersible hulls, and new results pertaining to the galloping response kink for a prism with dual inline–crossflow resonance is presented. Flow–induced oscillations of a spar model free to rotate in 3D space is replicated and observed as 2D figure–eight orbits about the center of the spar. Methods to suppress the flow from exciting the spar are proposed. The influence of mooring cable concavity is studied for a cylinder with crossflow–inline flexibility, and the effect of the axial tip on higher harmonic fluid forces is shown to have a significant reduction on the inline and crossflow oscillation components when concave. As a separate project, flow-induced oscillations are made beneficial to the operation of wind turbines via the study of larynx phonation to create an air-driven ultrasound generator for use as a bat deterrent on wind turbine blades.

CONTENTS

LIST OF TABLES

Table **Page**

LIST OF FIGURES

Figure **Page**

CHAPTER 1

INTRODUCTION AND BACKGROUND

In this chapter, background is given for the wind energy applications of flow-induced oscillations, and the mechanisms of vortex–induced vibrations are detailed.

1.1 Introduction

In 2015, 41% of all power capacity added to the United States was wind turbine based, bringing the national capacity to 74,000 MW or enough power for 20 million homes [12]. In particular, some models predict a 7% contribution by offshore wind power to the global energy supply by 2050 [38]. This figure is doubtlessly improved by several large-scale proposed projects, such as 816 MW of floating wind turbines (FOWTs) off the coast of Hawaii [95]. However current technology limits the market penetration of offshore wind energy due to innately higher Levelized Cost of Energy (LCOE) than both traditional onshore turbines and other energy sources [20].

If the turbine is permitted to float, a large percentage of global coastlines become more viable for offshore wind. Places such as the Western US seaboard, Northern Europe, Japan and China all quickly exceed 100 m of depth within kilometers of shore [95]. If the LCOE of FOWTs can be reduced to competitive ranges these high population density areas would considerably profit from the additional renewable energy influx. While very particular FOWT deployment scenarios already have an LCOE on par with a fixed-bottom offshore turbine [74], the costs can be brought down more readily by better designing the subsea mooring system [104]. The subsea mooring system consists of the mooring cables, anchors, and turbine platform (Figure

Figure 1.1. Various FOWT configurations compared to fixed-bottom structures. Josh Bauer, NREL.

1.1), and better knowing the hydrodynamic forces acting on these structures enables a more efficient, cheaper design.

The first operational FOWT array will be comprised of spar-type platforms [68]. A spar platform is essentially a high aspect-ratio cylinder partially filled with cement ballast and with a hollow upwards portion [61]. This offset center of mass keeps the cylinder upright and stable under various wind-wave loadings, and that stability is why the first FOWT array is comprised of spar platforms. At over 100 m long however there is the possibility for various flow-induced instabilities to occur on this uniform hull if the turbine is moored in any net current.

Vortex–Induced Vibration (VIV) is a well-studied form of flow-induced instability with implications for a broad range of design challenges ranging from cooling rods to smoke stacks to mooring cables. A bluff body in flow will have an unstable wake, which devolves into periodic shedding of large low pressure vortical structures, and

thus periodic loading on the structure. For a flexible structure, feedback between the oscillating structure and the periodic loading lock–in with each other, whereby amplitudes grow until a limit-cycle oscillation is stabilized. VIV is well studied for basic symmetric geometries, and even some more complex asymmetric bodies, but less so for the multi degree of freedom systems which permit three dimensional oscillation.

These complex oscillations are what is permitted by the subsea mooring system of FOWTs, and the main focus of the thesis. The uniform cylindrical hull of a spar platform is one such system. Traditional VIV study limits rigid-body motion to at most 2D crossflow-inline motion, while this structure can oscillate freely in three-dimensional space about its mooring point. Although the most massive structure of a FOWT assembly, the hull is only one aspect of how VIV interacts with the turbine. Indeed the moorings, whether catenary or taut, present kilometers of flexible cabling exposed to both uniform and shear flow. The most general study of these moorings can consider the effect of curvature on wake interference. By constraining the cylinder motion to crossflow and inline, established force reconstruction methods can be used to check how the concavity of the mooring damps higher harmonic fluid forcing, an important consideration for the fatigue life of the structure.

Thus far flow-induced oscillations have been cast as deleterious. It is possible though to use this mechanical phenomenon to the benefit of the operation of the turbine. By moving to the aeroelastic realm, flow-induced oscillations can be used to produce acoustic emissions of very high frequency, within the ultrasonic range above 20 kHz. An example of these flow-induced oscillations is the flexible larynx which bats control for their own ultrasonic phonation. In studying larynx mechanics, such emissions can be replicated and modified biomimetically as a deterrent for bats and birds near the spinning blade. In doing so, bat mortalities from the wind turbine can be minimized without curtailing the operational regime of the turbine.

This range of topics, from rigid-body motion of spar hulls and curved moorings to the frequency-jumping and hysteretic nature of replicating larynxes as tensioned films, comprise this thesis. Thus the thesis has the following structure, and goals of each study:

Chapter 2 studies the fundamental fluid-structure interactions of flexibly-mounted cylinders and prisms. Both cylindrical and square and triangular prisms are tested in flow given pure 2D inline-crossflow flexibility. Applications include floating turbine hulls in shallow water, where any movement would be almost purely 2D. Compared to spar hulls which are cylindrical, many semi-submersible hulls have prismatic sections exposed to flow. This chapter records the structural dynamics, wake interaction, and fluid forces acting on these structures, and examines how these aspects change as the angle of attack of the hull is changed. Notably for a square prism, when placed at an angle of attack of $\alpha = 0°$, odd-integer harmonics within the drag force acting on the structure cause abrupt jerks on the hull in the inline direction, in conjunction with strong side-to-side movement.

In chapter 3 the complete subsea system of a spar-type FOWT is considered. A scale model of a spar platform is moored in flow but otherwise freely floating, with all buoyancy and structural parameters matching those of full-sized spar prototypes. Free to oscillate fully three dimensionally, both the pitching movement and tip oscillations were recorded, permitting insight to the total response of the structure. Figure–eight trajectories surpassing one diameter in amplitude were observed for certain flow velocities. As current industrial design guidelines do not consider the influence of VIV, this lends credence to the idea that this additional loading phenomenon should be included in the structural design of these floating platforms. Furthermore, the region of the spar which energizes the system was isolated by incrementally placing VIV-suppressing strakes on the cylindrical hull, proving that certain inline-crossflow phase angles are indicative of flow excitation.

In chapter 4, the vortex–induced vibration (VIV) response of rigid curved cylinders flexibly mounted in crossflow and inline with varying concavity was examined. Such study is aimed at observing how flow interacts with mooring cables depending on whether their leading tip is upstream (concave) or downstream (convex) of the upwards portion of the cylinder which is perpendicular to flow. The role of concavity on the higher harmonic fluid forces is compared to the pure–crossflow case, and it is noted that the inclusion of an inline degree of freedom leads to substantially lower crossflow amplitudes when concave, compared to convex. Furthermore, the extended branch observed in the pure–crossflow concave case is mostly eliminated for the two-dimensional cylinder.

In chapter 5, aerodynamic flow-induced oscillations are considered in context of generating broad banded ultrasonic noise. While a different flow medium than the other chapters, the knowledge gained is important for the study of continuously flexible structures. This is an experimental, biomimetic approach whereby the mechanisms used within bat larynxes to generate ultrasound are reproduced and improved upon. A highly nonlinear response, the effects on acoustic emission of larynx geometry, tension and flow velocity are extensively investigated. The application this work is to deter migratory bats from the vicinity of the swept rotor area of spinning wind turbine blades.

Chapter 6 details the general conclusions and contributions of the present thesis. In addition, proposed future works are outlined which may continue the topics discussed in this project.

1.2 Bluff bodies in flow

One of the most fundamental bluff bodies to study in flow is that of a uniform cylinder. Here the bluff body is used to contrast the flow field of streamlined bodies, whereby their tapered points prevent flow separation. For this uniform cylinder, the

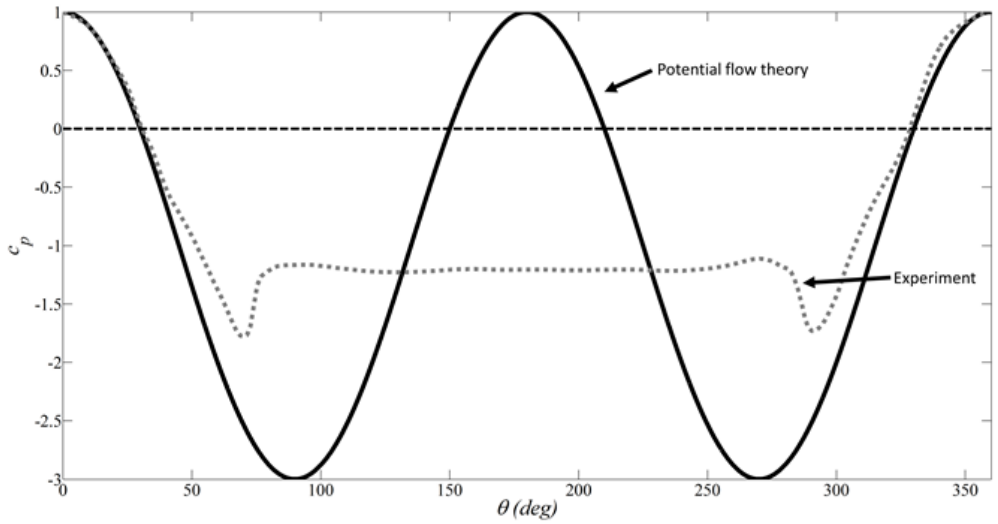

Figure 1.2. For $Re > 5$, the pressure distribution along the cylinder no longer follows potential flow theory due to flow separation.

classically defined Reynolds number [81] relates the inertial flow terms to the viscous flow terms, as

$$Re = \rho \frac{UD}{\mu} \tag{1.1}$$

where ρ is the fluid density, μ the dynamic viscosity, U the flow velocity and D a characteristic length (usually cylinder diameter in this thesis). To consider flow about a fixed cylinder for varying Reynolds numbers, for $Re < 5$ the flow remains attached to the cylinder, and $5 < Re < 40$ represents the first range for which vortices are formed. This flow detachment phenomenon is indicative of a break from the assumptions of potential flow theory, and the system can no longer be approximated as inviscid (Figure 1.2).

Of interest is that while the vortex pair forms in the wake, the flow is still too dominated by viscous forces to entrain the opposing shear layer. Without this shear layer mechanic the vortices are unable to shed, and instead continue to circulate attached to the cylinder [13]. This bound vortex pair is called Foppl vortices, and

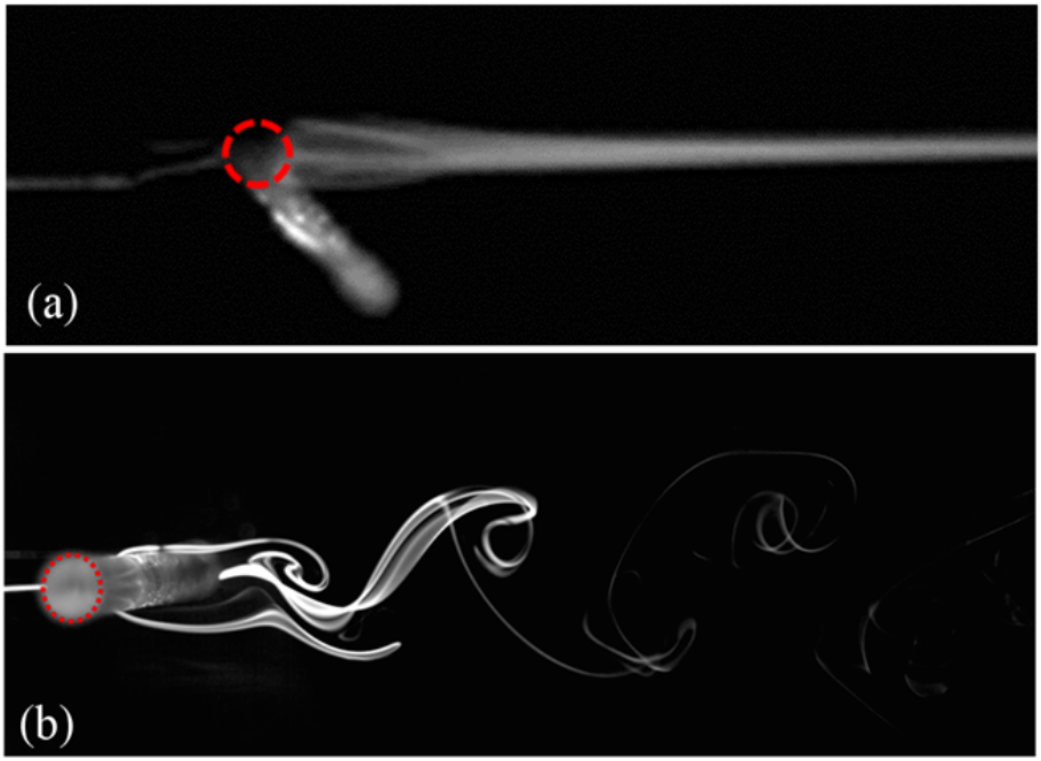

Figure 1.3. Flow visualization of vortex shedding regimes at (a) $Re = 36$, with attached Foppl vortices, and (b) $Re = 180$, with a stable von Karman vortex street. These were conducted using techniques detailed in chapter 3

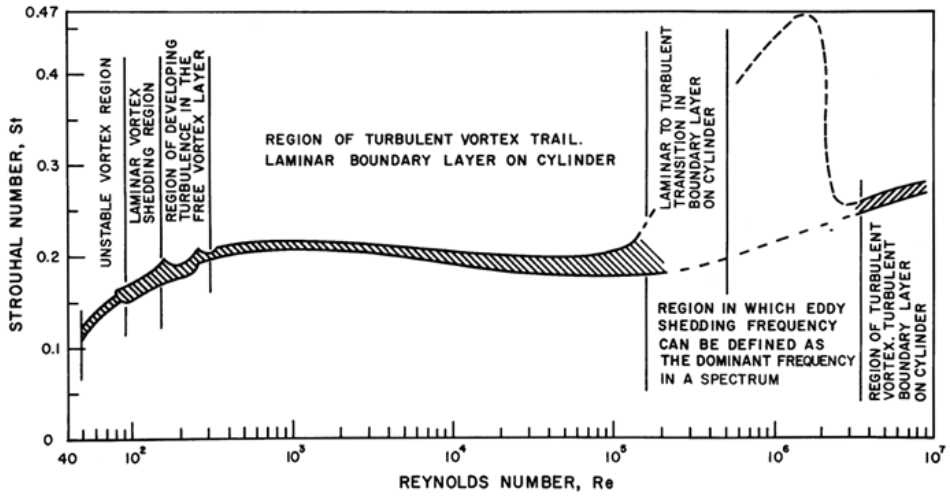

Figure 1.4. Strouhal number findings for $Re = 40\text{-}10^7$, from [67].

can be seen in 1.3(a). As the flow velocity increases, one of vortices will gain enough strength to entrain the opposing shear layer. In doing so, it severs the shear layer, from which it was being fed, and is shed downstream (Figure 1.3(b)). This phenomenon is one of the fundamental driving mechanisms of flow-induced oscillation. The rate of vortex shedding scales directly with flow velocity for fixed uniform cylinders in flow and, based on the original experiments by Vincenc Strouhal [98], collapses as the Strouhal number

$$St = \frac{f_{vs} D}{U} \tag{1.2}$$

where f_{vs} is the vortex shedding frequency. The Strouhal number can be approximated as a constant for subcritical Reynolds numbers ($Re < 10^5$). Although St depends on the geometry surface condition of the cylinder, $St = 0.2$ is a valid approximation for uniform cylinders of $10^3 < Re < 10^5$ (1.4) [67], while $St = 1 - 21/Re$ for $Re = 40$–200 [82]. For non-circular bodies, the Strouhal number must either be determined experimentally or approximated numerically.

As the vortices are shed, they are convected downstream by the flow while they gradually dissipate through viscous effects. For a symmetric cylinder, the vortices are uniformly staggered and this stable pattern is known as a von Karman vortex street ([17],[111]). The vortex street is stable for most orders of Re, except for during what is known as a drag crisis, a narrow Reynolds range where the wake is very disorganized as the boundary layer transitions to turbulence (1.5). As the boundary layer is neither fully laminar nor fully turbulent, pockets of the flow chaotically form what are known as separation bubbles as each locality transitions to turbulence [13]. During this transitory phase, the separation bubbles chaotically shift the circumferential shedding point of the vortices, preventing the periodicity which permits stable vortex shedding. Once fully turbulent, past $Re > 10^6$, the circumferential vortex separation points become more stable due to the boundary layer completely transitioning to turbulence and a fully turbulent vortex shedding pattern appears [13].

1.3 Vortex–Induced Vibrations

If the same bluff body previously mentioned is flexibly mounted, it will have natural frequencies dependent on the stiffness and degrees of freedom of the mounting, the mass of the body and the damping in the system. As a classical vibration example, a one-dimensional, mass-spring-damper system would reach resonance if a periodic forcing function acts upon it at the system's natural frequency. In the case of vortex–induced vibration (VIV), the vortex shedding is this periodic forcing function. To return to the pressure differential shown in figure 1.2, vortices are low pressure by nature of their circulation and these low-pressure regions manifest as lift and drag forces acting on the cylinder. Minor perturbations from the flow induce an initial displacement, and the displacement provides a synchronization mechanism between the structural oscillation and the vortex shedding: oscillation forces the vortex shedding to correlate along the length of the cylinder, bringing the lift forces into phase

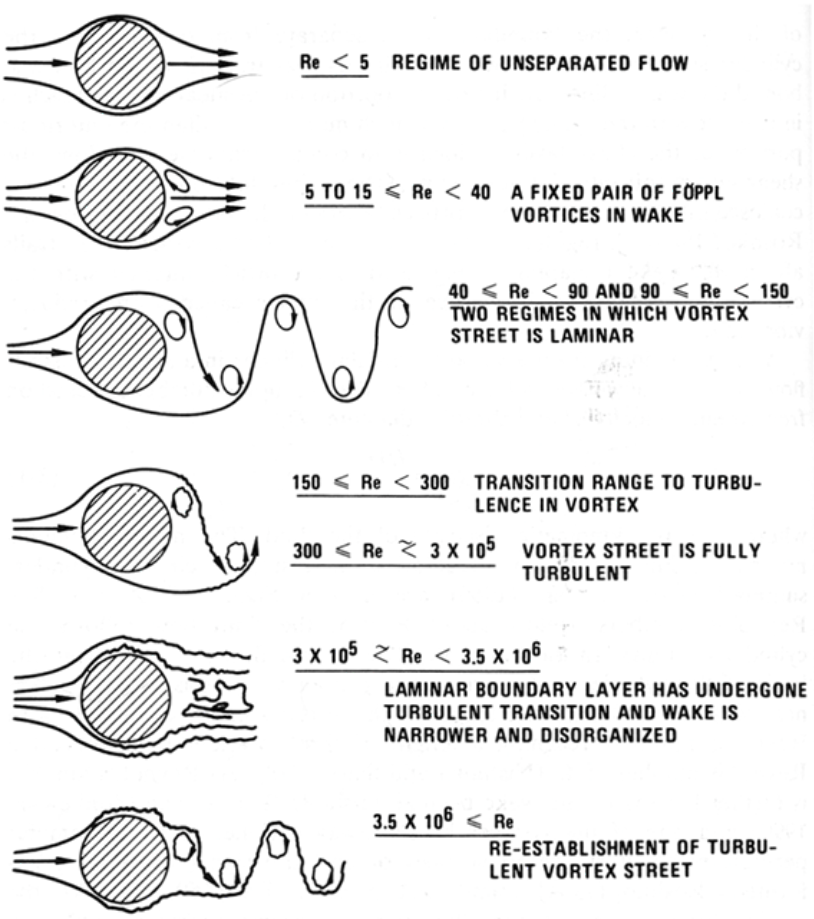

Figure 1.5. Progression of vortex regimes for higher Reynolds numbers, from [67].

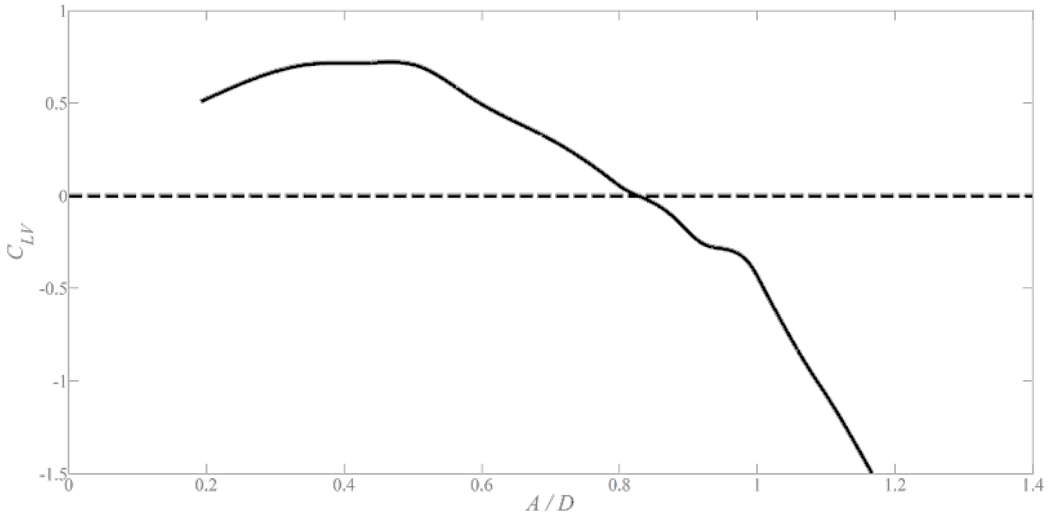

Figure 1.6. The relation between the velocity-synchronous lift coefficient and the oscillation amplitude. Positive values grow in amplitude, while negative values decay. Reproduced from Gopalkrishnan (1993)[46].

and resulting in increasing amplitude. The measure of how well synchronized vortex shedding is along the length of a cylinder is the "correlation length". If a vortex is shed along the entire length of the cylinder, the correlation length is 1 (normalized by the length of the cylinder). An increase in amplitude in turn feeds back into increasing the correlation length. The limit to this amplitude is based on the inertia of the system, which includes hydrodynamic added mass, and gives the limit cycle oscillation for each particular flow velocity. If the oscillation surpasses the velocity-dependent limit cycle amplitude, the lift-acceleration phase angle becomes negative and damps the amplitude until this dynamic stability condition is met (Figure 1.6).

For low velocities whereby the shedding frequency is far below the natural frequency of the cylinder, the system behaves as a traditional forced oscillator in that for increasing flow velocity, the oscillation amplitude increases due to the shedding frequency approaching the structure's natural frequency. However, to emphasize the effect of the shedding frequency f_{vs} approaching the natural frequency f_n, let us reorganize and substitute f_n in the Strouhal trend as per Blevins (1990)[18]:

$$0.2 = \frac{f_{vs}D}{U} = \frac{f_nD}{U}$$
$$\frac{U}{f_nD} = \frac{1}{0.2} = 5 \tag{1.3}$$

This inversion and substituted form of the Strouhal trend is what is known as the reduced velocity, U^*. Importantly, note the factor of 5 which relates the two. As U^* approaches 5, the shedding frequency equalizes with the natural frequency. For an ideal cylinder, this velocity marks the onset of lock–in between the oscillation frequency and vortex shedding frequency, about the natural frequency ([13],[18],[86],[113]). A 1:1 frequency is held over a range of different flow velocities, the lock–in range, as indicated by a break from the Strouhal trend, and this coupling between the oscillation and the flow forces is what differentiates VIV from classic resonance. There are many reviews on the fundamentals of this topic, in particular those of Bearman (1984)[13], Sarpkaya (2004)[86], and Williamson and Govardhan (2004)[113].

1.4 Nondimensionalizing VIV

For a classical one-dimensional forced oscillator, the equation of oscillation motion is well known to be

$$F = m\ddot{y} + c\dot{y} + ky \tag{1.4}$$

where F is the fluid force, m the moving mass, c the structural damping and k the spring stiffness constant. y will be referred to as the crossflow degree of freedom given by the spring. As discussed in [113] and [65], the F term in Equation 1.4 can be assumed to be sinusoidal during lock–in due to the periodic vortex shedding being correlated to the oscillation frequency, and simplified to

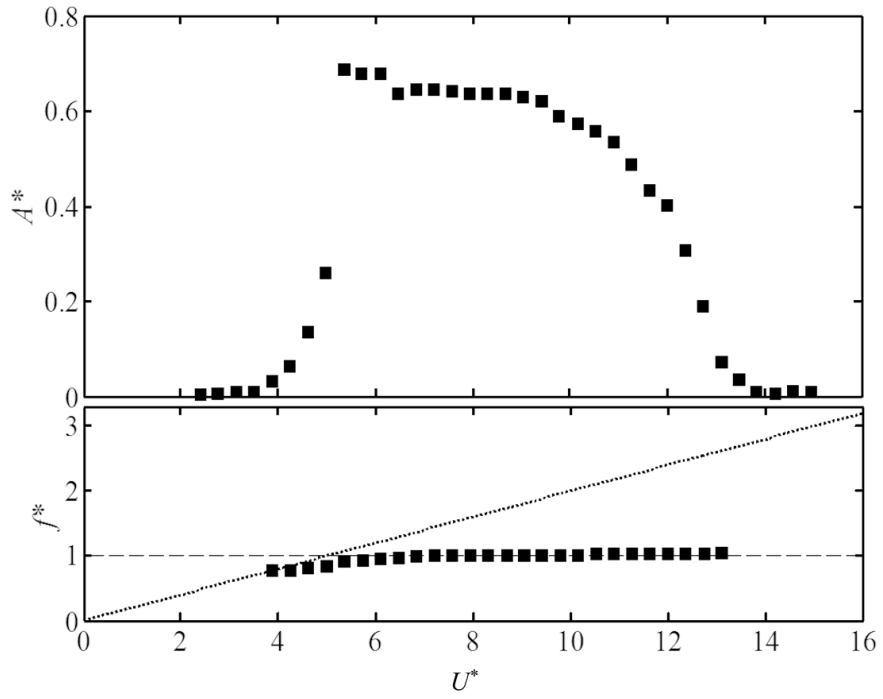

Figure 1.7. Vortex–induced vibration lock–in range for a uniform cylinder, with the Strouhal trend dotted.

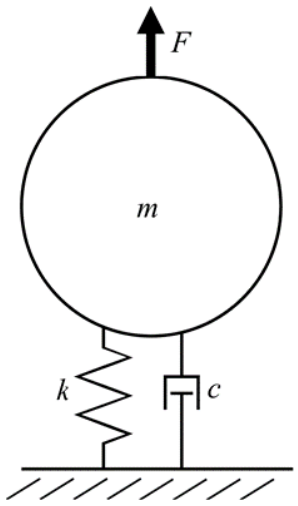

Figure 1.8. Classical one-dimensional forced mass-spring-damper system.

$$F(t) = F_0 sin(\omega t + \phi) \tag{1.5}$$

where ω is the oscillation angular frequency and ϕ the phase angle. The oscillatory response of the body will similarly be of the form

$$y(t) = y_0 sin(\omega t) \tag{1.6}$$

again with ω is the oscillation angular frequency. Khalak and Williamson [65] formulated a well-known set of dimensionless parameters which collapse the dimensionless amplitude response of a uniform cylinder to parameters of m^*, U^*, f^*, and C_{EA}. The common m^* mass-ratio is a relation between the mass of the moving body and the displaced fluid mass, thus

$$m^* = \frac{m}{\rho V} \tag{1.7}$$

where m is the moving mass, ρ the fluid density and V the displaced fluid volume. U^*, A^*, and f^*, the reduced velocity, amplitude ratio and frequency ratio respectively, are defined as

$$U^* = \frac{U}{f_n D} \tag{1.8}$$

$$A^* = \frac{A}{D} \tag{1.9}$$

$$f^* = \frac{f_{os}}{f_n} \tag{1.10}$$

where U is the dimensional flow velocity, f_n the natural frequency in still fluid, D the cylinder diameter and f_{os} the oscillation frequency. Khalak and Williamson [65] derived a relationship between these as

$$A^* = \frac{1}{4\pi^3} \frac{C_y sin\phi}{(m^* + C_A)\zeta} \left(\frac{U^*}{f^*}\right)^2 f^* \tag{1.11}$$

$$f^* = \sqrt{\frac{m^* + C_A}{m^* + C_{EA}}} \tag{1.12}$$

where the modified mass-damping parameter $\alpha = (m^* + C_A)\zeta$ first appears in the A^* term and uses the potential mass coefficient ($C_A = 1$, from potential flow theory), while the frequency response f^* makes use of the effective added mass coefficient as well:

$$C_{EA} = \frac{1}{2\pi^3} \frac{C_y cos\phi}{A^*} \left(\frac{U^*}{f^*}\right)^2 \tag{1.13}$$

The C_y term found throughout these parameters is the lift force coefficient :

$$C_y = \frac{F_y}{0.5\rho U^2 DL} \tag{1.14}$$

The present work considers only systems with light viscous damping, meaning the common simplification of the damping ratio ζ for underdamped systems may be applied:

$$\zeta = \frac{c}{2\sqrt{k(m + m_a)}} = \frac{1}{\sqrt{1 + \left(\frac{2\pi}{\delta}\right)^2}} \tag{1.15}$$

where the only new terms are δ, the logarithmic decrement, and m_a is the added mass

$$m_a = C_a \rho V \tag{1.16}$$

such that the added mass coefficient is multiplied by the displaced fluid mass to find the total added mass. These parameters are compatible with the form of a forced underdamped oscillator equation of motion, and plugging them back in gives

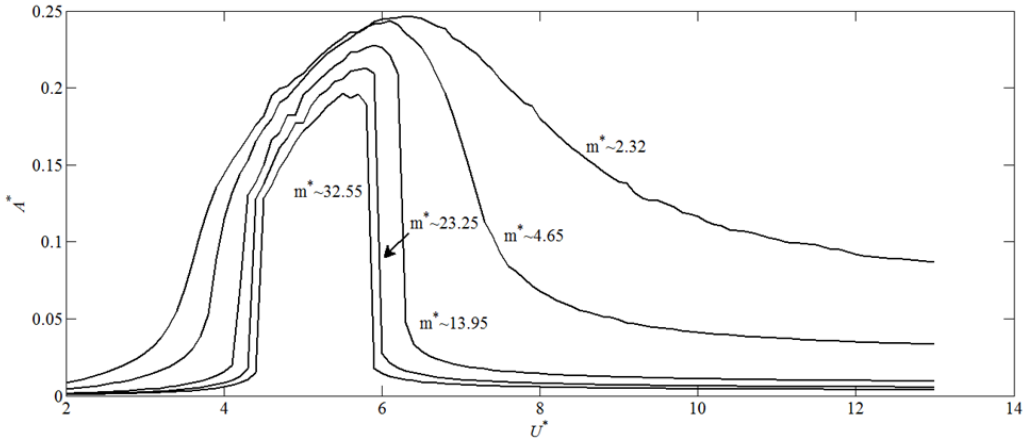

Figure 1.9. Solutions of the wake oscillator model.

$$(m + m_a)\ddot{y} + (c - 0.5\rho U^2 D C_{LV})\dot{y} + ky = 0 \tag{1.17}$$

where the fluid forces have been wrapped into the damping term.

1.5 The wake oscillator model

The similarities between the basic equations of motion reported in Chapter 1.4 and a self-excited oscillator have inspired efforts in the past to attempt to model VIV as a simple nonlinear oscillator based off the van der Pol equation ([18], [50], [94]). The model is devised around the underdamped forced oscillator equation of motion, plugging in the equivalent dimensionless parameters and coupling the resultant to the van der Pol equation. The reader is referred to the literature for the full derivation ([18], [40], [50], [94]). The amplitude and frequency response can then be found by solving the coupled differential equations of

$$\begin{aligned} Y'' + (2\zeta\Delta + \frac{\gamma}{m_1^*})Y' + \Delta^2 Y &= \frac{M}{m_1^*} q \\ q'' + \epsilon(q^2 - 1)q' + q &= AY'' \end{aligned} \tag{1.18}$$

and

$$\Delta = 2\pi \frac{1}{St} \frac{1}{U^*} \tag{1.19}$$

Here γ, M, A and ϵ are empirically derived constants [40], with the other variables defined in the previous section. The solution to the above equations can be seen in Figure 1.9 for varying $m^*\zeta$ values. Compared to experimental results (Figure 1.7), one can observe that the wake oscillator model matches neither the width nor the peak amplitude of actual results. This is from several innate assumptions for the derivations of the terms: inviscid, two-dimensional flow with the forcing terms only dependent on fluid velocity and acceleration. These, amongst other weaknesses [84], prevent accurate results when compared to experimental data or, more recently, strongly-coupled computational fluid dynamic (CFD) simulations of flexibly mounted uniform cylinders.

However, the wake oscillator model reasonably predicts the oscillation frequency. To refer back to offshore engineering applications, the peak amplitude for a moderate m^* cylinder undergoing VIV is $A^* \approx 1$, meaning for flexible structures the chief failure mode is not ultimate failure but rather fatigue damage resulting from the continuous oscillation of the structure. As the wake oscillator model can model the oscillation frequency, it can be used for designing against fatigue [72]. Thus, the wake oscillator model does have some utility in this regard, particularly when tuned with empirical constants similar to the desired environment.

1.6 Response of a cylinder with crossflow flexibility

The canonical uniform cylinder flexibly mounted in crossflow has widely been used to study the influence of various structural parameters. For this fundamental case, a topic of thorough research has been the effects of oscillatory mass and structural damping, which as seen in equation 1.11 point to an inverse relation with the maxi-

Table 1.1. Important dimensionless parameters

Reynolds Number	$Re = \rho \frac{UD}{\mu}$
Strouhal Number	$St = \frac{f_{vs} D}{U}$
Reduced Velocity	$U^* = \frac{U}{f_n D}$
Amplitude Ratio	$A^* = \frac{A}{D}$
Frequency Ratio	$f^* = \frac{f_{os}}{f_n}$
Mass Ratio	$m^* = \frac{m}{\rho V}$
Lift Coefficient	$C_L = \frac{F_y}{0.5 \rho U^2 D L}$
Drag Coefficient	$C_D = \frac{F_y}{0.5 \rho U^2 D L}$
Damping Ratio	$\zeta = \frac{c}{2\sqrt{k(m+m_a)}} = \frac{1}{\sqrt{1+\left(\frac{2\pi}{\delta}\right)^2}}$
Mass-damping parameter	$m^* \zeta$
Modified mass-damping parameter	$\alpha = (m^* + C_A)\zeta$
Skop-Griffin Parameter	$S_G = 2\pi^3 St^2 m^* \zeta$
Structural Stiffness Ratio	$SR = \frac{f_{nIL}}{f_{nCF}}$

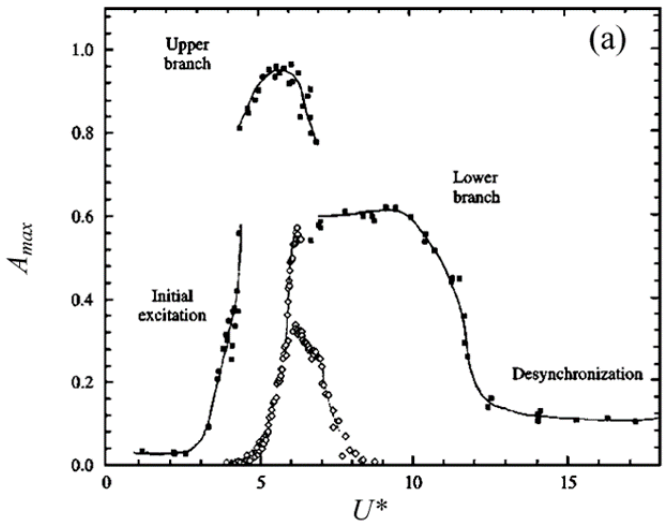

Figure 1.10. Comparison between high mass-damping (Khalak and Williamson [64], $m^*\zeta \approx 0.013$) and low mass-damping (Feng [41], $m^*\zeta \approx 0.34$) systems, from Khalak and Williamson [65].

mum amplitude. In Figure 1.10 high mass-damping results of Feng [41] are reported with $m^*\zeta \approx 0.34$ for comparison with Khalak and Williamson 1997 [64], with low mass-damping $m^*\zeta \approx 0.013$. Evident at low mass-damping is the appearance of three distinct branches: the initial, upper and lower branches. Govardhan and Williamson [47] experimentally found a relation for very low values of $m^*\zeta$ whereby the upper branch actually sees divergent amplitudes as m^* trends towards zero. Importantly, they also deduced that this was a result of the lock–in region becoming infinitely wide. Extrapolating their data, they found a critical mass ratio of $m^* \approx 0.54$ for this to occur. This has significance for tension–leg wind turbine platforms, which due to the tension in the anchors have an overall mass ratio below 1, and may approach this region.

The trend of how the initial, upper and lower branches reduce in amplitude depending on m^* and ζ has long been a topic of research in VIV. One early method at doing so is the Skop-Griffin parameter

$$S_G = 2\pi^3 St^2 m^* \zeta \tag{1.20}$$

where St is previously discussed Strouhal number and all other parameters previously defined. The Skop-Griffin number has proven robust at collapsing the maximum oscillation amplitude for cylinders with crossflow flexibility against this combined mass and damping parameter ([49], [93]), but has also received criticism ([85], [84],[83]). Criticism posited that for small values of S_G, m^* and ζ cannot be linearly coupled as they both influence the amplitude response separately. This skepticism was supported largely by the scatter within the data used to generate the Griffin plot, observable when plotted in log-linear space. However S_G shows agreement for more general trends. An alternate approach avoids coupling the mass and damping ratios [86] by deriving the maximum oscillation amplitude as

$$A^* = 0.5 C_L sin\phi \frac{1}{2\pi^3 \zeta} \frac{\rho_f}{\rho_m} \left(1 + C_a \frac{\rho_f}{\rho_m}\right)^2 \left(\frac{U}{f_n D}\right)^2 \tag{1.21}$$

In this form, m^* is replaced by ρ_f/ρ_m, a ratio of the equivalent densities of the structure and the fluid. Despite avoiding the ambiguity concerning the mass-damping parameter, this form is less common. The usefulness of the mass-damping parameter was improved by applying a correction factor to account for the hydrodynamic mass: as derived previously [65] the mass-damping parameter $(m^* + C_a)\zeta$ provides a better trend relating amplitudes to oscillatory mass ([48],[65]), seen in Figure 1.11, and it was found to collapse the results of 2D oscillations equally as well.

1.7 Flow forces

Taking force measurements allows insight as to why the amplitude decreases after the upper branch, despite the oscillation frequency still being locked-in with the vortex shedding frequency. Figure 1.12 shows experimental data for the in-phase coefficient of lift at different reduced velocities. This can be found via forcing the cylinder

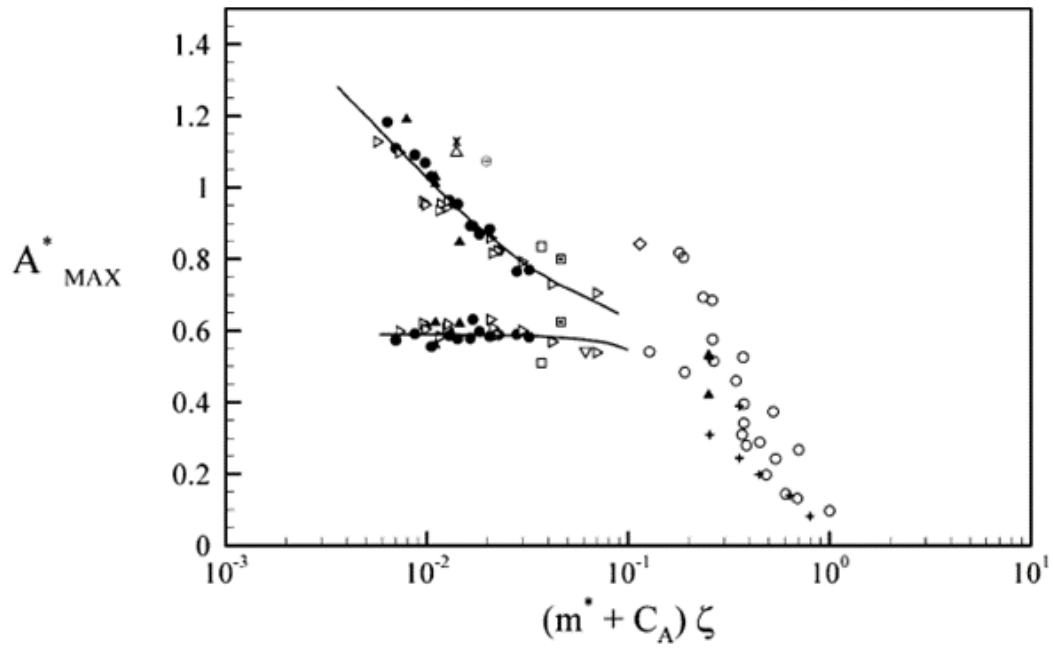

Figure 1.11. Increasing mass and damping logarithmically decreases the maximum amplitude, from [114]. The two trend lines report the amplitude of the upper and lower branches.

to oscillate in the flow rather than allowing natural free vibrations, and measuring the lift forces simultaneously with the oscillation profile. Sarpkaya [83] conducted an extensive campaign of such tests, providing a wide range of lift coefficients for different conditions. The significance of a positive $C_Y cos\phi$ (also known as C_{LV}) value is that it effectively indicates negative damping, remembering the equation of motion of form Eq. 1.17. During lock–in the oscillation amplitude increases until C_{LV} reaches equilibrium

Figure 1.13 reports phase angle measurements for forced (Bearman and Curie [14]) and free (Feng [41]) oscillations of a rigid cylinder. Of note is that the discontinuous phase jump recorded by Feng is actually a continuous change for physical systems. The phase jump indicates the significance of the exact timing in the oscillation of the cylinder when the vortex sheds, and correspondingly when the lift is at maximum. Vortices being shed out of phase with the oscillation coincide with a

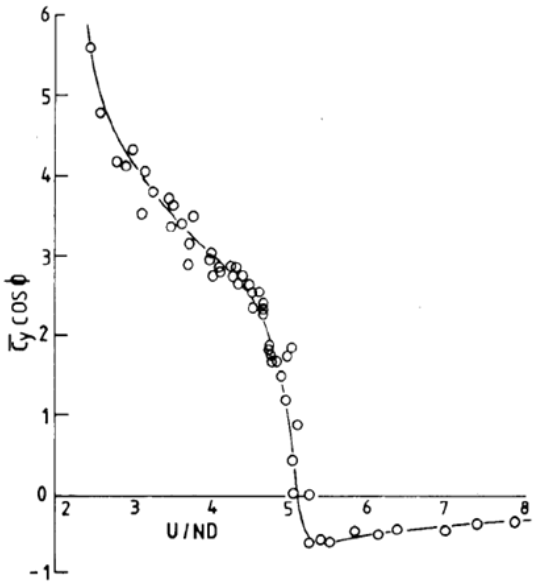

Figure 1.12. In-phase lift coefficient for different reduced velocities using a forced–oscillation experiment, from [83].

decreased amplitude due to $C_y cos\phi$ now being much reduced. What this looks like in the physical sense is a sudden change between vortex shedding modes. Rather than shedding one vortex per side, the phase jump means now two are shed per side (Figure 1.14(a)). These two modes are known as 2S and 2P respectively (Williamson and Jauvtis [114]). Mapping out the vortex modes of the initial, upper and lower branches shows the relation between the phase jump, $C_y cos\phi$, and the change to 2P shedding (Figure 1.14(b)).

1.8 Systems with multiple degrees of freedom

The discussion thus far has only concerned rigid cylinders with crossflow freedom. However, the loading imparted on even a simplified 2D cylinder via vortex shedding clearly exists in more than purely the crossflow direction, with a periodic inline force also present. For a circular cylinder, the lift force in crossflow is resultant from vortices shed from each side of the cylinder, which counteract eachother. In the inline direction

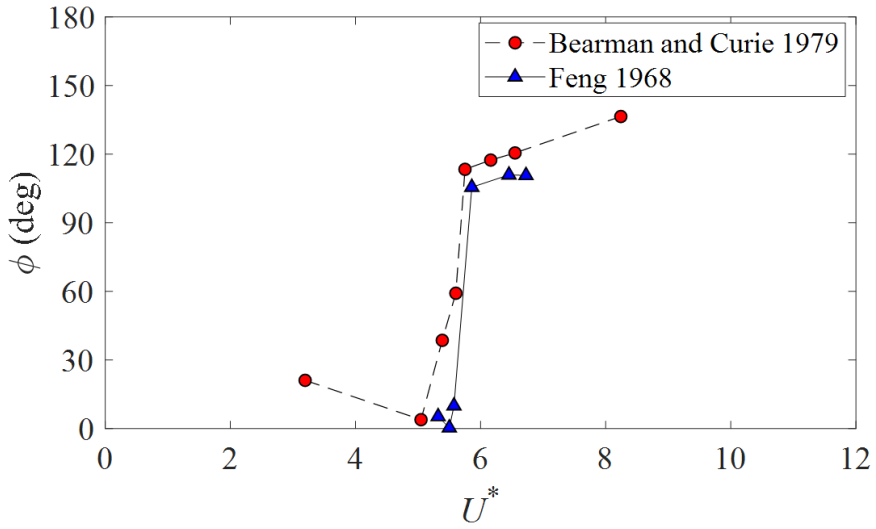

Figure 1.13. Phase angle measurements for forced (Bearman and Curie [14]) and free (Feng [41]) oscillations of a rigid cylinder.

however, each vortex shed imparts a drag force on the cylinder without counteraction. Therefore for a symmetric cylinder there is a 2:1 ratio between the frequency of the lift force and the frequency of the drag force. If given additional flexibility in the inline direction, the cylinder can resonate due to both lift and drag at this 2:1 ratio. While for high mass systems ($m^* > 6$) the inline contribution is negligible ([59], [85]), significant changes in the peak amplitude occur as the mass ratio is reduced ([32],[31],[30]). While the inline oscillation is small in amplitude compared to that of crossflow, the interaction between the two degrees of freedom can permit a greater transference of energy from the fluid to the cylinder and higher crossflow amplitudes than comparable cylinders with pure crossflow freedom. For example, if the structural crossflow-inline stiffness ratio is tuned to the same 2:1 fluid excitation frequency, the amplitude in crossflow surpasses that of purely transverse motion (Figure 1.15). This biharmonic oscillation [85]) mapped as a two-dimensional orbit appears as a figure–eight trajectory, with a directionality defined by the inline-crossflow phase angle. Nomenclature coined by Dahl et al. (Dahl [31],[30]) here defines the directionality

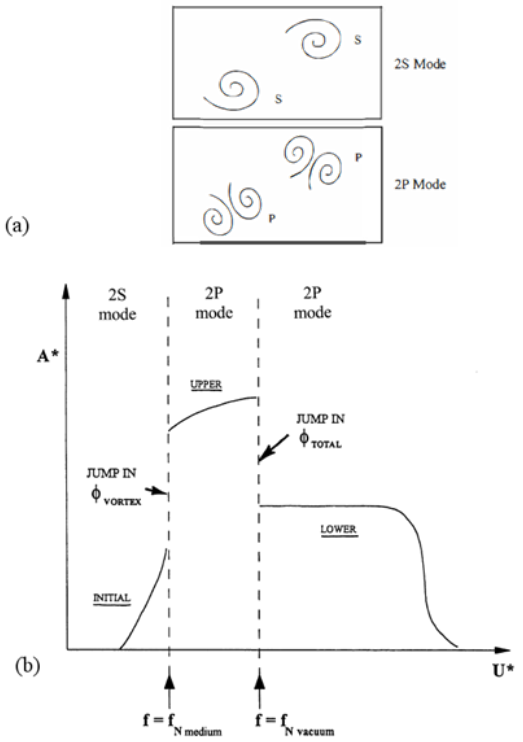

Figure 1.14. Definitions of (a) first two primary shedding modes (from [114]), and (b) how the change in shedding modes corresponds to transitions between branches (from [47]).

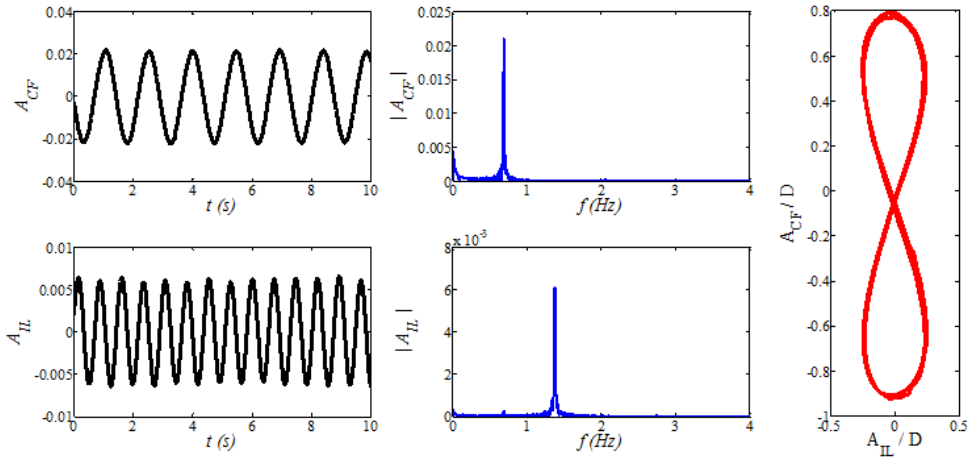

Figure 1.15. Sample data of a uniform cylinder with 2:1 natural frequency ratio and $m^* = 4.65$. See Chapter 4 for methodology.

to be counter-clockwise if the cylinder oscillates into the flow at the extrema of the crossflow oscillation. Conversely, it is called clockwise if it rotates with the flow at that point [30]. Seen from above with left–right flow, the upper orbit of a figure–right would be correspondingly CCW or CW. Direct Numerical Simulation (DNS) studies have shown that for a flexible cylinder in cross-flow, CCW regions indicate structural excitation by the flow [22].

Just as high mass systems damp this dual resonance condition, so too does structural stiffness ratios removed from the 2:1 excitation ratio (Dahl [31],[30]). From an incremental series of stiffness ratios ranging from 1 to 2, Dahl et al. observed the figure–eight orbit to decrease in transverse amplitude, and a much greater decrease in inline amplitude. This collapses the response back to approximately that of a one-dimensional motion. Their findings at a 2:1 stiffness ratio though support tests by Williamson and Jauvtis [114]. With extensive flow mapping, they observed a "super-upper" branch at $A^* \approx 1.5$ for a low mass cylinder ($m^* \approx 2.6$) whereby a new "2T" shedding mode was driving this large-amplitude motion Figure 1.16. 2T means two vortex triplets shed per oscillation, following common vortex shedding nomenclature

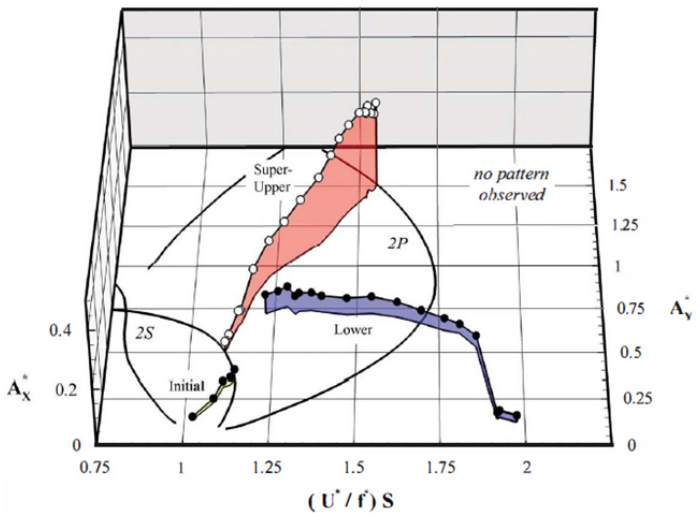

Figure 1.16. The appearance of a "super-upper" branch for low m* cylinders mounted in 2D , from [114].

(Williamson and Roshko [115]). Higher harmonic force components were recorded both for the super-upper branch (Jauvtis and Williamson [59]) and, more generally, for most biharmonic oscillations near peak amplitude (Dahl et al. [31]).

1.9 Continuously flexible structures

The study of rigid cylinders takes advantage of the fact that, despite being flexibly mounted, the portion of the structure in contact with flow never changes geometry. This is a simplification which forces the fluid forces to respond only to the excitation modes of the structure's fixture. To move beyond this limitation, a continuously flexible structure would have infinitely many modes which could be excited by the flow ([22], [54], [71], [77],[77], [109]). In uniform flow, very complex interactions occur as the shedding frequency intermittently locks-on with different portions of the cylinder, causing the cylinder to jump between modes (Figure 1.17). Traveling waves form as competing instabilities prevent the formation of stable correlated regions [108]. This results in numerous changes for VIV of a flexible cylinder compared to

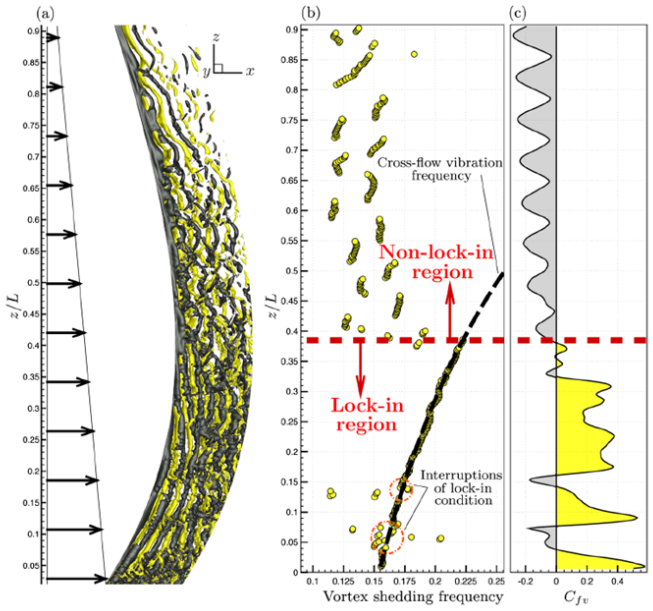

Figure 1.17. A flexible cylinder simulated via DNS for sheared cross-flow, from [22].

that of a rigid cylinder. For instance, the Independence Principle states that for inclined rigid cylinders, axial flow along the cylinder is unimportant and the response is governed only by the component of flow normal to the cylinder. This holds true for a wide range of inclinations ([55], [99]), and in the past was assumed to hold true for the same range for flexible cylinders [60]. For continuously flexible cylinders the Indepence Principle has been proven to be inaccurate for certain inclintations. ([21], [92]).

The current state of research for flexible cylinders is moving towards multi-body interaction. Little is known about the interactions between clustered or even tandem cylinders, despite being recognized as having great significance from an engineering design perspective for offshore risers or cooling rods ([18], [117]). There have been studies on clustered cylinders in axial flow [43], where the flow is simpler due to the lack of wake interaction, but for cross-flow only simplified structures have been considered, i.e. rigid cylinders with flexible mountings [78]. More recently, it has been

observed that wake-induced oscillation is the dominant mode for a flexible cylinder in tandem, though VIV is also present ([52], [54], [53]). This shows similarity to rigid tandem cylinders, where the downstream cylinder actually encounters the greater loading of the two [6], but with the key distinction that the spacing between the cylinders has little effect on the wake-induced oscillations for a flexible cylinder. This eliminates another assumption inherited from the study of rigid cylinders, as there the spacing greatly changes the fluid forces recorded on the downstream cylinder ([9], [10]).

CHAPTER 2

VORTEX-SURFACE ALIGNMENT FOR PRISMS WITH CROSSFLOW-INLINE FREEDOM

In this chapter, vortex alignment with the afterbody of asymmetric flexibly-mounted prisms and the resulting flow-induced vibrations are studied. Square and triangular prisms were studied experimentally for all angles of attack, and it was observed that the lift and drag coefficients approach their maximum values for cases when the surface normal angle of the afterbody aligns with the vortex shedding angle. New results pertaining to a kink in a galloping-type response are presented, and we discovered it manifests with an even greater influence for a system with 2D dual-resonance permitted.

2.1 Introduction

A cylinder free to oscillate in the crossflow direction has been extensively studied as a canonical example of vortex-induced vibration: a phenomenon whereby for a structure in fluid flow the frequency of vortex shedding can lock-in with the structure's oscillation frequency and remain locked-in for a range of flow velocities, creating the lock-in region. Across this region, large-amplitude oscillations occur. There are numerous review papers on this topic (e.g. [13], [113], [84]). There are also some studies for a cylinder with two degrees of freedom. Jauvtis and Williamson [59] provide a thorough summary of VIV of a cylinder with two degrees of freedom, followed by studies by Dahl et al. on the topic ([30], [31], [32]). Notably, when permitted to resonate in both the inline and crossflow directions, significantly higher

oscillation amplitudes can be observed in the crossflow direction, resulting in a super-upper branch, which is accompanied by 2T vortex shedding for structures with low m^* (m^* <6) [59]. This results in a figure-eight amplitude profile, where the inline component oscillates at twice the frequency of the crossflow oscillation.

Since vortices are shed per cycle from both sides of the cylinder, the apparent force on the structure in the inline direction is acting twice per cycle (2f) while the force in the crossflow direction is only at 1f. Dahl et al. ([30], [31], [32]) coined the terminology of clockwise (CW) and counterclockwise (CCW) directionality to the figure-eight orbits based on the crossflow-inline phase angle. If the cylinder oscillates *into* the flow at the extremes of the crossflow movement, the response is said to be counterclockwise. If flow is left-right when looking at the orbit, the upper lobe of the orbit has counterclockwise directionality for these cases. Importantly, studies investigating the flow-induced vibrations of continuously flexible cylinders see that portions of the cylinder which correspond to structural excitation undergo CCW orbits, while those portions that are actually damping the response could undergo either CW or CCW orbits [73][22]. This has also been confirmed for rigid cylinders free to oscillate in crossflow and inline, and also rotate about a central mooring point. By showing that if VIV is suppressed only in the portion of the cylinder otherwise undergoing CCW motion during resonance, VIV is suppressed for the structure as a whole [27].

In giving background to the effect of multiple degrees of freedom, it should be noted that the studies discussed prior have exclusively considered cylinders with a uniform circular section. When this symmetry is broken, other forms of flow-induced oscillations can occur, such as galloping. A galloping–type response occurs when an angle of relative flow brings fluid forces into phase with the velocity of oscillation, resulting in high amplitude oscillations which continue to grow in magnitude for higher velocities: whereas vortex-induced vibrations only have a limited velocity range where

a stable equilibrium is reached, and decay to zero outside this region. In the past it has been observed that a square prism with one side close to perpendicular to flow and with a crossflow degree of freedom experiences galloping for angles of attack up to 7.5° ([120], [75]) (where the angle of attack is defined as the angle between the surface normal of the trailing face and the inline direction, but has a narrow region between $\alpha = 7.5° - 10°$ where both VIV and galloping are exhibited as the response transitions to mainly VIV [75]. For higher angles of attack, the response is predominantly VIV. It has been shown that the galloping response at $\alpha = 0°$ experiences kinks ([16], [75]), and it has recently been explained by Zhao et al. [119] that these kinks are from odd-integer synchronization between the shedding frequency and the oscillation frequency. In other words, while the prism gallops throughout the U^* range, certain velocities allow synchronization and VIV. Uniquely, all these cases have been for pure crossflow degree of freedom, but Zhao et al. [123] [122] performed numerical analysis for a square prism with 1:1 crossflow–inline stiffness. They imposed a mass ratio of $m^* \approx 3$ and performed simulations at $\alpha = 0°, 22°$ and 45°. In a break from previous findings, Zhao, M. et al. [123] reported a limited lock–in region at $\alpha = 0°$, before transitioning to a galloping response with an amplitude much smaller than the 1D experimental findings of Zhao, J. et al. [119]. Despite the 1:1 stiffness ratio, the mass ratio was sufficiently small for the cylinder to undergo "soft lock–in", whereby the inline oscillation frequency detunes from the natural frequency and matches the shedding frequency at twice the natural frequency [70]. This ratio is due to symmetry in the inline direction.

Compared to the square case, a triangular prism with a crossflow degree of freedom is notable in that the triangular case is completely asymmetric about fore-aft, while the square has mirrored asymmetry. Several recent studies have considered the equilateral triangle case ([3], [2], [4], [1], [91]). The experimental works by Alonso et al. ([3], [2]) considered a pendulum-mounted prism (crossflow freedom with a slight

inline contribution) and recorded the oscillation response and instability regions for varying angles of attack and varying leading vertex angles. They showed that both α (the angle of attack) and β (the lead vertex angle), influence the onset of galloping. Alonso et al. 2012 [4] continued to expand the instability map for a triangular by also considering hysteresis. They showed the instability regions agreed with the findings of Parkinson and Smith [80], in that the the galloping instability can is related to the slope of lift versus α and furthermore that hysteresis occurs at inflection points of C_L vs α. Seyed-Aghazadeh et al. 2017 [91] considered a prism mounted with a pure crossflow degree of freedom and investigated the wake modes, oscillation response and fluid forces for $\alpha = 0° - 60°$ and $U^* = 3$–23. They showed a limited range between $\alpha = 30° - 35°$ where both VIV and galloping occur at different U^* ranges. Between $U^* = 7$–14.5, the response resembles VIV in that lock–in has a minimum and maximum velocity. No response was observed for $U^* = 14.5$–19.5, and galloping begins past $U^* = 19.5$ for these angles. A pure galloping response was recorded for all cases above 35° whereby the amplitude grows proportionally with velocity. This was confirmed as high frequency vortex shedding, while the cylinder's oscillation frequency was below the natural frequency.

The present study considers the flow-induced vibration of a square prism with crossflow–inline freedom, tuned such that $f_{nIL} = 2 \times f_{nCF}$. Of interest is whether the synchronization kinks reported for crossflow galloping also occur in 2D, and any corresponding change to the odd-integer lift and drag harmonics.

2.2 Experimental Method

Experiments were run in a recirculating water tunnel with a $1.27 \times 0.5 \times 0.38$ m test section which has a turbulence intensity below 1% for flow velocities up to 1 m/s. Using bubble-image velocity, the uniformity of flow was measured to be within 2-8% of the nominal flow velocity for the free–stream (i.e. excluding the

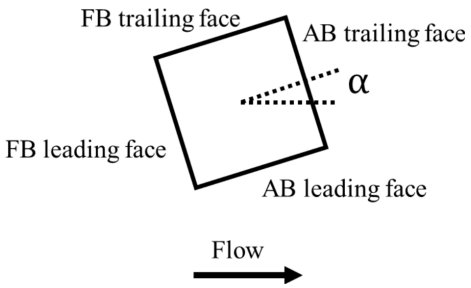

Figure 2.1. Angle of attack orientation for the square and triangular prisms, where α is given by the trailing face of the afterbody.

wall effects). For additional discussion on the bubble-image velocimetry technique, see Seyed-Aghazadeh et al. [91]. A mounting apparatus was constructed which used two planar air bearings to support a lightweight aluminum truss, permitting it to move freely in a plane. Relatively long springs (254 mm) connect the truss to a rigidly-fixed frame attached to the test section, with the length of the springs chosen to minimize the structural coupling in the crossflow and inline directions. Non-contacting displacement sensors fixed to the frame measured the movement of the truss in the crossflow and inline directions. As peak displacements approach 25 mm, the maximum angular deflection of the springs is thus below 6°. FFT of arbitrary displacements showed crossflow–inline coupling to be on the order of 1%, i.e. the frequency contribution of the perpendicular component was approximately 1% that of the orientation of the displacement sensor. Between the truss and the surface-piercing cylinder, a six-axis ATI Nano-17 force sensor directly measured any forces acting on the cylinder. All results in the present work had the inertia of the combined cylinder and attachment load subtracted from the forces recorded by the sensor.

The bluff bodies considered included a circular cylinder, a triangular cross-section, and a square cross-section. For the square and triangular prisms, the angle of attack is defined by the angle that the trailing face makes with respect to the incoming

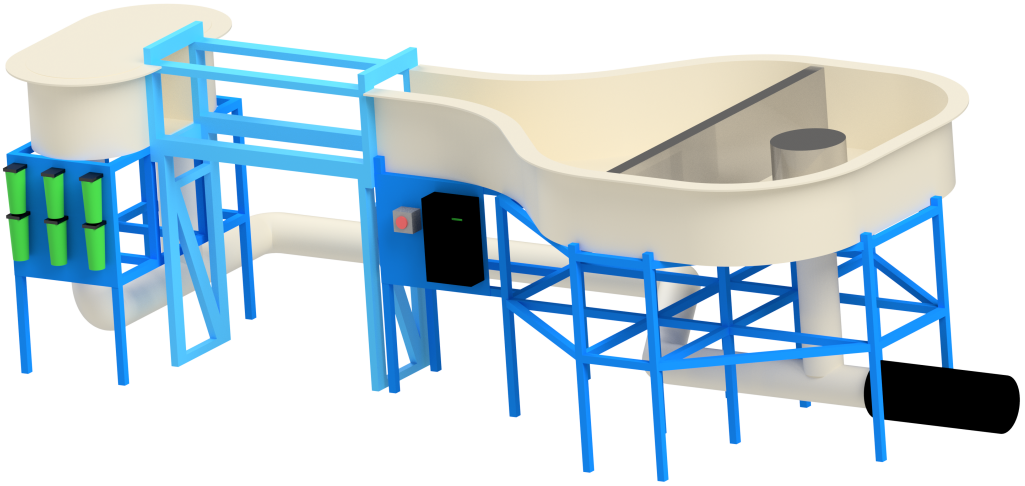

Figure 2.2. Drawing of the recirculating water tunnel used in the present thesis.

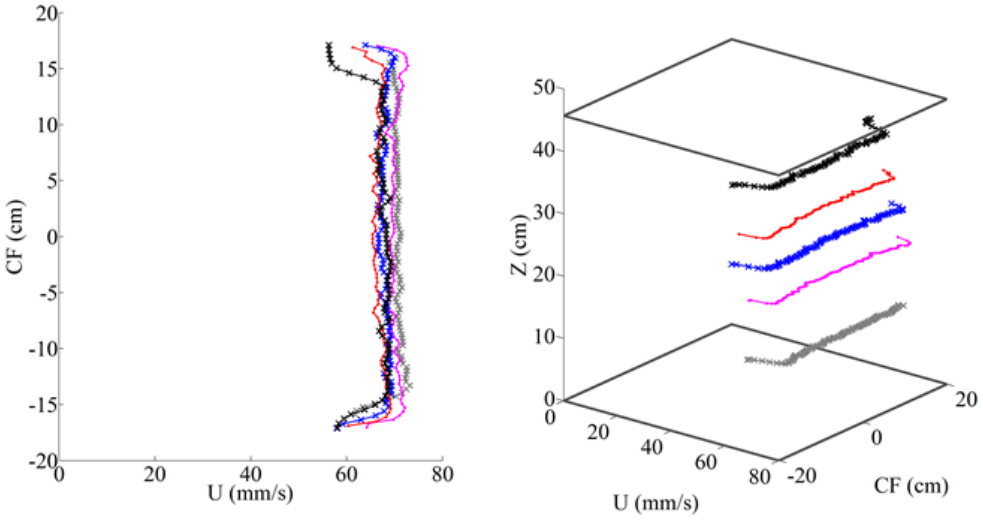

Figure 2.3. Sample flow profile of the test section seen in Figure 2.2 taken at 76 mm/s. Flow uniformity of the free–stream within 2-8% of nominal velocity. Reproduced from Seyed-Aghazadeh et al. [91].

flow. (Figure 2.1). The cylinder and the square prism were manufactured from a lightweight ABS plastic using 3D printing to give them a hollow interior, and a maximum diameter of 2.54 cm for the circular cylinder and 1.9 cm for the square prism. The mass ratio (defined as $m^* = \frac{m}{\rho V}$ where m is the moving mass, ρ the fluid density, and V the displaced fluid volume) was $m^* \approx 2.54$ for the circular cylinder and $m^* \approx 4.52$ for the square cylinder. The triangular prism was previously used in a study for 1D VIV and galloping, has a higher mass ratio at $m^* \approx 27.9$. The aspect ratio, L/D, was 8.5 for the circular cylinder, 11.4 for the triangular prism, and 17.8 for the square prism.

For flow visualization, a 50 μm platinum wire was mounted at the midplane of the test section, 3 cm upstream from the cylinder. A 100 volt, 2 amp power supply connected the platinum wire to two carbon plates below the wire, and the voltage potential between the platinum and carbon created a stream of hydrogen gas from the platinum wire via hydrolysis. The bubble field thickness was of the order of the wire diameter (50 μm), and was illuminated by two light-emitting diode (LED) lighting banks such that a high-speed camera could capture vortices shed from the cylinder within the plane of the bubble field.

2.3 Response of the circular cylinder

The apparatus was first validated for the VIV response of a uniform cylinder with $f_{nIL} = 2 \times f_{nCF}$, where f_{nIL} and f_{nCF} are the natural frequencies in otherwise still fluid, in the inline and crossflow directions, respectively. The results of these tests will be compared against existing experimental data ([31], [114], [86]).

In Figure 2.4, the oscillation orbits, crossflow-inline phase angle, and lift-acceleration phase angle are shown for all U^*. Below $U^* = 3.96$ the wake is symmetric and vortices are shed into the far wake, thereby no imposing periodic forces on the cylinder (Figure 2.5(a)). The reduced velocity of $U^* = 3.96$ marks the onset of synchronization

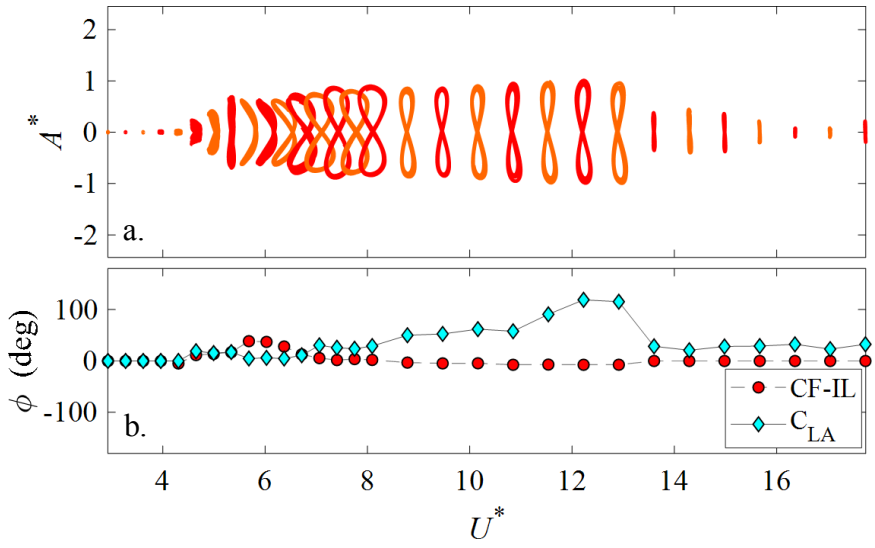

Figure 2.4. Amplitude and phase plots for a circular cylinder undergoing dual-resonance across the lock-in U^* range.

between vortex shedding and the cylinder's oscillation in the inline direction (Figure 2.5(b)). Minute disturbances within the flow provide some initial movement, and the shedding of vortex pairs becomes synchronized with the oscillation frequency. This shedding regime is known to occur for cylinders with one degree of freedom in the inline direction [25][26], but the addition of a crossflow degree of freedom results in a narrowing in the width of the U^* range for which symmetric shedding is observed. Purely symmetric shedding was only observed at $U^* = 3.96$, but the courseness of the velocity increments limits commenting on the width of this range. At $U^* = 4.3$ the crossflow component also synchronizes, and competition emerges between the symmetric and alternating shedding modes (Figure 2.6(a)). Similar mode progression was observed by Cagney and Balabani 2014 [25], for a cylinder with a 1:1 stiffness ratio of $f_{nIL} = 1 \times f_{nCF}$.

A growth was observed in the crossflow-inline phase angle as amplitudes increase during the onset of oscillations for low U^* (Figure 2.4). In this region, mode competition yields to predominantly alternating shedding, with vortices shedding from

the cylinder at close to 45° between crossflow and inline (Figure 2.6(b)). At low U^*, this shedding angle results in a strong inline component which can be observed in the absence of the larger mean drag forces which manifest for higher U^* cases under lock-in. Thus, these cases have the highest inline-crossflow phase angle, approaching 40 degrees. As the drag force builds for higher U^*, we observe a decrease in the CF-IL phase angle. Seen in Figure 2.7(a,b), this was attributed to the vortex shedding angle moving further to the side of the cylinder, leading to vortices shedding earlier in the cycle and closer in-phase with the crossflow oscillation. While the high phase angle cases had a dominant 2f component in the drag coefficient (Figure 2.8(b)), responses outside that region, with lower phase angles, were driven by 1f lift forces for low U^*, and 3f lift forces for higher U^* (Figure 2.8(a)). For low U^*, the drag force was observed to desynchronize as crossflow motion begins, appearing as a dip in the drag coefficient and a break in the previously increasing fluctuating drag frequency at $U^* = 5.75$. This aligns with the initial formation of the 3f lift force harmonic, and subsequently the peak fluctuating drag force at 2f as the crossflow-inline phase angle reaches its maximum value near $U^* = 5.7$-6.

2.4 Square prism VIV

A D-cylinder has been used in previous studies to determine the importance of the afterbody (whereby if the flat face is upstream or downstream, the forebody or afterbody is completely eliminated). However, recently it has been discovered that the D-cylinder afterbody is not needed for VIV under certain conditions by Zhao et al. [118], contrary to numerous studies indicating that the afterbody is required for either VIV or galloping ([24], [15], [79]). As opposed to the D-cylinder in the literature, a square prism has a forebody symmetric to the afterbody. For a square prism with a pure crossflow degree of freedom, the structure is known to respond with both VIV and galloping-like responses depending on the angle of attack ([13], [119]).

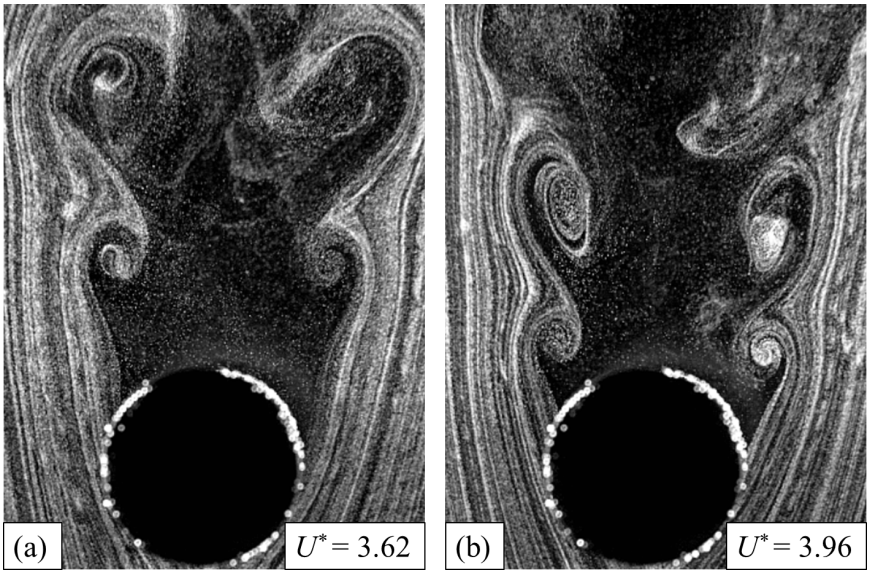

Figure 2.5. For U^* below and at the onset of oscillation, symmetric vortices are (a) shed into the far wake when the lack of oscillation prevents synchronization, then (b) attach to the afterbody and resonate the inline component of the structure. At U^* = 3.96, the oscillation is almost purely inline.

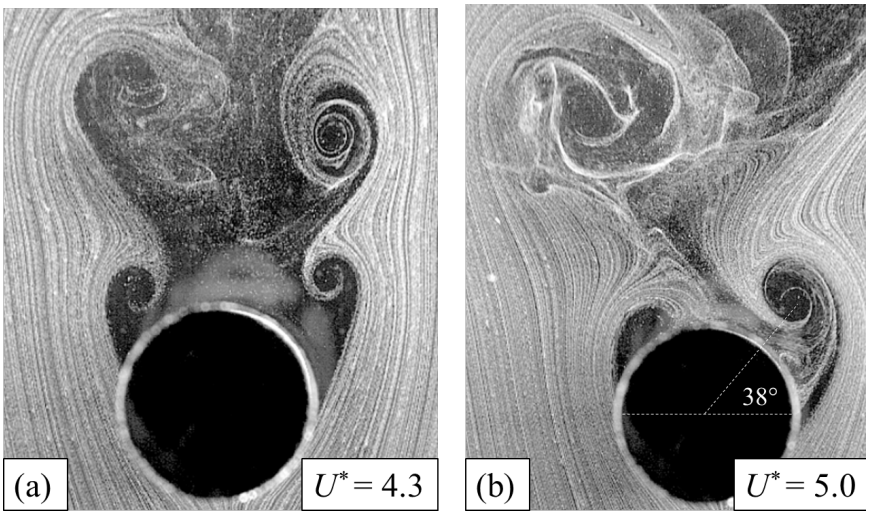

Figure 2.6. At U^* close to the onset of oscillation, the wake has a degree of symmetry but is always competitive. The shedding angle in (b) is held throughout U^* = 5-6, bringing the crossflow-inline phase angle from 14° at U^* = 5, to 39° at U^* = 5.7 and 37° at U^* = 6.

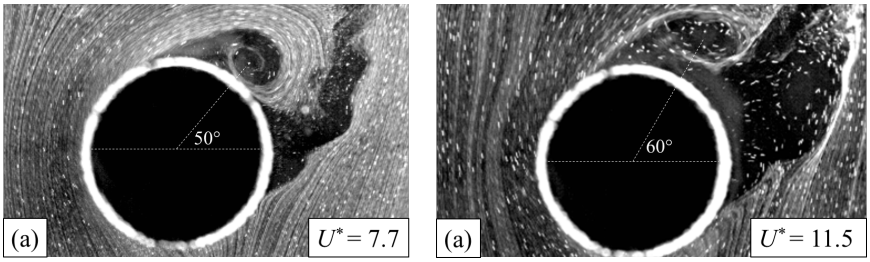

Figure 2.7. For increasing U^*, the shedding angle increases, collapsing the inline response.

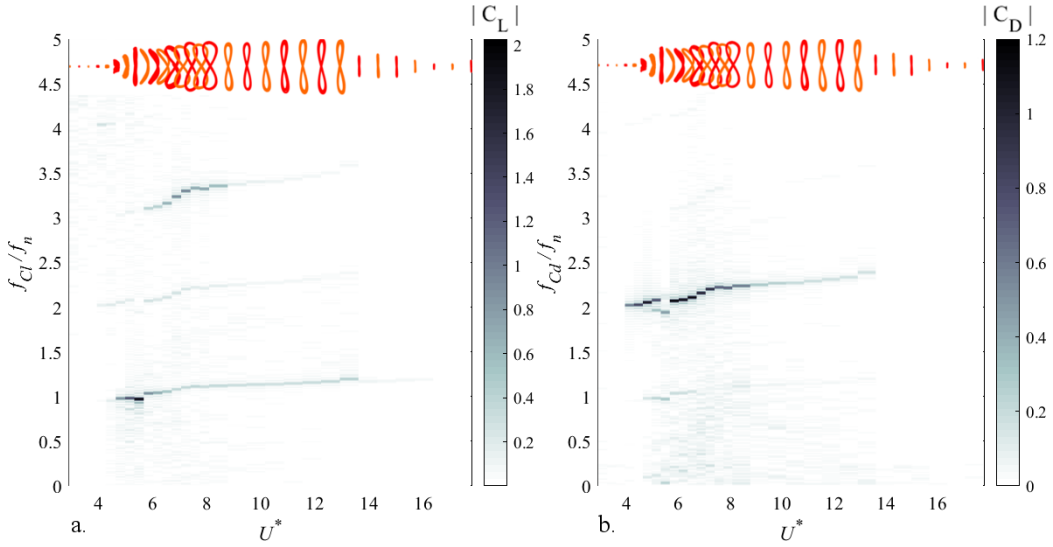

Figure 2.8. Frequency contents of the fluctuating lift and drag coefficients for the circular cylinder.

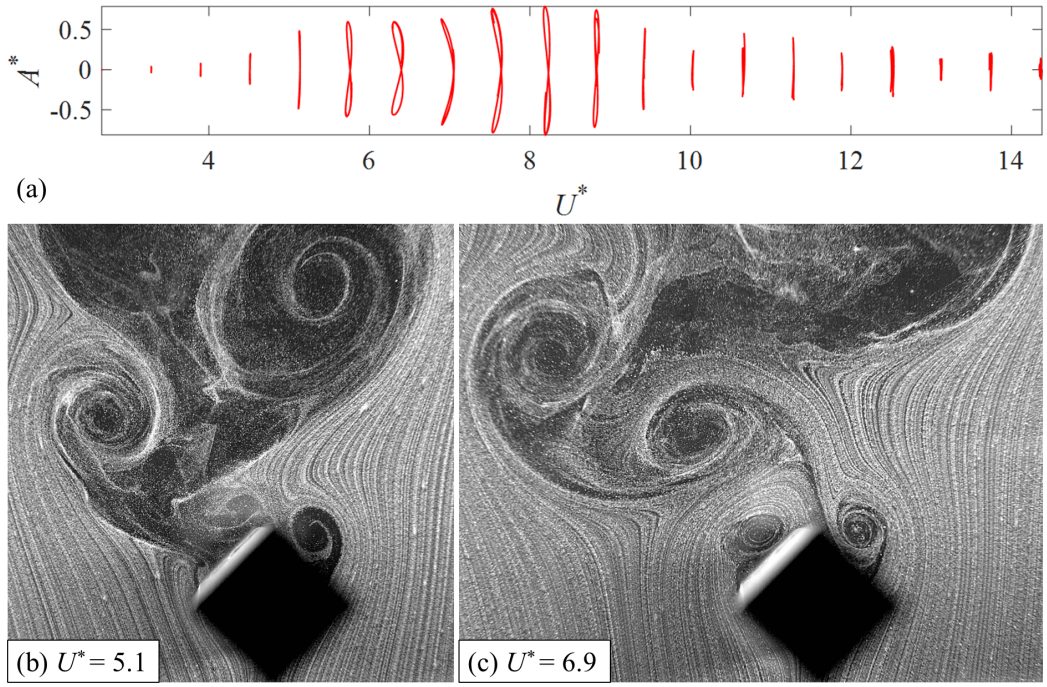

Figure 2.9. The square prism at 45° has a similar vortex-induced vibration response as the circular cylinder.

A square prism with two degrees of freedom has not been studied experimentally, and only recently been considered numerically by Zhao et al. [122][123]. Using the same methods described in the prior sections, we placed a square prism in flow for angles of attack of 0°, 22.5°, and 45°. This range encompasses all possible angles of attack, as the structure has symmetry beyond 45°.

Prior studies have observed the 1D VIV response of a square prism at 45° angle of attack. The symmetry of the prism permits shedding patterns similar to those of a circular cylinder undergoing VIV, and thus the square prism responds with classical vortex-induced vibrations across a similar U^* range as the uniform cylinder. Seen in Figure 2.9 are response orbits and sample flow visualizations for the square prism at 45°. For U^* close to the onset of oscillations ($U^* = 5.1$), 2S vortex shedding dominates the response and a high CF-IL phasing results in a crescent-shaped orbit similar to that of a uniform cylinder near lock-in. For $U^* = 6.4$ as a high amplitude example

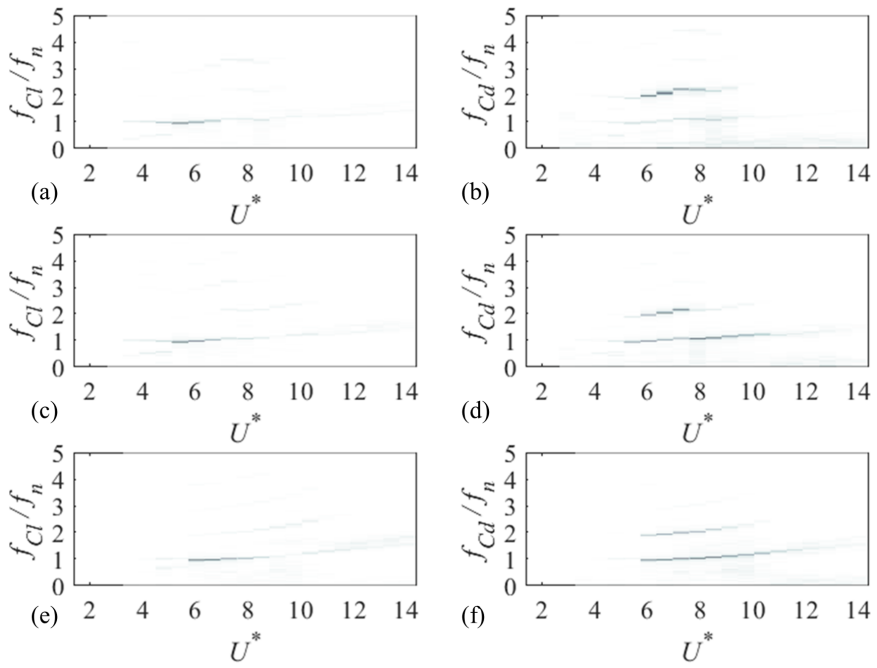

Figure 2.10. FFT of lift and drag coefficients for a square prism at (a,b) 45°, (c,d) 35°, and (e,f) 22.5°. The 22.5° response is VIV for $U^* < 8$, after which asymmetric vortex shedding from the relative motion of the cylinders drives a beat-like response due to intermittent correlation. This manifests as a reduced lift contribution relative to drag, as the oscillation is primarily driven by the drag force.

(Figure 2.9), simultaneous vortices are formed on either side of the afterbody, and both are shed at each half cycle. This is 2P vortex shedding and is well understood to be expected for low-mass cylinders at their peak amplitudes within the upper response branch ([114], [59], [31]).

The frequency contents of the fluctuating lift and drag coefficients were mapped for each U^* in Figure 2.10(a,b), with the frequency axis normalized by f_n. The lift coefficient remains near f_{nCF} throughout the lock-in region, with slight 3f contribution as both the crossflow and inline oscillation amplitudes maximize near $U^* = 7$. This region also aligns with the maximum drag coefficients which manifest with $f_{Cd} \approx f_{nIL} = 2 \times f_{nCF}$.

2.5 Prism FIV at varying angles of attack

2.5.1 The general amplitude response

In this section the general FIV response of a square prism is given for varying angles of attack. The angle of attack of the square prism was incremented from $\alpha = 0°$ to $45°$ in steps of $5°$, plus one intermittent step of $2.5°$ to capture $\alpha = 22.5°$. Figure 2.11 presents the two-dimensional trajectories of each orientation at each reduced velocity. Orbits are to-scale between the crossflow direction on the horizontal axis and inline direction on the vertical axis, allowing for direct comparison between cases. In addition, orbits are colored by their directionality, with red marking figure–eight orbits with counterclockwise lobes, and black marking single–loop orbits. No clockwise figure–eight trajectories were observed for any angle of attack or reduced velocity. The lower branch observed for the symmetric $\alpha = 45°$ case appears to be sensitive to α, and decays to single–loop orbits for $U^* > 8$ for the first asymmetric case at $40°$. This trend continues for the lower angles of $35°$ and $30°$, with counterclockwise figure–eight orbits sustained only for $U^* \leq 7$. Note the increase in asymmetry at $20° - 25°$, with the lower lobe clearly dominating the high–amplitude responses near $U^* = 6 - 8$.

Below $22.5°$ decreasing angles are progressing back towards symmetry. This region is accompanied by the collapse of the upper branch VIV response for low U^* at $\alpha < 20$. However as the upper branch collapses, a transition occurs within the lower branch to significant inline contribution, with roughly circular orbits as the inline oscillations approximately match the crossflow oscillation amplitude at $15° - 20°$. By comparing the orbits to the A^* values in Figure 2.12, this transition is more evident for the $15°$ case. If instead A^*_{10} is used (mean of the top 10% of oscillation amplitudes), the beat nature of this region is captured as an extended lower branch (Figure 2.11(b)).

At $10°$ the VIV response is almost entirely eliminated for $U^* < 10$, but occasional beat responses were noted in the oscillation for this region. Notably this angle

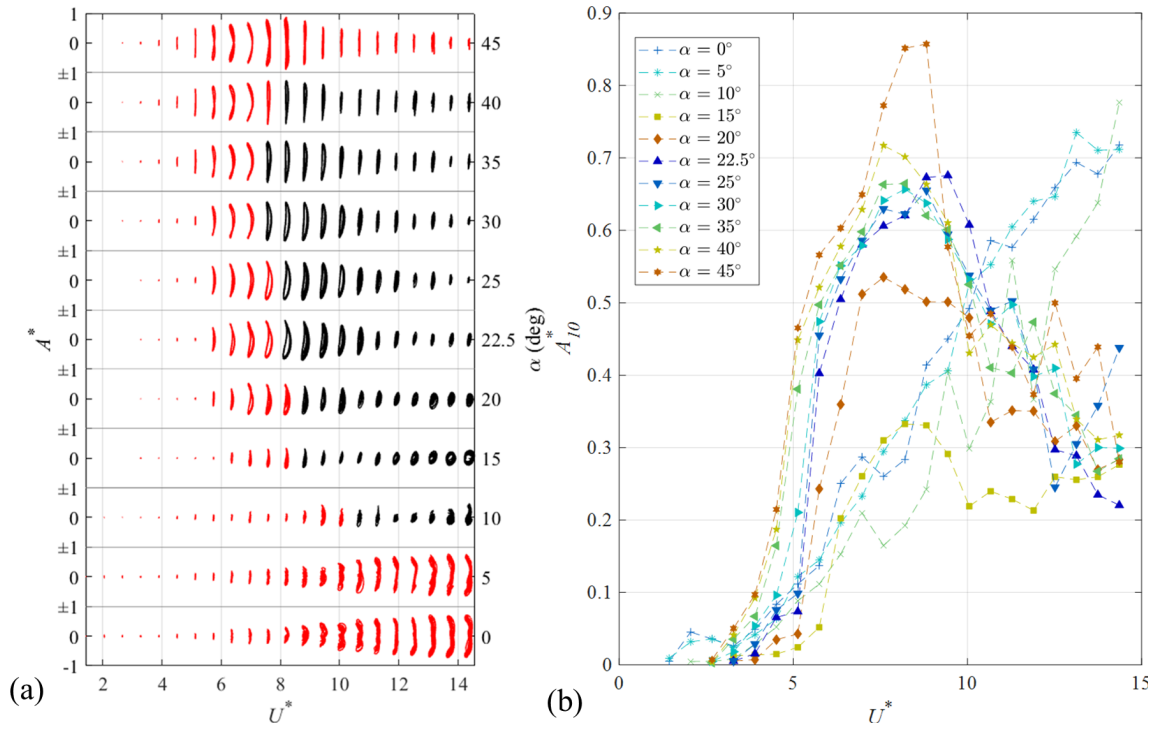

Figure 2.11. (a) The response of the square prism at each angle of attack. Trajectories are to-scale between crossflow (x) and inline (y). Red denotes counterclockwise figure–eight orbits, black marks single–loop orbits. (b) The A^* values for each angle, reported as the average of the top 10% of oscillation amplitudes.

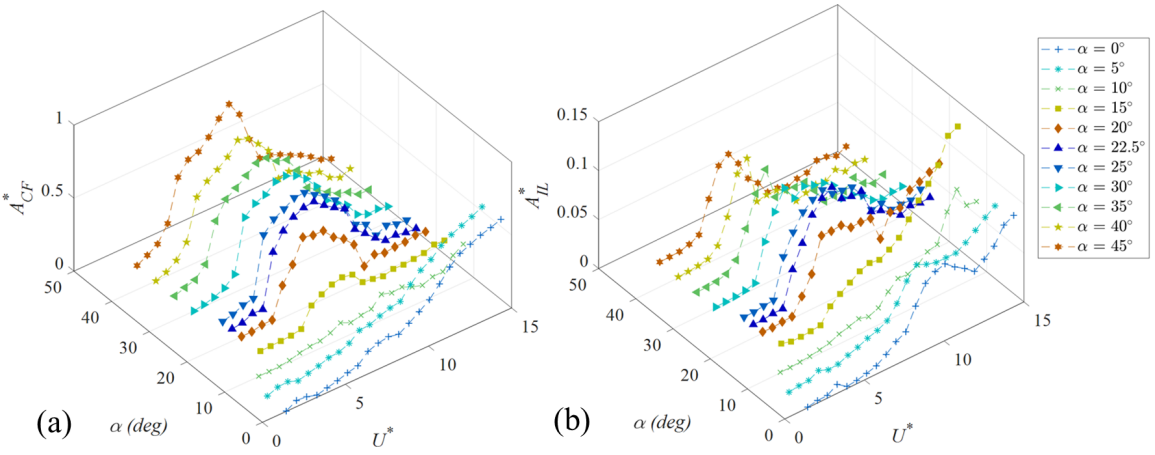

Figure 2.12. A^* for each angle of attack for (a) the crossflow direction and (b) inline. Values reported as RMS.

also marks the onset of high U^* galloping, however it was also as a beat response. This region will be discussed further in section 2.7. Finally, consistent galloping was observed for all U^* for $\alpha = 0° - 5°$. The orbits reported in Figure 2.11 are all counter-clockwise, but with a modified definition. Here a third lobe appears at the midpoint of the crossflow oscillation, which will be discussed in section 2.8. Despite no longer being figure–eight, the counterclockwise terminology is used here to denote that at the peak of the outer lobes the prism oscillates into the flow.

2.5.2 Overview of the fluid forces

For each amplitude response reported in the prior section, simultaneous force measurements were also recorded. To summarize the findings of the lift and drag forces and how they change with the angle of attack, three reduced velocities were chosen for investigation relative to the $\alpha = 45°$ case: $U^* = 5.1$ the onset of oscillation, $U^* = 8.2$ the peak amplitude response within the upper branch, and $U^* = 14.3$ the maximum velocity reported. Each case is shown in Figure 2.13, with lift coefficient FFT on the left and drag coefficient FFT on the right. Response regions are most distinct between a split at $\alpha = 20°$. Above this point the response is primarily driven by a 1f lift force at $U^* = 5.1$ and 8.2, and is disorganized at $U^* = 14.3$ (oscillations are inconsistent by this velocity for $\alpha > 20°$). Higher harmonics manifest starting at $\alpha = 20°$ for $U^* = 8.2$, culminating in the peak VIV response seen 45° for this U^*.

Below 20° a gradual transition into galloping was seen for the square prism. 0° had the clearest galloping response, with a strong odd-integer lift harmonic manifesting at each U^*. At higher α this lift harmonic increases in frequency and decreases in magnitude for each U^* sample. This is due to an intermittent beat response at 10° (the third frequency bin on the contours) which lowers the average FFT value, and is further discussed in section 2.7.

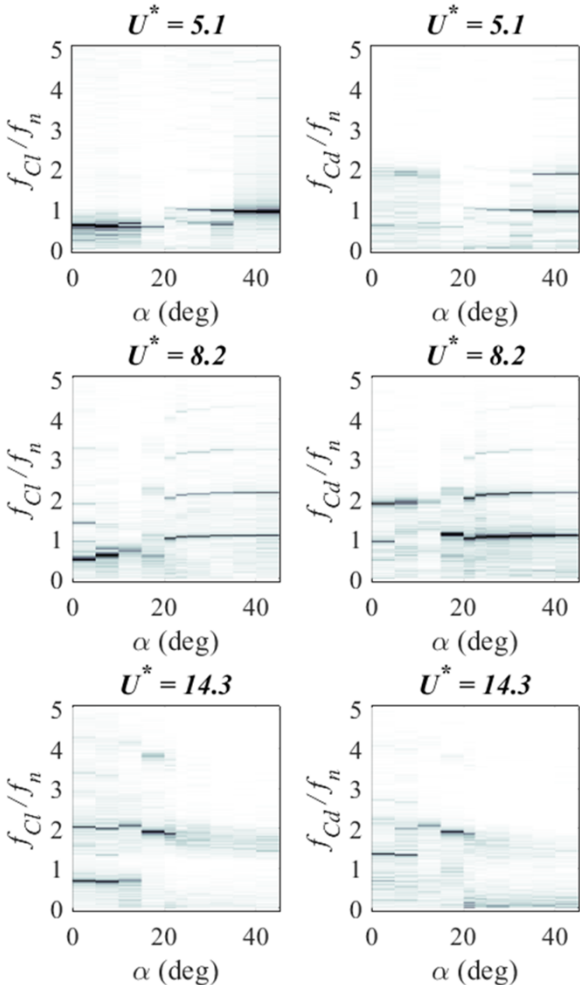

Figure 2.13. Contours of the FFT of the lift and drag force coefficients plotted agains α.

2.6 Mixed response for the square prism

As previously mentioned, the asymmetry in the figure–eight orbits is significant for $\alpha = 20^\circ - 25^\circ$ until the orbits collapse to single–loop. To examine this region, the middle angle of 22.5° will be further detailed. In Figure 2.14(a) are displacement orbits for all U^*. The response starts at $U^* = 5.8$, and sustains dual-resonance until $U^* = 8$, where the upper lobe is collapsed entirely.

At velocities below lock-in, the shear layers separate at the leading edges of the afterbody and do not interact in the near wake of the prism, resulting only in vortices far from the prism (Figure 2.14(b)). Approaching lock-in, vortex interaction is drawn closer to the afterbody of the structure. At this point, any disturbance in the flow can trip synchronization between the vortex shedding and the cylinder. Once the cylinder begins to oscillate, the relative component of flow velocity moves the separation point from the edge preceding the trailing face to the leading edge on the leading face (Figure 2.14(c)). Thus, despite being fully exposed to flow, a vortex forms on the leading face. The motion of the cylinder leads to the vortex "rolling" down the face as the cylinder reaches an oscillation apex, and on the return rolls over the preceding edge of the trailing face (Figure 2.14(d)), where it is caught by the wake and attaches to the trailing face of the afterbody.

In Figure 2.14(a), note the collapse of the upper orbit lobe for $U^* > 8$. Here a vortex was observed to still form on the leading edge and get caught on the trailing face of the afterbody, but on the opposing side (leading face of afterbody) flow separates as a jet which remains parallel to the surface, preventing vortex formation due to the relative flow (Figure 2.15(c, d)). Occasionally, the jet from the leading face of the afterbody wraps around to form a vortex on the trailing face, but despite the sporadic formation of two opposing vortices per cycle, the force from each vortex is aligned due to each vortex acting on the same face of the prism. With the forces from vortex shedding aligned, the oscillation orbit is reduced to a single lobe.

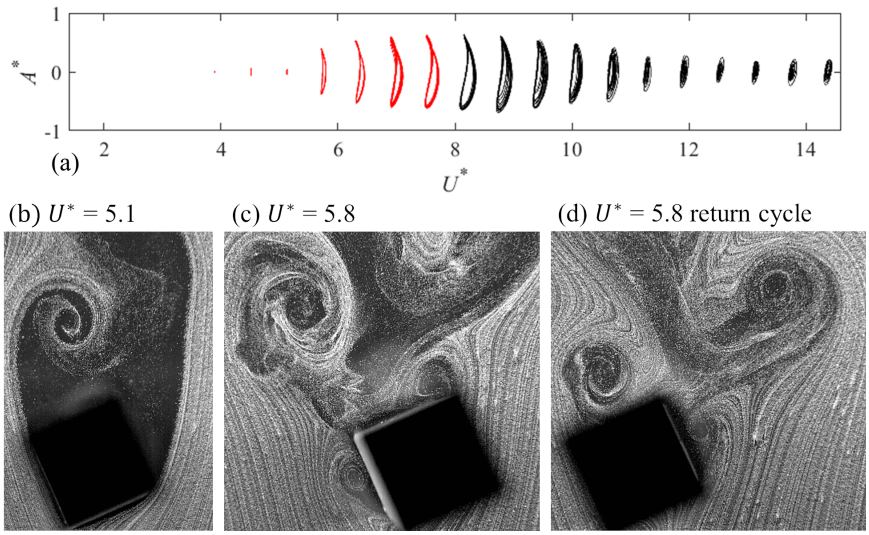

Figure 2.14. The square prism at 22.5° sees a vortex form on the leading face at $U^* = 5.8$ through 8, which is swept into the cylinder wake and acts on the afterbody of the cylinder.

Higher flow velocities are accompanied by a disorganized wake about the prism. The majority of vortices are shed into the wake of the prism, but occasional disturbances from the flow allow synchronization between the prism's oscillation and the vortex which leads to the vortex reattaching. The effect is seemingly chaotic pulses in the oscillation of the prism (Figure 2.16). The temporary synchronization is not sustained as the oscillation amplitude builds, and the beat amplitude decays towards zero until the next disturbance occurs.

The frequency contents of the fluctuating lift and drag coefficients were mapped for each U^* in Figure 2.10(e,f). The transition from VIV to a beat-like response manifests in the lift and drag coefficients as a region of lock-in with $f_{Cl} \approx f_{nCF}$, but the main lift harmonic at 1f decays as the lower response lobe collapses at $U^* = 8$, while a subharmonic in the drag component continues to act at approximately $0.5 f_{nIL}$ ($f_{nIL} = 2 \times f_{nCF}$). Thus this indicates that the extended response branch consisting of single-loop orbits is primarily being driven by a component of the drag force acting in the crossflow direction due to the asymmetry of the prism.

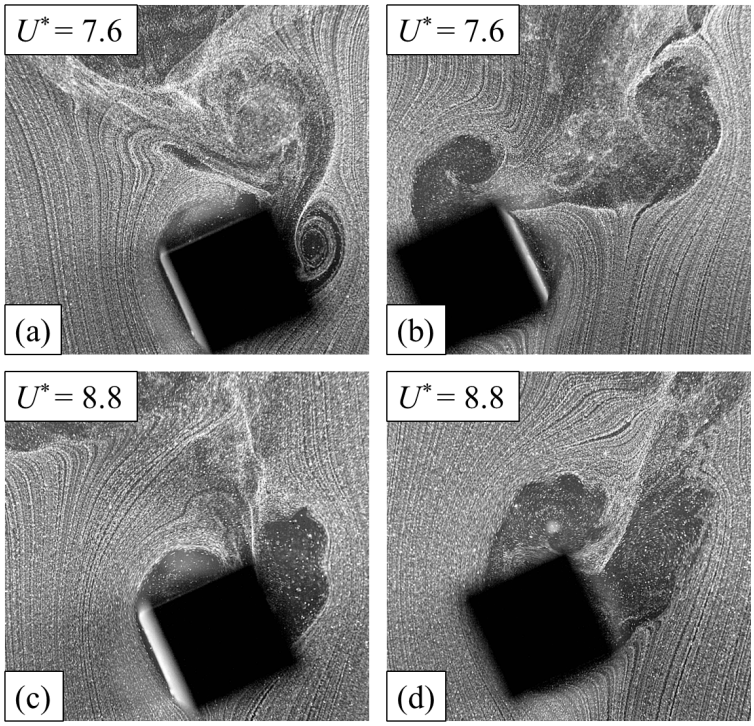

Figure 2.15. The square prism at 22.5° is primarily driven by the vortex shedding from the leading edge of the leading forebody face, which reattached to the trailing face of the afterbody. Occasion nonuniformities in the flow trigger shedding an opposing vortex to form on the same trailing face of the afterbody, bringing the forces into phase despit having opposite vorticity. Thus in the absence of any opposing shedding forces the orbit collapses into a single lobe.

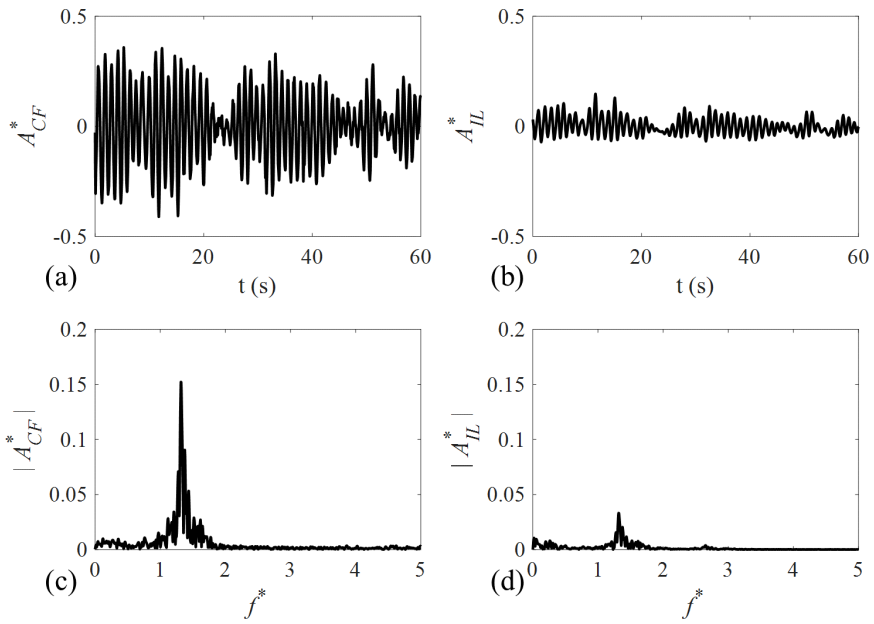

Figure 2.16. Crossflow (a,c) and inline (b,d) displacements and FFT for the prism at 22.5° and $U^* = 11.3$, where the response is collapsed into a single lobe.

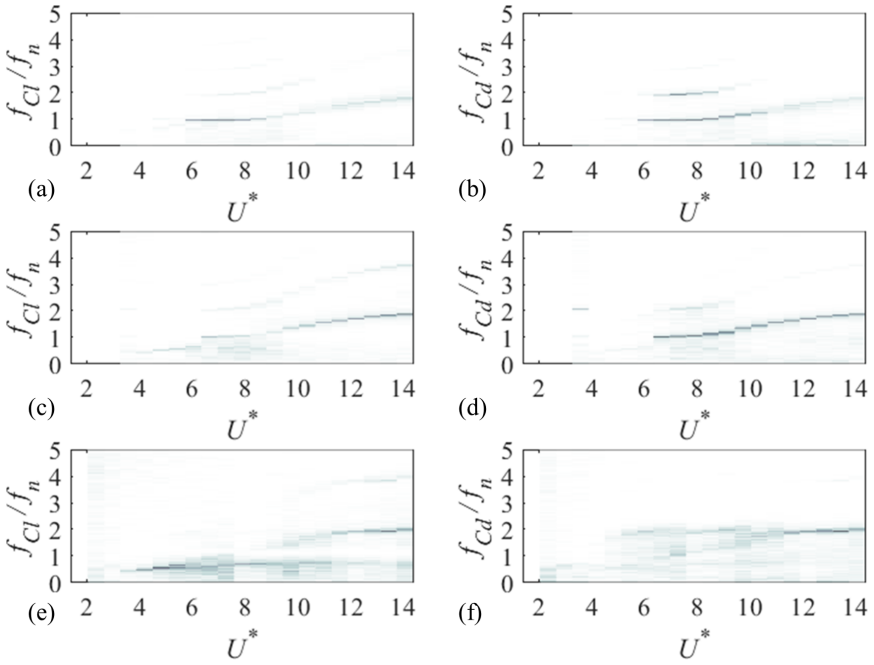

Figure 2.17. FFT of lift and drag coefficients for a square prism at (a,b) 20°, (c,d) 15°, and (e,f) 10°.

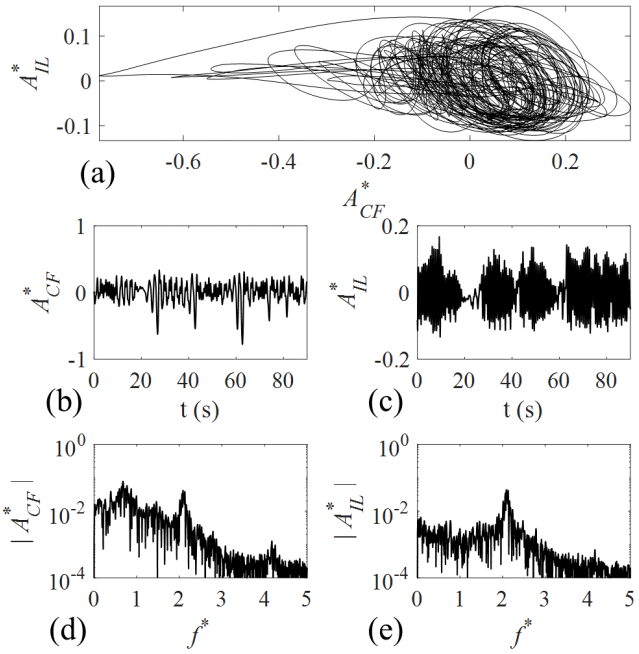

Figure 2.18. Sample case of the beat response for the prism at 10° and $U^* = 14$. (a) displacement orbits, (b,c) crossflow and inline A^* time series, (d,e) FFT of the displacement time series.

2.7 The transition to galloping

Below 22.5°, the VIV response was very sensitive to α and dropped from a maximum amplitude of $A^*_{10} = 0.68$ at 22.5° to a local maximum of $A^*_{10} = 0.21$ by 10°. (Figure 2.11(b)). As seen in Figure 2.11(b) though, the A^*_{10} peak at $U^* = 7$ for 10° is indeed only a local maximum within the traditional lock–in region. At higher velocities, a galloping-like response was recorded which eventually surpasses this amplitude. At angles of attack of5° and below the local maximum is not observed due to a more consistent galloping response throughout the U^* range. Thus, angles of attack ranging from 10° to 20° mark the transitory range from a VIV response to galloping.

As a sample of the beat response which occurs during the transition from VIV to galloping, the orbits, time series and FFT of A^*_{CF} and A^*_{IL} for the prism at 10° and U^* = 14 are shown in Figure 2.18. The oscillation response comprised of both (a) circular

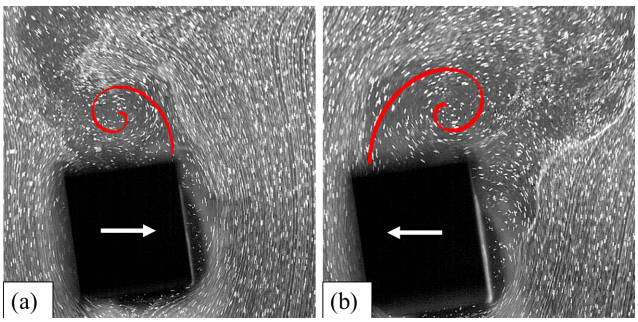

Figure 2.19. Flow visualization for the prism at 10° and high U^*, where $U^* = 14$. The response oscillation response driven by a build–up in the strength of the vortex being shed in orientation (a), which once shed accelerates the prism in direction (b), towards the face of the covex to flow.

orbits and (b) a build–up in the crossflow component jolting the cylinder towards the direction of α (the face convex to flow). These modes are overlaid in Figure 2.18(a), and appear as beat responses in Figure 2.18(b,c). As the prism moves side to side, each vortex shed per side attached to the face of the afterbody convex to flow, driving a circular orbit. This mode of vortex shedding continues as the amplitude in both crossflow and inline decays. Intermittently the prism was sufficiently still to permit the vortex in the Figure 2.19(a) orientation to grow in strength. In the sample time series, this occurred at $t = 20$ s, 55 s in Figure 2.18(b,c). Once shed, this larger vortex accelerated the prism towards the convex face (the orientation in Figure 2.19(b)) before reaching a maximum amplitude ranging between A^*_{CF} =0.5–0.8. After each of these large amplitude responses the oscillation decays back towards zero, repeating the beat response. As the response is primarily driven by vortices detaching from the convex face of the prism, it is similar to the high U^* response for the prism near 22.5° in that the drag force is dominant and manifests with a component in the lift direction as well. This results in the clear 2f band reported in the respective lift and drag force FFT Figure 2.18 (d) and (e), respectively.

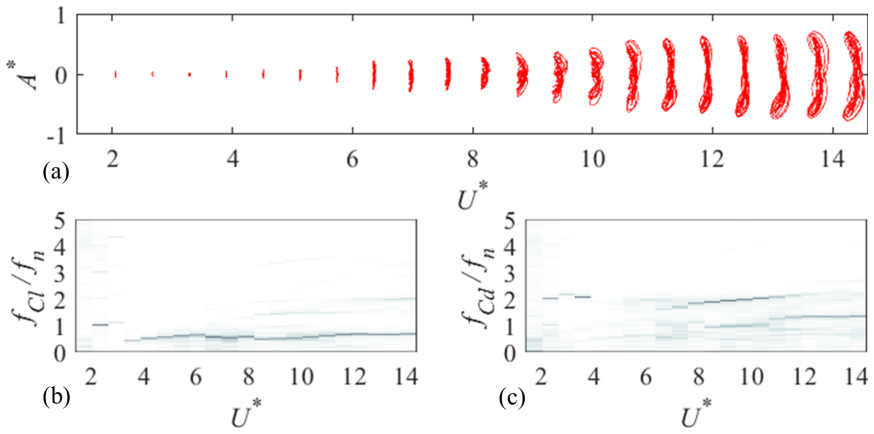

Figure 2.20. A square prism at 0° angle of attack encounters a vortex wrap around the sidefaces and attach to the afterbody, yielding a kink in the crossflow oscillation and a third lobe in the orbit.

2.8 The galloping prism

For angles of attack below the transitory 10° to 20° region, the amplitude response shows little change between 5° and 0° (Figure 2.11(a,b)). Therefore the 0° prism will be used as a sample to examine this response regime. In the literature, a square at 0° with crossflow is well known to undergo galloping, and a similar response was observed in the present work given the inclusion of inline freedom. Throughout the traditional lock-in region, the amplitude response for a prism at 0° or 5° was much smaller than for any case at a higher angle attack. Though, for all U^* the amplitude was seen to increase for increasing velocities and no upper bound was observed for $U^* < 15$. Orbits for velocities below $U^* = 8$ were predominantly side-to-side, with an inline counterclockwise transition at the peak crossflow displacements. While not a clear figure–eight orbit, we once again use the counterclockwise nomenclature to mark the prism oscillating into the flow at either lobe.

For the lower velocity cases, flow which encounters the bluff leading face of the prism separates at the leading edges, creating vortices which act on the sides of the cylinder as well as the afterbody as they convect downstream (Figure 2.21(a, b)).

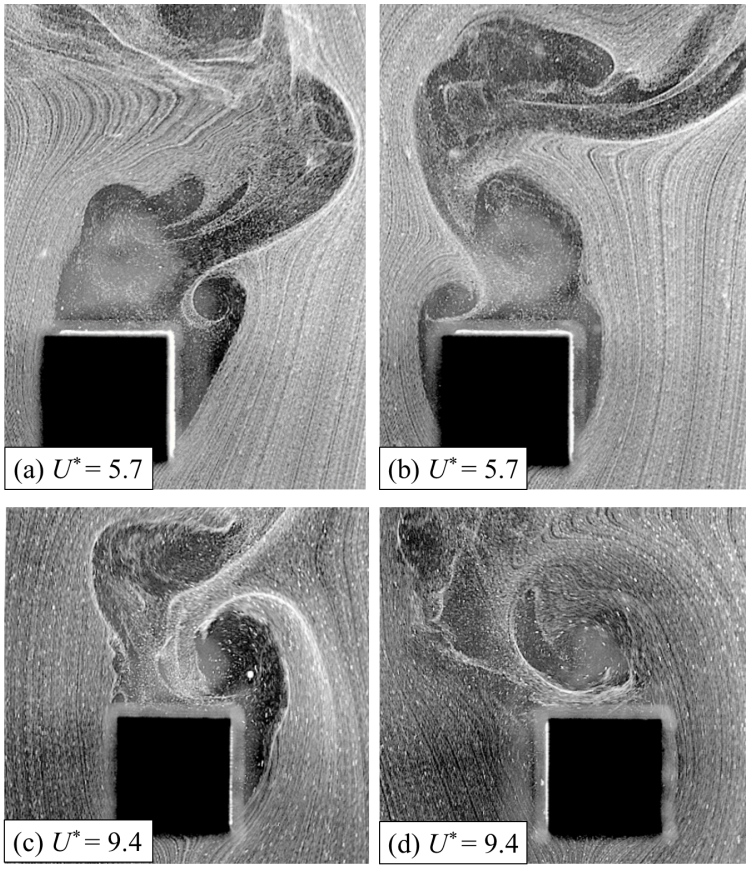

Figure 2.21. A square prism at 0° angle of attack encounters a vortex wrap around the sidefaces and attach to the afterbody.

This process is of course symmetric at 0° and resembles 2S shedding. Much like the 22.5° case, for U^* below synchronization the vortices are shed into the wake, but the pressure differential is not yet sufficient to draw them against the afterbody.

It was noticed that there was a limited U^* range which responded with a significant inline component as the prism crossed the midpoint of crossflow displacement. This range, approximately $U^* = 8$–12, corresponded to vortex sheddings which remained attached to the afterbody progressively longer through the oscillation cycle for increasing U^*. Whereas the 2S regime sheds vortices which act on the sides of the prism (Figure 2.21(a,b)), at higher U^* for 0° the prism encounters additional fluid forces from the vortices rolling onto and detaching from the afterbody. The force from the afterbody detachment acts normal to face of the prism, purely inline at 0°. (Figure 2.21(c,d)). At the midpoint of the cycle, the afterbody vortex is shed. This gives a strong inline force acting on the cylinder at the midpoint of each cycle, resulting in a third response lobe (Figure 2.21(a)). By following the orbit, one can see that for this type of response one outer lobe must be clockwise and the other counterclockwise, with the clockwise orbit resulting in a crossflow traversal downstream of the third lobe. This process was found to have competing asymmetry, with the clockwise directionality occasionally reversing. These reversals can be seen as inner loops within the outer lobes in Figure 2.21(a)

The square prism at 0° is a good example of galloping for crossflow degree of freedom structures, but with additional inline freedom the forces become more disorganized. In Figure 2.23 are the frequency contents of the lift and drag coefficients for this orientation. As expected for a galloping-type response, there is no clear lock-in region, but the previously discussed inline response between $U^* = 8$–12. In this region, resonance in the inline direction creates the new synchronization region which is sustained only while f_{Cd}/f_n is close to 2, due to the imposed 2:1 ratio between f_{nIL} and f_{nCF}. Outside this region at both lower and higher U^* the response is closer to

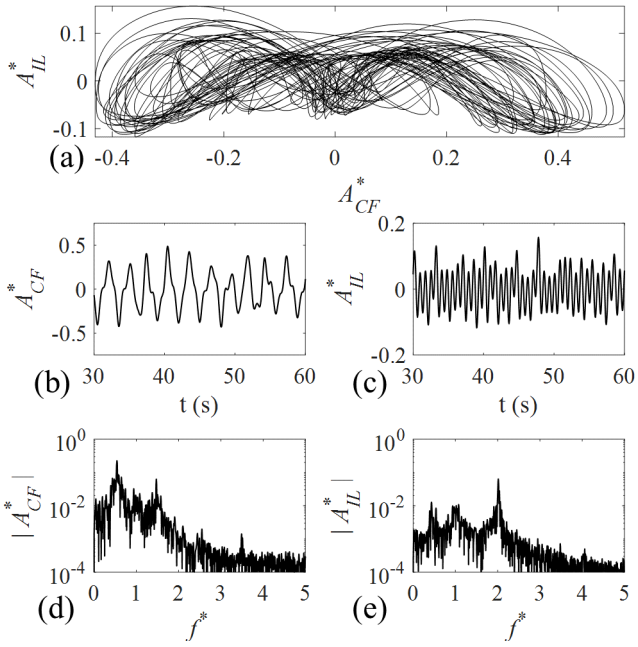

Figure 2.22. Sample case of the beat response for the prism at 0° and $U^* = 10$. (a) displacement orbits, (b,c) crossflow and inline A^* time series, (d,e) FFT of the displacement time series.

traditional galloping. For instance, immediately before the inline resonance at $U^* = 8$, the dominant lift harmonic acts at approximately $0.61 \times f_n$ and drag synchronizes at $1.78 \times f_n$, almost three time the lift frequency.

Previously described for a galloping square prism with pure crossflow freedom [16], the inline resonance we observed here due to afterbody vortex reattachment is theorized to contribute to the galloping kink for a structure with two degrees of freedom. The cylinder suddenly moves from a side-to-side oscillation to one with additional inline synchronization. Vortex reattachment on the trailing face momentarily slows the crossflow movement of the cylinder as the vortex grows and sheds, propelling the prism upstream as it does so. This gives additional lobes in the oscillation orbit which which are primarily drag–driven and due to this phenomenon occuring only at the midpoint of each cycle, explains the odd integer harmonics within the lift force.

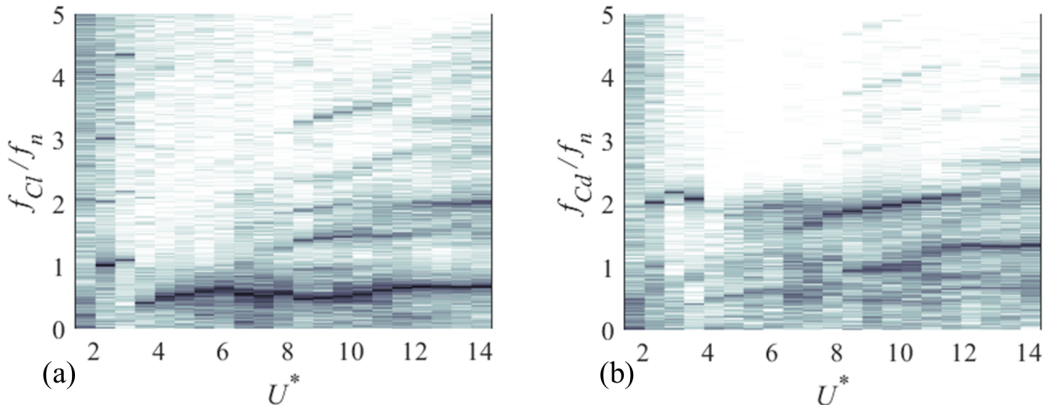

Figure 2.23. FFT of lift and drag coefficients for a square prism at 0° angle of attack is driven to galloping, with odd-integer harmonics in the range of $U^* = 8$–12 manifesting from a vortex periodically attaching to the afterbody of the cylinder.

2.9 Response of a triangular prism

Both square and triangular prisms are known to exhibit VIV and galloping-like responses depending on the angle of attack when they are free to oscillate in the crossflow direction only. The inclusion of a dual-resonance condition could introduce changes on the observed response. With a pure crossflow degree of freedom, a triangular prism at $\alpha = 60°$ is known to exhibit a galloping-type response. We used the same prism from Seyed-Aghazadeh et al. [91] with the two degree of freedom mounting described in prior sections. To achieve dual-resonance more easily, we set $f_{nIL} = 2 \times f_{nCF}$. The same methodology as with the circular cylinder was repeated here, with the displacements, forces, and wake visualization all captured simultaneously across the U^* range. However, mechanical limits on the bearings limited the maximum U^* tested to approximately $U^* = 10.75$, where for higher reduced velocities the amplitude of oscillations surpasses the capability of the mounting. An angle of attack range of $\alpha = 0° - 60°$ was captured, encompassing all unique angles for this geometry. Below 30° no oscillations were recorded and as such we focused on the angles 30° and higher.

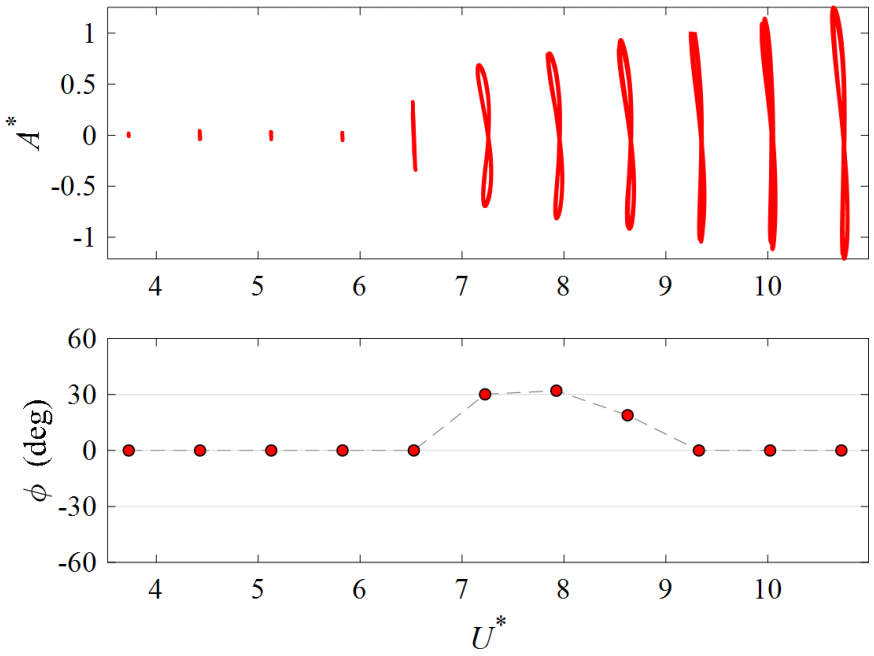

Figure 2.24. Orbits and CF-IL phase angle of a triangular prism at an angle of attack of $\alpha = 60°$.

For a triangular prism with an angle of attack of $\alpha = 60°$, all U^* for which the prism oscillated exhibited CCW figure-eight orbits. We observed the greatest inline amplitude contribution (highest CF-IL phase angle) was 30° (equal to one-half the normal angle of the afterbody) at $U^* = 7.2$ and 7.9 (Figure 2.24). Oscillation began at $U^* = 6.5$, the first reduced velocity for which vortices attach to the symmetric afterbody (Figure 2.25(b)). For asymmetric cases below 60°, the angle of attack introduces a leading and trailing face to the afterbody, moving the separation point of the leading face upstream, and the separation point of the trailing face downstream. For example at 50° and 40° in Figure 2.25(c,d), the vortex attaches further downstream on the trailing face of the afterbody for decreasing α, for cases at the same U^*. At 30° the vortex on the side of the trailing face of the afterbody is entirely detached from the prism (Figure 2.25(e)), and no oscillations are observed. This makes the amplitude seen at 60° significantly reduced for lower angles of attack at the same U^*.

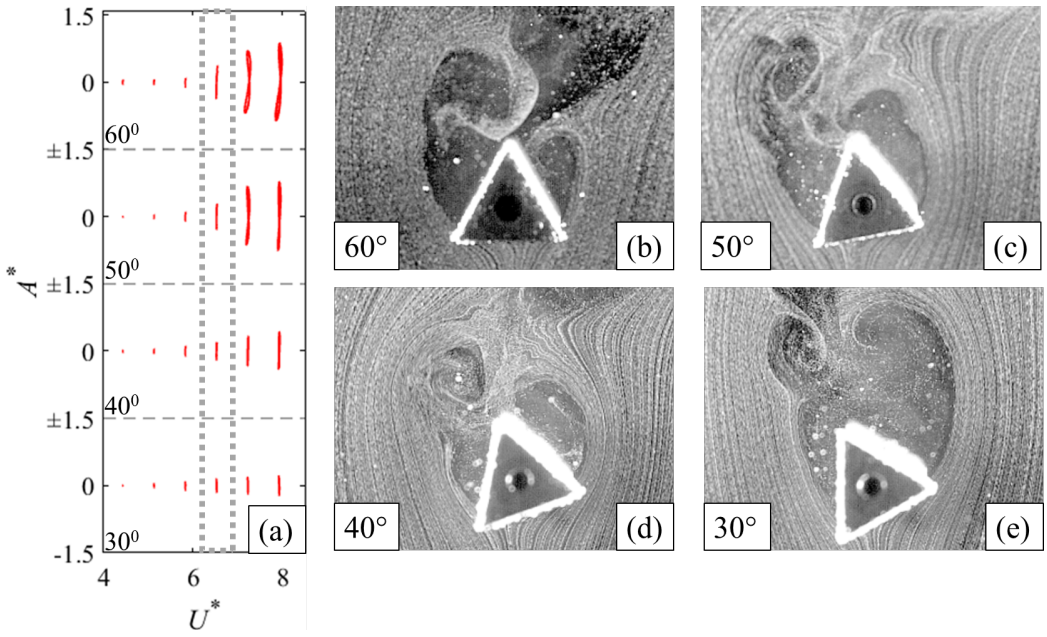

Figure 2.25. Orbits and shedding patterns for varying angles of attack.

All orientations were ran for U^* until the maximum amplitude of the mounting was met. As α decreases, the asymmetry introduces as lopsidedness to the lobes of the figure-eight orbit, but all cases do retain a degree of figure-eight motion instead of collapsing into single-loop orbits (Figure 2.26). At α below 60°, a galloping-type response is observed, with oscillations beginning at a higher U^* than for the symmetric case (Figure 2.26), and increase in amplitude for all U^*. Note the asymmetry in the response lobes for decreasing α and increasing U^*. The asymmetric prisms induce a relative component of flow as the prism oscillates. Depending on towards which direction the prism is moving, the relative flow either detaches at the trailing edge of the prism (Figure 2.27(a)) or (b) the leading edge. Detachment from the trailing edge permits a region of sustained vortex growth attached to the trailing face of the prism, due to that face being convex to flow. This increases the forces on that side of the prism and thus expanding the lobe on that portion of the orbit (Figure 2.26). On the return stroke, the opposing face is increasingly concave to the flow for decreasing

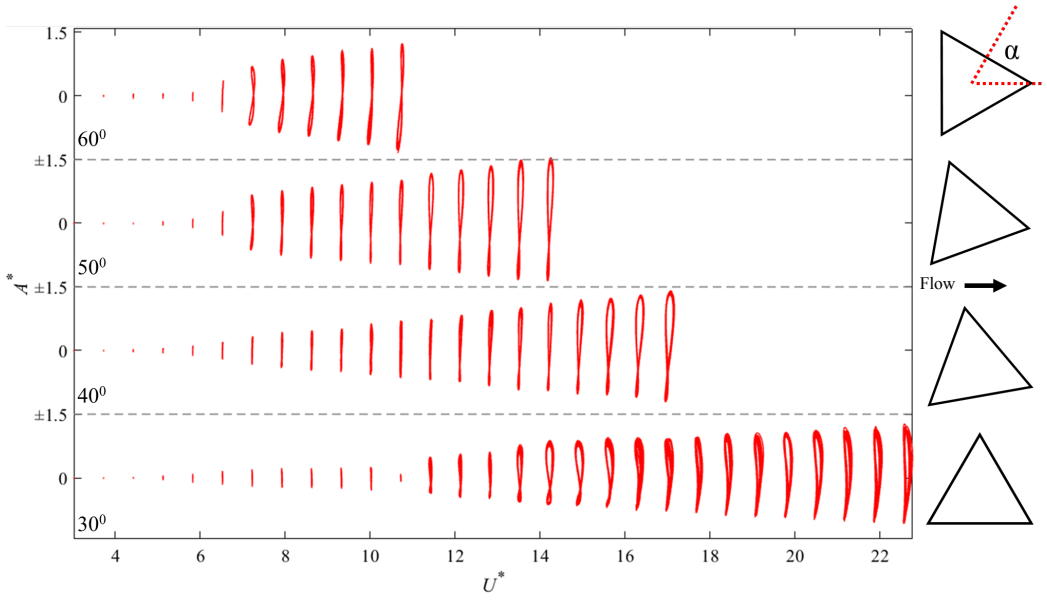

Figure 2.26. Orbits of a triangular prism for all angles of attack where oscillation was observed. α below 30° were also tested but no oscillations were observed.

α and increasing U^*, which limits vortex formation throughout that half of the cycle. These two mechanisms: increased vortex growth on the convex face, and decreased on the concave face, are what manifests as increasingly asymmetric lobes within the two-dimensional orbits.

2.10 Conclusions

New results on the flow-induced oscillations of square prisms with two degrees of freedom were presented. When permitted an inline stiffness two times that of the crossflow component, vortices align with the normal angle of the afterbody during synchronization, resulting in a vortex-induced vibration response for the symmetric square at 45°. For the prism at 22.5°, the angle of relative velocity aligned with the angle of the afterbody beyond $U^* = 8$, leading the shear layer to remain attached on the leading face of the afterbody, but also to vortex formation on the trailing face of the forebody. Combined, this leads to asymmetric intermittent 2S shedding,

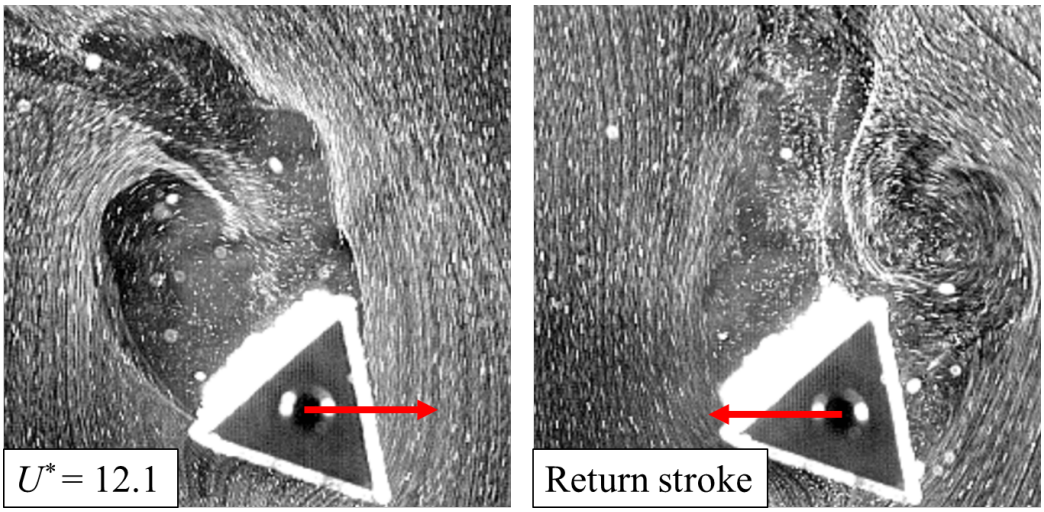

Figure 2.27. Asymmetry in the afterbody permits (a) sustained vortex growth on the trailing face, and (b) sooner separation on the leading face of the afterbody. Shown here for $U^* = 12.1$ and $\alpha = 40°$.

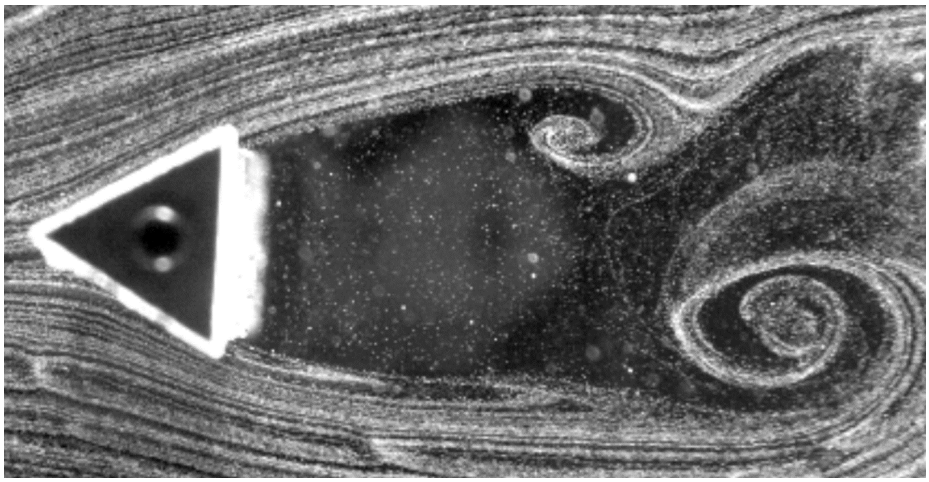

Figure 2.28. For a triangular prism at low angles of attack, vortices are shed far from the body and no oscillations are observed.

where both vortices are acting on the trailing face of the afterbody. This collapses the oscillation orbit into a single lobe, as opposed to the symmetric figure-eight orbits seen for symmetric cylinders undergoing VIV or galloping.

For angles of attack below a transitory phase between $\alpha = 10^\circ$ to 20°, stable galloping occurs. Of interest, prior literature considered the galloping kink for a square prism at 0° angle of attack, which has been studied since Bearman et al. 1987 [16] and known to result in odd-integer lift harmonics over a limited U^*. Shown here experimentally for a system within additional inline freedom, vortex shedding starts at the leading edge of the forebody, and the vortices curl around the side faces of the cylinder and attach to the afterbody. The shedding point occurs at midway through the crossflow cycle, yielding inline resonance due to this additional synchronization, but only for $U^* = 8$–12. Mapped in 2D CF-IL space, the galloping kink manifests as a three-lobed orbit with competing clockwise directionality at the outer lobes.

CHAPTER 3

VORTEX–INDUCED VIBRATION OF SPAR PLATFORMS FOR FLOATING OFFSHORE WIND TURBINES

In this chapter, a floating model spar buoy is moored in flow and the nature of flow-induced oscillations for this structure is examined. This chapter has been published in Carlson, D.W., Modarres-Sadeghi, Y. (2018). Flow-induced oscillations of a floating moored cylinder. Wind Energy, 2018:1-8 [27].

3.1 Introduction

Offshore wind energy is well proven for depths shallow enough to permit fixed structures, but floating systems open vast swathes of ocean space, especially in locations where depth quickly exceeds 100 m within a few kilometers of shore [95]. Several concept designs have been proposed for a floating offshore wind turbine (FOWT)([29], [62], [63]) One of the proposed designs for a FOWT is a spar buoy design. This is the type of platform used by the first FOWT array prototype by Hywind Scotland [68]. Using a high aspect ratio cylindrical hull counterweighted with cement ballast, these platforms offer stability for a broad spectrum of wind and wave conditions (Figure 3.1 (a)). These traits are amenable to industrial design goals: ease of fabrication, reduced material intensity, and simplicity of installation [95]. It is known that any uncontrolled vibration in FOWTs could have significant impact on the turbine's mechanical and electrical systems [97], and therefore, vibration suppression in spar type FOWTs is an active field of research and several different suppression ideas have been proposed ([106], [36]).

The long circular body of a spar buoy results in shedding of vortices in the wake of the hull. Since the hull is flexibly-mounted (connected to mooring lines), it could oscillate because of the fluctuating flow forces that are caused by the shed vortices. These type of oscillations have been observed and very well studied for a flexibly-mounted circular cylinder free to oscillate in only one (1 DOF) or two (2 DOF) degrees of freedom, and they are called vortex-induced vibration (VIV). Bearman [13], Sarpkaya [86], and Williamson and Govardhan [113] give comprehensive reviews on VIV of 1 DOF systems. Dahl et al. [30], among others, discuss 2D VIV with some details.

When the frequency of vortex shedding becomes equal to the natural frequency of a flexibly-mounted cylinder free to oscillate in the crossflow (CF) direction (i.e., the direction perpendicular to the direction of flow), the structure starts to oscillate with an amplitude of around one cylinder's diameter. Once the oscillations start, the shedding frequency and the oscillation frequency of the system will stay equal to each other over a range of reduced velocities— a dimensionless flow velocity defined as $U^* = \frac{U}{f_n D}$, where U is the flow velocity, D is the cylinder's diameter, and f_n is the structure's natural frequency in still water. Oscillations are observed over this range of reduced velocities, which is called the lock-in region.

If the cylinder has 2 DOF, in the CF and inline (IL) directions (i.e., the direction of the flow), it can oscillate in both directions. The frequency of oscillations in the CF direction will be the same as the shedding frequency and in the IL direction twice the shedding frequency (the fluctuating IL force will have a frequency twice that of the fluctuating CF force). The 2:1 frequency ratio results in a figure-eight–type trajectory for the cylinder's oscillations. The amplitude of oscillations in the CF direction in a 2 DOF system is slightly larger than the equivalent 1 DOF system, and the amplitude of the IL oscillations is around 0.2 to 0.3 times the cylinder's diameter [59]. The additional degree of freedom in the IL direction has significant effects on the CF

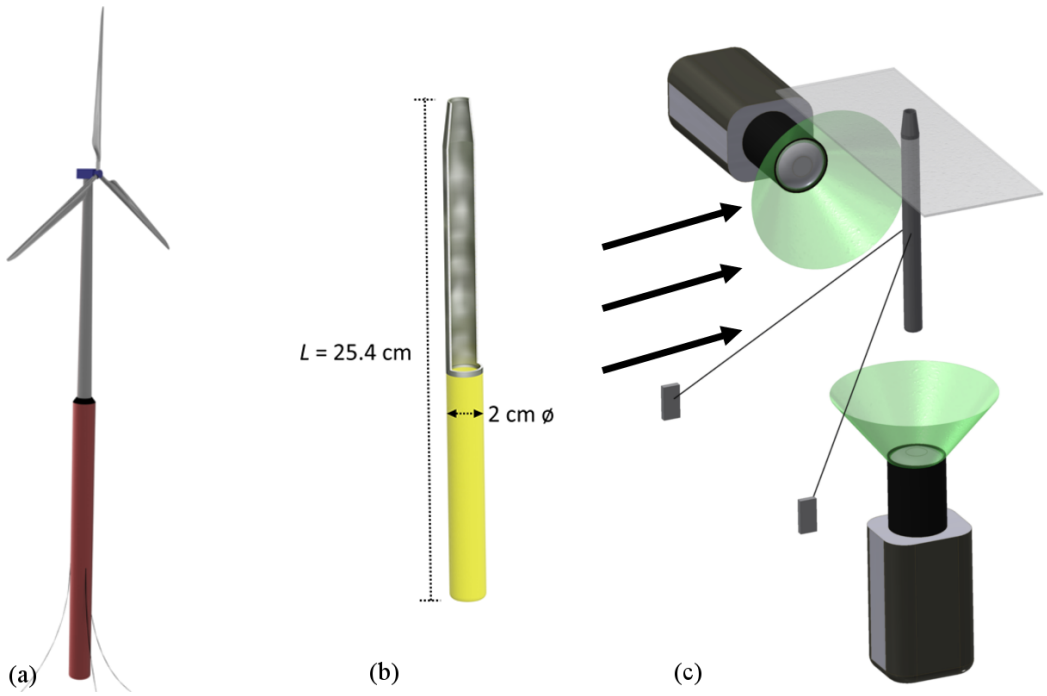

Figure 3.1. (A) To-scale drawing of typical spar platform dimensions compared with the NREL 5-MW offshore reference turbine. (B) Dimensions of the model spar length and diameter, together with (C) a schematic of the experimental setup. Note camera orthogonality for capturing 3-dimensional oscillating response.

response besides the increase in the amplitude. Dahl et al. ([30], [31]) observed a relatively large contribution of flow forces in the CF direction at 3 times the main frequency of oscillations, when the figure-eight trajectory followed a counterclockwise (CCW) direction (i.e., the cylinder was moving upstream at the extremes of its CF path). This higher harmonic component can result in a dramatic decrease in fatigue life of flexible cylinders undergoing VIV and thus poses a threat to the safety of systems undergoing VIV [73].

Vortex–induced vibration of a low aspect ratio cylinder has been studied as well. Goncalves et al. [44] and Goncalves and Fugarra [45] experimentally analyzed a surface-piercing floating cylinder free to oscillate in the CF and IL directions with a mass ratio of $m^* \approx 1$ (defined as $m^* = \frac{m}{\rho V}$ where m is the moving mass, ρ the

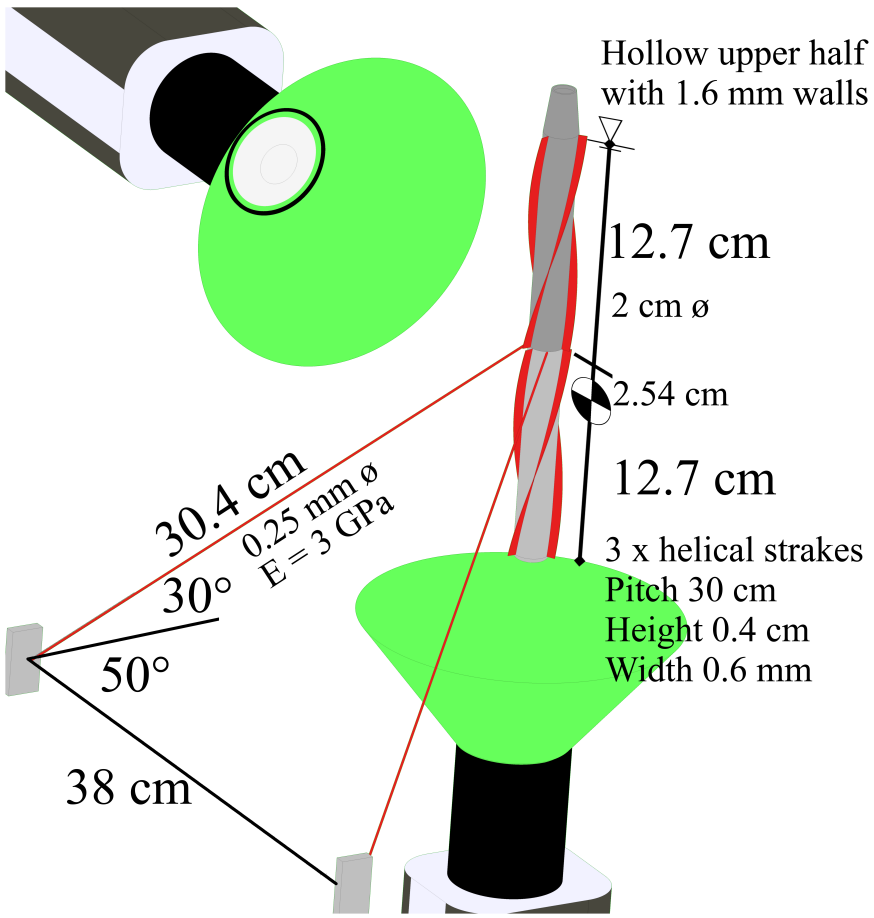

Figure 3.2. Dimensions of the floating cylinder and moorings, where the moorings are monofilament nylon and the hull is VeroWhite RDG835. The optional strakes are included, with variations on the design including a bare cylinder and partial strake coverage on the top and bottom. The free surface is marked, with the lower portion being submerged in a recirculating water tunnel.

fluid density, and V the displaced fluid volume). They focused on small aspect ratios of $L/D < 2$. The natural frequencies of the system were equal in the CF and IL directions, resulting in a 1:1 structural frequency ratio. During the lock-in region, they observed a 2:1 oscillation frequency ratio, meaning that the IL oscillations coincided at twice the frequency of the CF oscillations, resulting in a figure-eight–type trajectory for the response. They [45] concluded that VIV disappears only for very small aspect ratios of $L/D < 0.2$.

In the present work, we study VIV of spar buoy–type FOWTs by conducting experiments on a small-scale model. The goal of this study is twofold: (1) to observe VIV in a spar buoy–type FOWT, where the spar is a high aspect ratio, low mass ratio cylinder, supported only at one point along its length by mooring lines, and (2) to pinpoint the region along the length of the cylinder where the flow excites the cylinder, which is a critical piece of information for future VIV suppression methods for spar-buoy–type FOWTs.

3.2 Experimental setup and method

The experiments were conducted in a recirculating water tunnel (Figure 2.2) with a test section of 1.27 × 0.5 × 0.38 m and a turbulence intensity below 1%. For additional discussion on the flow quality e, see Seyed-Aghazadeh et al. [91]. A small-scale model of a spar-type floating turbine was designed and built using 3D printing techniques. The material was VeroWhite RDG835 at a density of 1.17 g/cm^3. The model was a scaled down version of the Hywind Scotland demo spar platform by a factor of 1:470 with respect to the original design [68]. Its length was L = 254 mm and its diameter D = 20 mm (Figure 3.1 (B,C)) to match the aspect ratio of the full-scale turbine [68] at L/D = 12.8. All hull variations were designed such that the center of mass of the assembly matched the metacentric height (distance between center of

mass and the mooring location) of the Hywind spar platform, with the ballast portion shifted to account for the density of the material.

The model was moored in the test section via two upstream strands 120° separated, attached about the center of mass of the model and anchored to a submerged rigid frame of acrylonitrile butadiene styrene plastic with tapered leading edges. The material used for the cables was monofilament line with a diameter of 0.25 mm. The third mooring cable, which would be slack and uninfluential under a fixed flow orientation, was excluded to allow clear observation of the wake. Figure 3.1 (c) shows a schematic of the experimental setup. The displacements of the system were recorded using a Phantom Miro M110 high-speed camera facing the bottom of the spar platform, synchronized with a Panasonic Lumix DSLR camera at the side window to record pitching movement. Both camera placements are shown in the figure with mock fields of vision. Footage was collected at 100 frames per second for 30-second series. Using Cabrillo Tracker, an optical pattern recognition software, the 2-dimensional displacement of the spar was extracted from each frame for each camera. The cylinder experienced a pitch and roll motion about the mooring attachment point, and the measured displacements were the displacements of the lower end of the cylinder in the direction of the flow (the IL displacement) and perpendicular to the flow (the CF displacement). For select flow velocities, flow visualization tests were conducted. A neutrally buoyant fluorescent dye was injected directly upstream of the spar. Lighting banks and ultraviolet spotlights focused on the wake enabled the capture of video of both the near and far wakes from the perspective of the Phantom Miro M110 high-speed camera.

3.3 The natural frequency in otherwise still fluid

For the spar system placed in still fluid, a decay test was conducted to determine the system's natural frequencies in the inline (f_{IL}) and crossflow (f_{CF}) directions. In

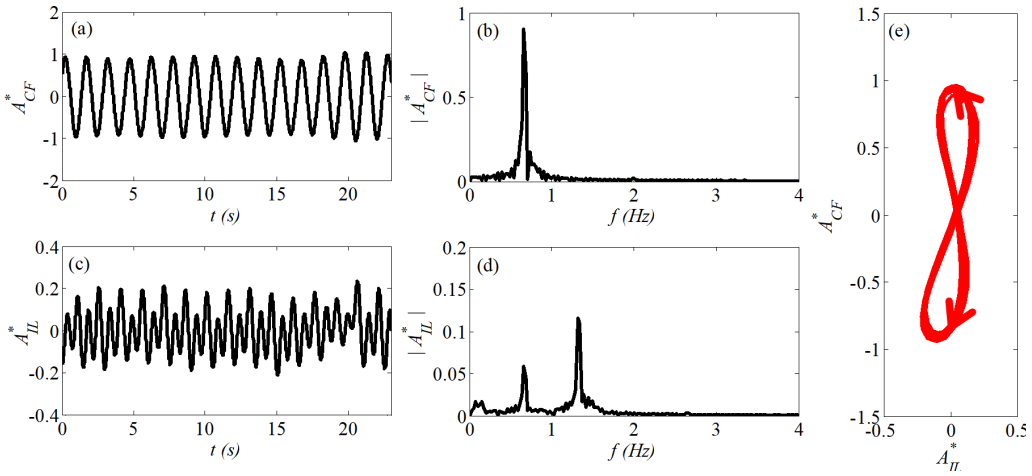

Figure 3.3. (A) Amplitude and (B) frequency of the crossflow response, together with the (C) amplitude and (D) frequency of the inline response, and (E) the corresponding orbital motion of the lower end of the bare cylinder at $U^* = 10.5$.

separate tests, the spar was given an initial disturbance mainly in each of the inline and crossflow orientations and time histories were recorded. The natural frequencies were measured from the corresponding fast Fourier transforms to be $f_{CF} = f_{IL} =$ 0.63 Hz, in the CF and IL directions. The damping ratio in still fluid during the decay tests, ζ, was found to be $\zeta = 0.067$ in both the CF and IL directions.

3.4 Amplitude and frequency of the response

The floating cylinder was placed in the test section of the water tunnel, and the flow velocity was increased from zero in small increments. At each flow velocity, the displacements were measured using the high-speed cameras. The cylinder started to oscillate in both the IL and CF directions after a reduced velocity of $U^* \approx 4$. The amplitude of oscillations increased with increasing flow velocity. Figure 3.3 demonstrates the response of the cylinder at a reduced velocity of $U^* = 10.5$ as a sample case. The amplitude of oscillations is nondimensionalized by dividing it by the diameter of the cylinder: $A^* = A/D$. At $U^* = 10.5$, the crossflow amplitude was $A^*_{CF} \approx$

1 (Figure 3.3(A)), and the inline amplitude was $A^*_{IL} \approx 0.35$ (Figure 3.3(B)). Despite a constant natural frequency in both directions at zero flow velocity, the dominant oscillation frequency in the CF and IL directions were $f_{CF} = 0.9$ Hz (Figure 3.3(B)) and $f_{CF} = 1.8$ Hz (Figure 3.3(D)), respectively, leading to a 2:1 ratio between the inline and crossflow oscillation frequencies and a figure-eight–type trajectory (Figure 3.3(E)). A smaller contribution of the first harmonic is observed in the IL frequency content. This is due to the asymmetry of the shedding pattern [37]. The vortices that are shed off the cylinder lead to fluctuating forces in the CF and IL directions, with frequencies equal and twice the shedding frequency, f_s, respectively. This will result in an excitation with a frequency of $2f_s$ in the IL direction and a frequency of f_s in the CF direction. The observed figure–eight trajectory is similar to what has already been observed in the VIV response of a 2 DOF circular cylinder [30][31].

If the flow is from left to right, a trajectory is called CCW when the cylinder moves in the CCW direction in the upper half of the figure–eight, and is called clockwise (CW) otherwise. In fact, a CCW trajectory corresponds to the case in which the cylinder moves in the opposite direction of the flow when it is at its extreme amplitudes in the crossflow direction. The observed trajectories in the sample case shown in Figure 2 are CCW trajectories. If we extend this analysis to all the other reduced velocities within the lock–in region, we observe that they all are CCW.

Figure 3.4 shows the cylinder's trajectory (the dimensionless CF oscillations plotted versus the dimensionless IL oscillations) for its lower end, versus U^* for the entire range of reduced velocities tested here. It is observed that the full domain is dominated by CCW trajectories (shown in red) of the lower portion of the cylinder, implying that once the oscillations start, they stay CCW for the entire lock–in region.

The corresponding CF and IL amplitudes of the response for the entire range of reduced velocities tested here are shown in Figure 3.5(A,B). The onset of the lock-in region is clear in both directions. In the CF direction, the amplitude of oscillations

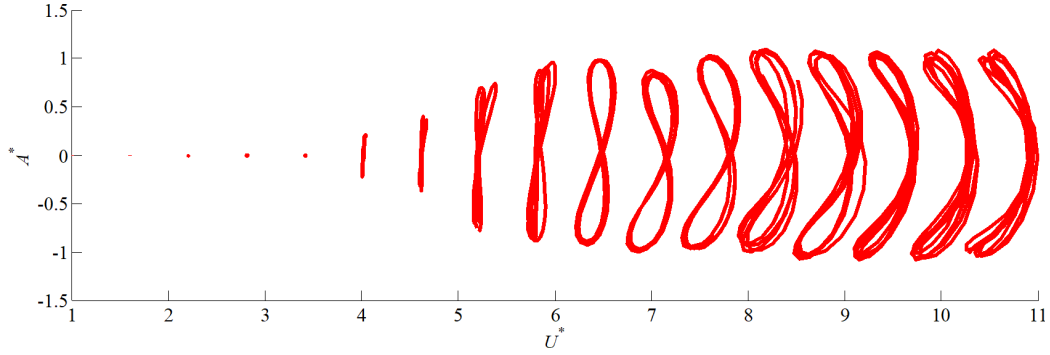

Figure 3.4. Dimensionless orbital trajectories of the cylinder's lower end versus reduced for the bare cylinder

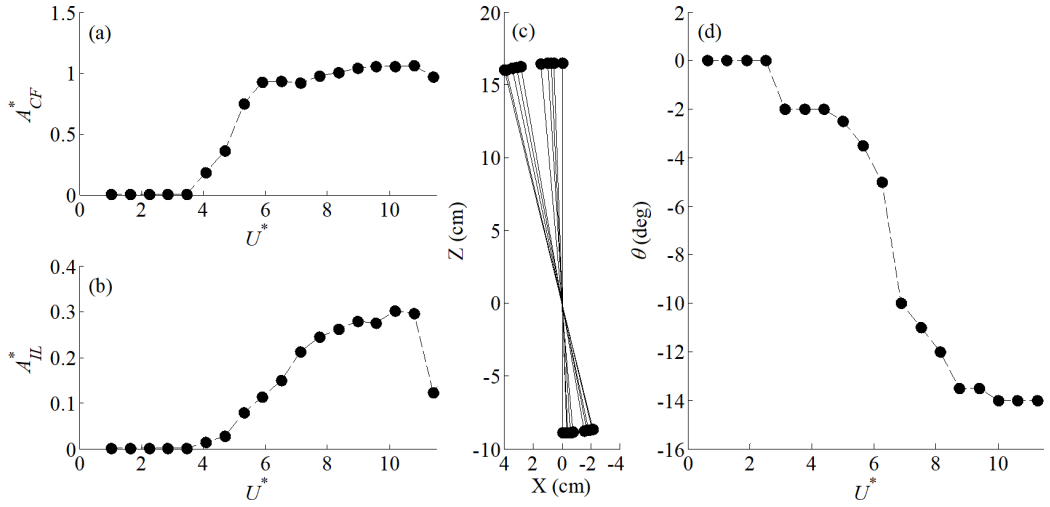

Figure 3.5. The amplitude of the (A) crossflow (CF) and (B) inline (IL) oscillations of the cylinder versus reduced velocity, (C) a side view of the static deflection of the cylinder as the flow velocity is increased, showing a node at Z = 0, and (D) the average static pitching angle for the bare case versus reduced velocity.

increases to $A^*_{CF} \approx 1$ and in the IL direction to $A^*_{IL} \approx 0.3$. The tests were stopped at reduced velocity of $U^* = 10.9$, because the cylinder's inclination was excessive. As the flow velocity was increased, the cylinder experienced a static inclination in the IL direction because of higher mean drag, as shown in Figure 3.5(C). The inclination angle, θ, is defined as the angle that the cylinder makes with a vertical line. This value was calculated based on the mean inclination angle recorded by the side-facing camera and is shown versus reduced velocity in Figure 3.5(D). This inclination angle increased with reduced velocity to a maximum of approximately $\theta = 15°$, which is the maximum static inclination tolerance for similar floating concepts [29] for the survivability limit during a 100-year storm response. Therefore, the tests were conducted up to the flow velocity at which this angle of inclination was observed.

3.5 Synchronization between the shedding and oscillation frequency

Within the lock–in region of any VIV response, the shedding frequency and the oscillation frequency are equal. Therefore, to show that the oscillations that are observed here are VIV, we should show that the oscillation frequency and the shedding frequency are synchronized. We conducted a series of flow visualization tests in order to observe the wake of the structure when it oscillates and measured the corresponding shedding frequency. Fluorescent dye was injected upstream the oscillating cylinder through a tiny dye tube and was exposed to ultraviolet light to visualize the wake. The capture area was focused on a portion of the cylinder near its lower end. Figure 5 shows a sample snapshot of the cylinder's wake at $U^* = 7$, where 2 cycles of vortex shedding can be observed: Vortices 1 and 2 are already shed and are in the wake, vortex 3 is just being shed, and vortex 4 is being formed as the shear layer bends inward. Similar pattern was observed for all the reduced velocities within the lock–in region.

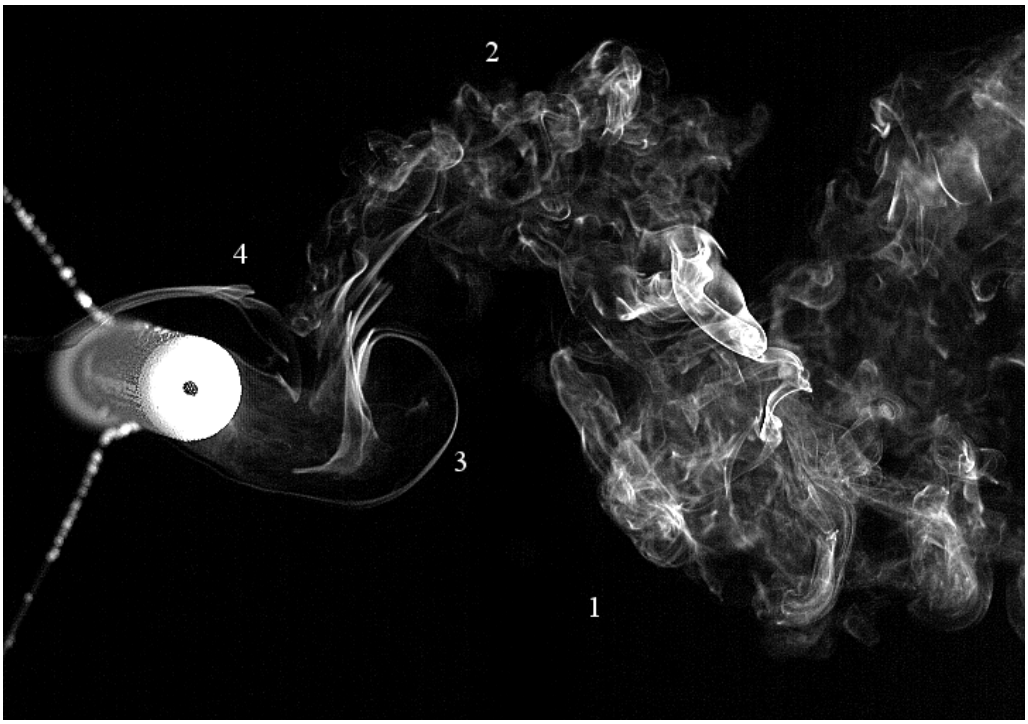

Figure 3.6. A sample snapshot of wake visualization to measure the shedding frequency at $U^* = 7$.

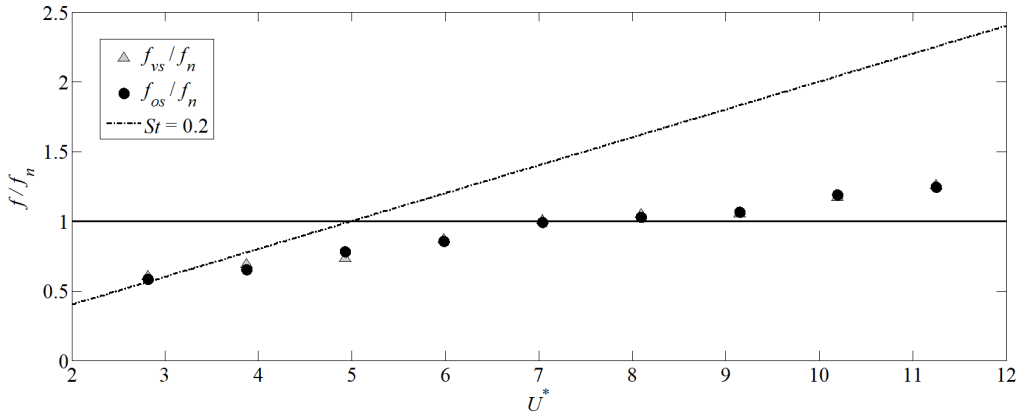

Figure 3.7. The normalized oscillation frequency versus reduced velocity. The dashed–dotted line corresponds to the predicted Strouhal frequency (based on $St = 0.2$) for a fixed cylinder.

Figure 3.7 shows the normalized shedding frequency and the normalized oscillation frequency in the CF direction versus the reduced velocity. The oscillation frequency is found using the measured time histories of the displacement, and the shedding frequency is measured using flow visualization tests by visually quantifying the number of vortices that are shed in our flow visualization videos. This method has been extensively used to measure the shedding frequency at low flow velocities. Lienhard and Liu [67] found an error of approximately 3% for frequencies calculated using this method. The plot shows that the shedding frequencies stay close to the oscillation frequencies at each reduced velocity indicating that the 2 frequencies are synchronized and therefore VIV is observed. The line in the figure corresponds to the estimated Strouhal frequency, which is the expected shedding frequency off a fixed circular cylinder with the same diameter. As expected for a VIV response, the oscillation and shedding frequencies deviate from the predicted Strouhal frequency and stay around unity for the entire lock–in region.

3.6 CCW trajectory and the excitation region

The CCW trajectories of Figure 3.4 are for oscillations of the lower end of the cylinder. Since a node exists at the location where the cylinder is attached to the mooring lines (Figure 3.5(C)), when the oscillations are CCW in the lower part of this node, then they are CW in the upper part. This indicates that the cylinder experiences CCW orbits in its lower part and CW orbits in its upper part, for the entire lock–in region. This is a unique case for a flexibly–mounted rigid structure undergoing VIV, in the sense that at the same time, the structure is undergoing both CW and CCW orbital motions. In previous studies of VIV of 2 DOF systems, the structure could oscillate in a purely translational direction, and no node could have been observed anywhere along the length of the structure. Only in the VIV response of a flexible structure (e.g., a flexible cylinder placed in flow to model the VIV response of ocean risers) distributions of CW and CCW orbital motions are observed along the length of the structure[73][22]. In the current experiment, given that there is a node in the response of the moored cylinder, the regions for CCW and CW trajectories are clearly distinguishable: The lower part of the cylinder follows a CCW orbital motion and the upper part of it a CW orbital motion. Here, we investigate the significance of observing a CCW or a CW trajectory in this system.

Bourguet et al. [22] used a series of experimental results as well as detailed direct numerical simulations numerical results to show that for a flexible cylinder undergoing VIV, the trajectories are CCW in regions of the cylinder's length where the flow is exciting the cylinder. Toward this goal, they pinpointed the regions of the cylinder where the power was transferred from the fluid to the structure using their numerical results and then observed that the trajectories are CCW in those regions. They showed that in other parts of the cylinder where energy was being damped, the trajectory could be CW or CCW.

We hypothesize that in the case of a moored cylinder placed in flow, if the region of the cylinder with a CCW orbital motion is the region in which the flow has excited the cylinder, then by suppressing VIV only in that region, the resulting amplitude of oscillations will decrease dramatically. If, however, we suppress VIV in the region with CW orbital motion, since this region does not act as an excitation region, then the amplitude of the resulting VIV response will not change much. To test this hypothesis, we suppress VIV in the region of interest and then measure the cylinder's response and compare it with the VIV response of a bare cylinder.

3.7 VIV suppression via strakes

Helical strakes are known to suppress VIV ([39],[110],[116]) and the present study used them in our experiments as well. Helical strakes were chosen to suppress VIV, only because they have been used extensively for VIV suppression. Any other VIV suppression method could have been used to test the hypothesis. For the present study, we used a helical strake of height and pitch of 0.25 diameters and 17 diameters, respectively, following Constantinides and Oakley [28]. The components for each buoy configuration were built using the same 3D printing technique as the bare cylinder, with the strake–hull assembly printed simultaneously as a solid body. The additional weight and damping of the strakes resulted in a lower natural frequency of $f_n = 0.29$ Hz in both the CF and IL directions for the straked cylinder variations, including the fully straked cylinder. The damping ratio in still fluid during the decay tests was found to be $\zeta = 0.2$ for all the straked cylinder variations (compared with $\zeta = 0.067$ for the bare cylinder). As a first step, to examine that the strakes were designed properly, we tested whether the strakes could reduce the magnitude of the VIV response efficiently or not, by covering the entire length of the cylinder by strakes and measuring the resulting response. In that case, the amplitude of the response was reduced to $A^* \approx 0.01$ in both directions, which is by far smaller than what was

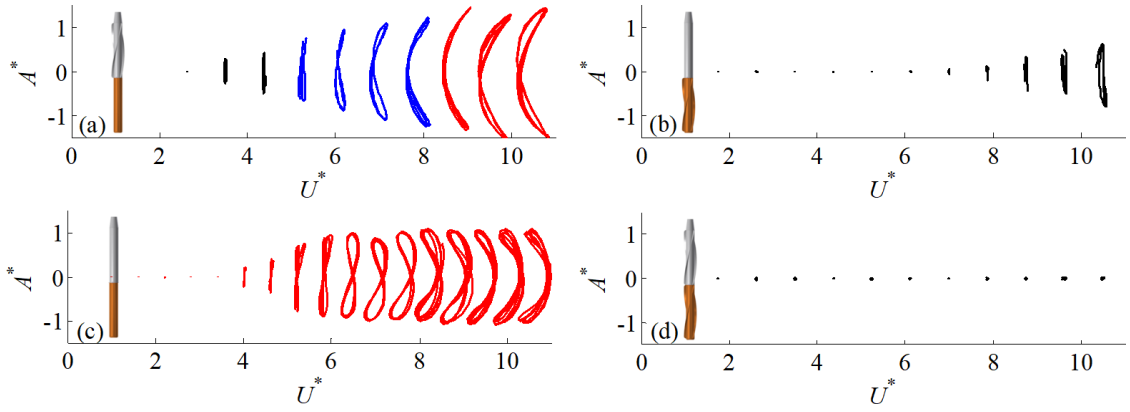

Figure 3.8. Orbital trajectories versus reduced velocity for the (A) upper–straked cylinder, (B) lower–straked cylinder, (C) bare cylinder, and (D) fully straked cylinder.

observed in Figure 3.4 for a bare cylinder. We had observed crossflow amplitude of around A^*_{CF} ≈1 and the inline amplitudes of around A^*_{IL} ≈0.35 for the bare cylinder, and clearly covering the entire cylinder by strakes reduces the amplitude dramatically and suppresses VIV. Therefore, we conclude that the strakes are designed properly.

3.8 Suppressing VIV in the portions with CW and CCW orbital motions

After showing that the strake design was appropriate, we conducted 2 series of experiments to test the hypothesis discussed in Section 3.6. First, we covered the upper part of the cylinder by strakes, which if our hypothesis is correct, should not reduce the amplitude of the response because flow does not excite the cylinder in that region. Then we covered the lower part of the cylinder by strakes, which if our hypothesis is correct, should reduce the observed VIV response, because flow does excite the cylinder in that region. In both cases, "upper–straked" and "lower–straked" configurations, the natural frequencies were measured and found to be equal to 0.29 Hz in both directions at zero flow velocity.

Figure 3.8(A) shows the orbital motion of the cylinder when its upper part was straked. It is observed that the general behavior is very much similar to the bare cylinder. Large–amplitude responses still exist in both the IL and CF directions, and the lock–in region is observed for a range of U^* ≈6–10.5, suggesting that VIV is not suppressed. The figure–eight trajectories are observed to be in both the CW and CCW directions, but the oscillations do exist and their amplitudes and frequencies in both the IL and CF directions are comparable with those of the bare cylinder.

When the strakes are placed along the lower portion of the cylinder, however, the VIV response is mainly suppressed as observed in Figure 3.8(B). There are some small nonzero amplitudes of oscillations for U^* >9.5, but they are very small compared with the amplitudes of oscillations observed in the bare cylinder case.

For the ease of comparison, the responses of the bare and fully straked cylinders are plotted in Figure 3.8(C,D). Overall, the response of the upper–straked cylinder over the entire range of reduced velocities resembles that of the bare cylinder, and the response of the lower–straked cylinder resembles that of a fully strake cylinder. The fact that VIV was suppressed significantly by placing strakes along its lower portion confirms our hypothesis: The flow forces do excite the lower portion of the cylinder, within which CCW orbital motions are observed.

3.9 Conclusions

Vortex–induced vibration of a floating cylinder, resembling a spar buoy platform for floating offshore wind turbines, was studied experimentally. The cylinder was moored about its center of mass in the test section of a recirculating water tunnel, allowing fully 3–dimensional oscillations. The cylinder was observed to oscillate in the CF and IL directions over a range of flow velocities. The oscillation frequency in the CF direction was equal to the shedding frequency and in the IL direction was twice the shedding frequency, which resulted in a figure–eight-–type trajectory.

The trajectories were CCW in the lower end of the cylinder and CW in its upper end. It was hypothesized that the region with a CCW orbital motion is the region within which the cylinder is excited by the flow. This hypothesis was validated by suppressing VIV after placing helical strakes in the region with CCW orbital motion, while placing strakes in the region with CW orbital motion did not suppress the oscillations. This finding is of significance both from a fundamental point of view in showing that the region of a cylinder undergoing VIV in which the flow excites the cylinder follows a CCW orbital motion and from an applied point of view to give guidance for strategies to suppress or reduce the VIV response of future floating offshore turbine platforms.

It is expected that changing the location of mooring attachment point or the center of mass would change the exact location of the node and therefore the range of the observed CCW and CW motions. But it is expected that these changes would be only minor as long as the general design concept of the spar stays the same. In an extreme case, if the location of the mooring attachment point is moved to one end of the cylinder, then the system would become a pendulum–like cylinder. Jauvtis and Williamson [59] studied 2D VIV of a pendulum–like cylinder and reported the phase angles between the IL and CF oscillations. According to their results, the oscillations are in the CCW direction for almost the entire lock–in region, except for a very small region with small amplitudes of oscillations. The CCW orbits have also been observed in the lock-in region of purely translational 2D flexibly–mounted cylinders [31] It is the existence of a node in the middle of the cylinder in the case studied here that leads to a combined CCW and CW orbital motions in the same rigid body. If this node did not exist, then the entire cylinder would oscillate in a CCW direction within the lock–in region.

CHAPTER 4

2D VIV FOR A CURVED CYLINDER

In this chapter, rigid curved cylinders with crossflow and inline degrees of freedom are tested for the influence of concave versus convex curvature on the response to vortex-induced vibrations.

4.1 Introduction

For applications such as mooring cables for offshore purposes, the structure has both multiple degrees of freedoms and a non-uniform cross-section. The fatigue life of these kilometers-scale cables can be better known by studying how their curvature interacts with vortex shedding and responds to flow-induced oscillations. Vortex-induced vibration is a fundamental mechanism of flow-induced oscillations and has been thoroughly studied for rigid uniform cylinders with crossflow freedom ([13], [86], [113]). By breaking the symmetry of the cylinder more complicated flow-induced oscillations may occur either instead of or in conjunction with vortex-induced vibrations. Some example of cylinders with broken symmetry include those with axial tapering, curvature, or a faceted face with some angle of attack ([11], [35], [90], [89]). Curved cylinders in particular present a system whereby the continuously variable inclination leads to a breakdown of the small angle assumptions key to the Independence Principle ([99], [121]), creating a response sensitive to the concavity of the cylinder.

Miliou et al. [69] provided the first numerical analysis of the complex vortex shedding patterns surrounding a curved cylinder, as theorized in the experimental work of

Takamoto & Izumi [102]. This was expanded to oscillating cylinders with an extended axial tip by de Vecchi et al. [35], which saw highly three-dimensional flow instigated by the cylinder's concavity, with vortex separation correlating along the length of the cylinder as opposed to the fixed case [34] for which vortex shedding showed no sensitivity to the curvature. They also numerically proved that by reducing the damping at the axial tip of the cylinder, the flow would excite the structure. This finding was experimentally supported by Assi et al. [11], which observed reduced oscillation amplitudes when the axial tip encountered the flow first (in the concave orientation), meaning the extended tip was acting as a hydrodynamic damper as it disturbed the flow ahead of the rest of the cylinder. Seyed-Aghazadeh et al. [90] eliminated the additional tip damping by excluding the extended axial tip, testing just the quarter-circle section free to oscillate in crossflow. Here they observed the manifestation of higher harmonic forces for a curved cylinder, a phenomenon not seen for the previous, higher damping cases. Furthermore, the higher harmonic forces were shown to manifest at different U^* depending on the concavity of the cylinder. While the convex orientation responded with a larger peak oscillation amplitude at the velocity range for which higher harmonics were recorded, the concave case responded with generally smaller crossflow amplitudes but sustained a 3f harmonic for significantly higher velocities. By sustaining the higher harmonic beyond the traditional lock–in range, an extended lower branch resulted. Flow visualization confirmed the findings of de Vecchi et al. [34] and Assi et al. [11], in that vortex shedding from the axial tip disturbs the flow downstream, creating a break in vortex shedding correlating near the midpoint of the cylinder for the concave orientation, while the correlation length is significantly higher for the convex orientation whereby the wake of the axial tip is downstream of the rest of the cylinder.

For structures with multiple degrees of freedom, the core difference to single-degree systems is the possibility of dual resonance [32], leading to stronger fluid forces

which would otherwise be suppressed if the structure is constrained to a single degree of freedom. As current literature has only studied these curved cylinders for one-dimensional oscillations, the present work continues that of Seyed-Aghazadeh et al. [90] but for a system flexibly mounted with crossflow and inline degrees of freedom, such that the system has constraints more similar to those encountered by actual catenary moorings.

In the present work a curved cylinder is tested experimentally in flow for convex and concave orientations, on an apparatus which permits crossflow and inline degrees of freedom. Cylinders with different CF-IL natural frequency ratios are examined for VIV and other forms of flow–induced oscillation, and the role of higher harmonic forces on the amplitude response is discussed. The role of the axial tip is examined, and compared to the same cylinder undergoing VIV with only crossflow freedom.

4.2 Validation of a low–coupling apparatus to study 2D VIV

4.2.1 Experimental methods

The mounting apparatus was constructed using air bearings resting on a smooth glass surface. Four air bearings support an aluminum truss from which arbitrary cylinders can be mounted (Figure 4.1), penetrating the free surface into the test section. A matte white L-plate was mounted such that each leg is perpendicular to either CF or IL, and serves as a reflection surface for the non-contacting laser displacement sensors. The rig was validated via VIV tests for a uniform acrylic cylinder 25.4 mm in diameter and 300 mm in length, with variable external masses applied to consider a range of mass ratios (mass ratio $m^* = \frac{m}{\rho V}$, where m is the moving mass, ρ the displaced fluid density, and V the displaced fluid volume). The cylinder was mounted on the low-friction air bearings free to move within the 2D inline-crossflow plane. The displacement of the structure was measured via non-contacting laser displacement sensors, which were mounted in the crossflow and inline directions.

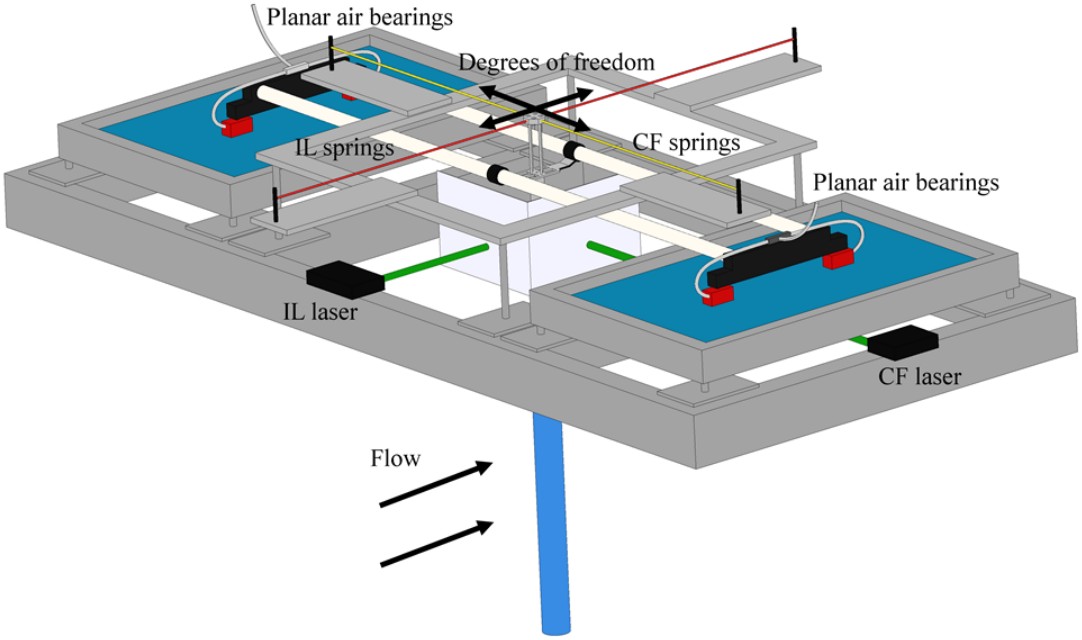

Figure 4.1. The two-dimensional oscillation apparatus, with low-damping air bearings and stiffness provided by opposing springs. Laser mockups used for noting displacement sensor placements.

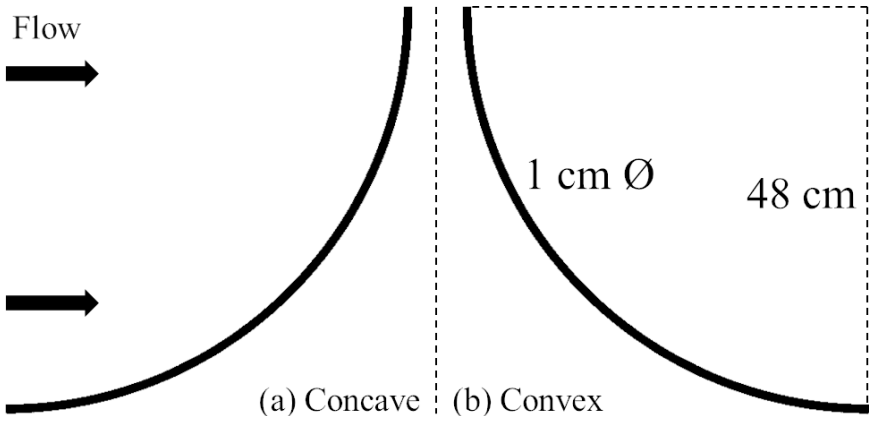

Figure 4.2. Dimensions and directionality of the curved cylinder relative to flow.

Structural stiffness was provided by pairs of opposing springs fixed in the inline and crossflow orientations. Monofilament wire was used to extend the length of these springs to 254 mm in order to reduce the angular displacement about the springs as the structure oscillated, minimizing structural coupling between the crossflow and inline components. Decay tests were conducted, and showed a maximum of 1.04% coupling in the spectral FFT contributions between the two perpendicular directions. Given an impulse 45 degrees between the inline and crossflow components, the ζ damping ratio in air was found to be less than ζ <0.5% in CF and ζ <0.3% in IL. The air bearing apparatus was mounted over a recirculating water tunnel with a test section of 1.27 m $\times$ 0.5 m $\times$ 0.38 m, which can produce a flow up to 1 m/s with turbulence intensities less than 1%.

4.2.2 VIV of a uniform cylinder

To validate the low–coupling mounting apparatus, the VIV response of a uniform cylinder with crossflow–inline freedome was examined. A suitable velocity range was determined by finding the maximum and minimum velocities for which oscillations occured. This range was nondimensionalized as the reduced velocity U^* ($U^* = \frac{U}{f_n D}$, where U is the flow velocity, D is the cylinder's diameter, and f_n the structure's natural frequency in still water) ranging from U^* =2–12, and corresponds to Re =725–5000. The natural frequency f_n was found in still fluid, using decay tests from a 5 cm initial displacement to calculate the FFT, yielding a natural frequency of f_{ncf} =0.6 Hz and f_{nil} =1.2 Hz, or a structural stiffness ratio of 2. At each velocity increment, after being allowed to reach steady-state the 2D crossflow-inline oscillation response was recorded for 90 seconds. In Figure 4.3 the dimensionless amplitude ($A^* = A/D$) response of a uniform cylinder at each U^* is presented for varying mass ratios. In agreement with Williamson & Jauvtis [59], compared to a 1D crossflow response the oscillations due to 2D VIV occur with a greater amplitude and wider lock–in region

([30], [31]). Furthermore, the influence of an additional inline component is magnified at lower mass ratios (Figure 4.4).

Due to symmetry, the inline force acts at twice that of crossflow, giving a 2D figure–eight pattern to the response. These figure–eights have a consistent directionality to them depending on whether the cylinder moves with or against the flow at the peaks of the figure–eight. Thus using the same nomenclature as Dahl et al. [30] given left–right flow when viewing an orbit with the crossflow direction on the vertical axis, the upper loop would have a counter-clockwise direction (CCW, colored red in the present work) when the cylinder oscillates into the flow at the peak. If the cylinder were to oscillate with the flow, it would be called a clockwise oscillation per the direction of the upper loop. For the response of the uniform cylinder, after the onset of oscillation all orbits responded with CCW directionality. There have been some numerical and experimental studies which have shown that for a cylinder allowed to move with simulataneous clockwise and counterclockwise regions along its length, clockwise orbits may indicate regions of the structure either being excited or damped by the flow, but counterclockwise orbits always accompany excitement of the structure by the flow ([22], [73], [27]).

By adding external masses, the mass ratio of the system ($m^* = \frac{m}{\rho V}$) was increased from 4.65 through 22.6 for the same U^* measurements. Here it was observed that even for the most massive cylinder tested the figure-eight trajectory does not completely collapse (in agreement with literature [59]), but rather it decreases the IL:CF ratio of the oscillations as well as the width of the lock-in range (Figure 4.4).

Considering the low m^* case, the response was collapsed against V_rSt (V_r the true reduced velocity uses f_{os} instead of f_n as in U^*) in order to compare the amplitude response to the two local peaks were observed in the crossflow amplitude response (Figure 4.6). These peaks, previously reported in Sarpkaya (1995)[85] and Dahl et al. (2006)[30], were found to be caused by triplet vortex shedding by Williamson &

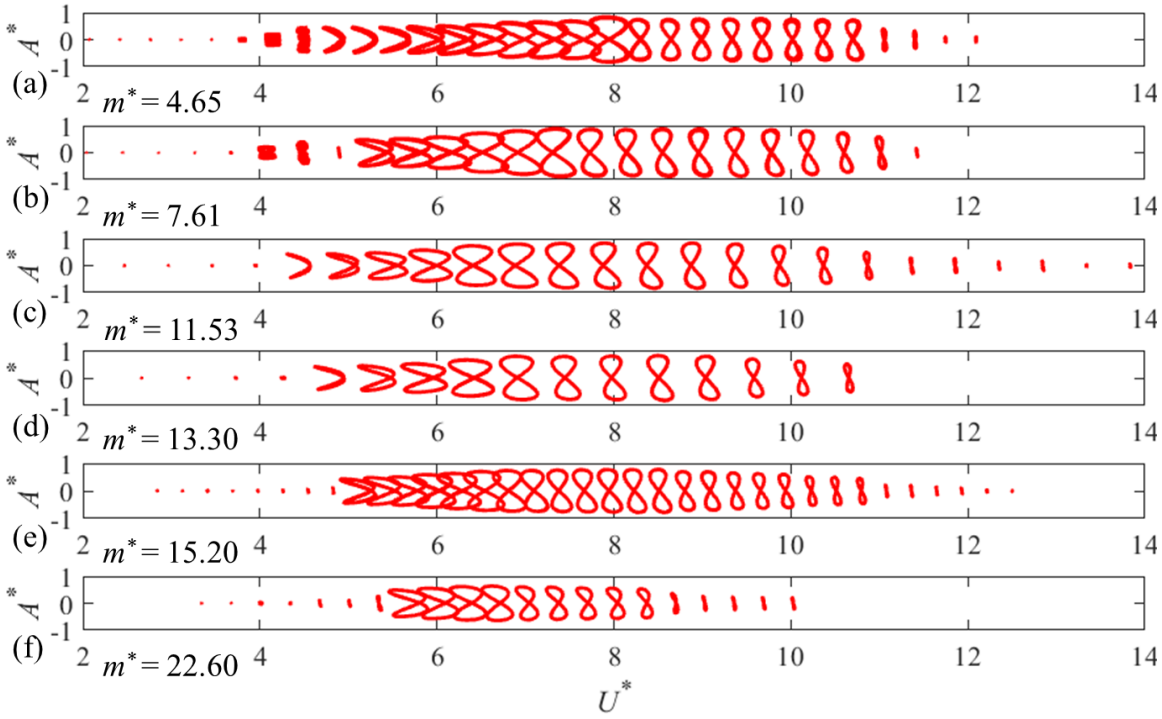

Figure 4.3. Two-dimensional orbits of a uniform cylinder undergoing VIV for varying mass ratios. Trajectories are to-scale and all orbits were observed to have counterclockwise directionality (colored red).

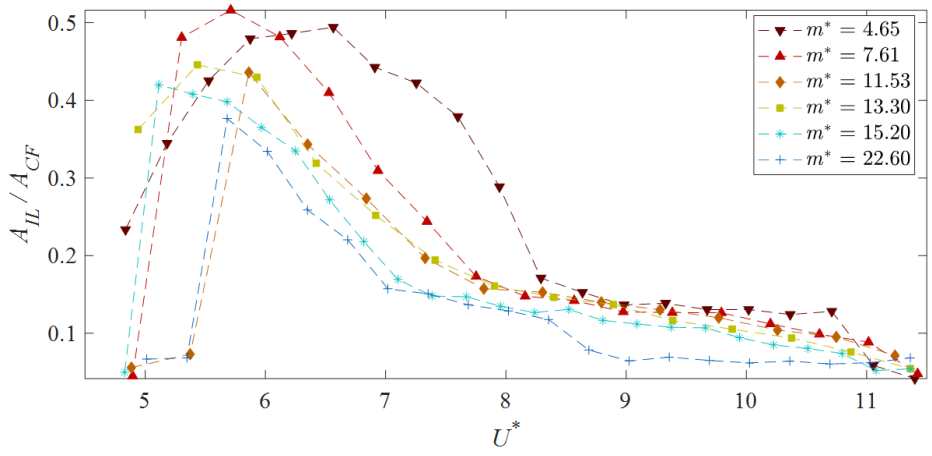

Figure 4.4. Uniform cylinder response, reduced to figure-eight amplitude ratio.

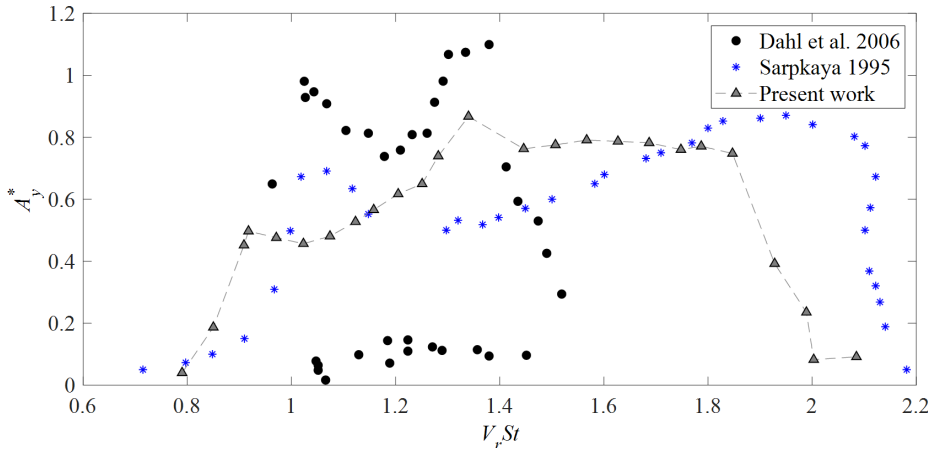

Figure 4.5. Low m^* response from the present work (Frequency ratio 2, $m^*\zeta = 0.023$) compared to Dahl et al. [30] (Frequency ratio 1.9, $m^*\zeta = 0.35$) and Sarpkaya [85] (Frequency ratio 2, $m^*\zeta$ not reported but calculated to be approximately 0.01-0.04).

Jauvtis (2004)[114]. In particular, for very low m^* (m^* <6) systems, the 2D movement permits what they branded as a "super upper-branch", with $A^* = 1.5$.

By collapsing the low m^* case by the V_rSt parameter (V_r the true reduced velocity uses f_{os} instead of f_n as in U^*) the amplitude response can be compared to 2D VIV response data reported by Dahl et al. (2006) [30] (with f_{nIL}/f_{nCF} =1.9) and Sarpkaya (1995)[85] (with f_{nIL}/f_{nCF} =2.0). In figure 4.5 the three cases are overlaid. Note however that both mass and damping are different between the cases. The data from Dahl et al. had $\zeta = 6.2\%$ and $m^* = 5.7$, yielding $m^*\zeta = 0.35$. The present work had a system with $\zeta = 0.5\%$ and $m^* = 4.65$, yielding $m^*\zeta = 0.023$. Sarpkaya did not report $m^*\zeta$ values, but did provide results in terms of the Skop-Griffin parameter ($S_G = 2\pi St^2\delta_r$, $\delta_r = 2m(2\pi\zeta)/\rho D^2$, additional details in [87] and [88]) by which $m^*\zeta$ may be esimated. By estimating $St = 0.2$, $m^*\zeta$ falls on the range of 0.01 to 0.04 (the study used multiple cylinders with different diameters). Generally each case is seen to have two local peaks in the amplitude response, with the maximum amplitude in the present work at a similar value to that of Sarpkaya [85] but at a V_rSt closer to that of Dahl et al. [30]. This is likely further complicated by a wide range of Reynolds

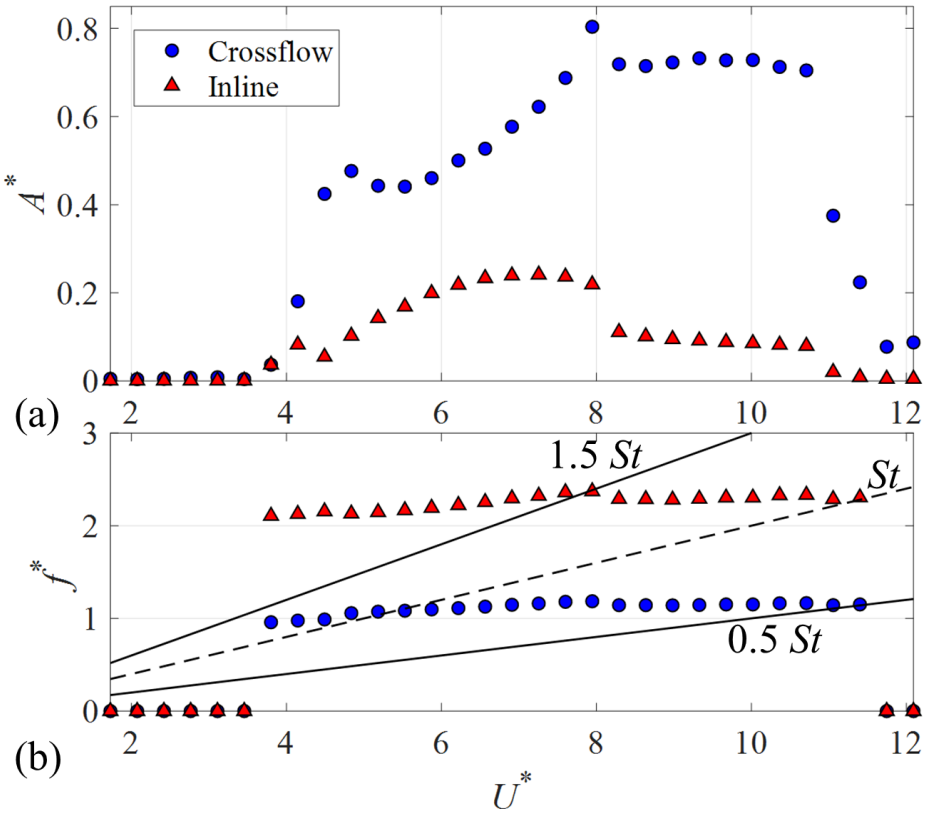

Figure 4.6. Components and oscillation frequencies of the low m* uniform cylinder case.

numbers between the cases: 725–5,000 for the present work, 11,000-44,000 for Dahl et al., and a maximum of 35,000 for Sarpkaya. Nonetheless, qualitatively the same general trends are observed in all the cases.

By comparing the crossflow amplitude of the present work to the oscillation frequency (Figure 4.6), it is observed that the lower velocity amplitude peak near $U^* = 5$ occurs as the crossflow oscillation frequency f_{osCF} meets the vortex shedding frequency predicted by the Strouhal trend. Meanwhile the higher velocity amplitude peak at $U^* = 8$ coincides with the inline oscillation frequency f_{osIL} passing an odd-integer multiple of the shedding frequency of $1.5St$.

Table 4.1. Properties of the curved cylinder.

R/D	$m^*\zeta$	m^*	U^*	Re
47.5	0.034	8.6	4-14	725–5000

4.3 FIO of a curved cylinder with crossflow–inline freedom

4.3.1 Relevance to prior studies

For a curved cylinder in flow, there exists two principal orientations: concave, with the horizontal tip facing upstream into the flow, and convex, with the tip facing downstream with the flow. Thus, the flow encounters the axially-aligned tip first in the concave orientation, and encounters the perpendicular cylinder first in the convex orientation. To compare two-dimensional oscillations to a one-dimensional crossflow case, the same cylinder used by Seyed-Aghazadeh et al. [90] is again used here. The cylinder was flexibly-mounted in two-dimensions using the planar air bearing setup previously discussed, with the oscillations recorded via the same non-contacting displacement sensors. The cylinder was tested for $U^* = 4$–11, encompassing the entire lock-in range, for both convex and concave orientations. Using the same decay test methodology as with the uniform cylinder validations cases, FFT calculations yielded a natural frequency of $f_{nCF} = 0.70$ Hz and $f_{nIL} = 1.41$ Hz, or a structural stiffness ratio f_{nIL}/f_{nCF} of 2.01. The damping ratios in air were found to average as follows: ζ_{CF} =0.4% and ζ_{IL} =0.25%. Due to the mass of the rig, the mass ratio for the curved cylinder was higher than that of Seyed-Aghazadeh et al. [90], which had $m^* = 4.5$. For the same cylinder, the present work had $m^* = 8.6$. For comparison, the uniform cylinder with $m^* = 7.6$ shown in Figure 4.3 was chosen.

Previous studies ([11], [35]) have observed elongated vortex-induced vibration lock-in ranges for curved cylinders in the concave orientation, but at a reduced ampltiude compared to the convex orientation. They concluded that the cylinder tip acts as a hydrodynamic damper, whereby shedding vortices from the tip disrupts

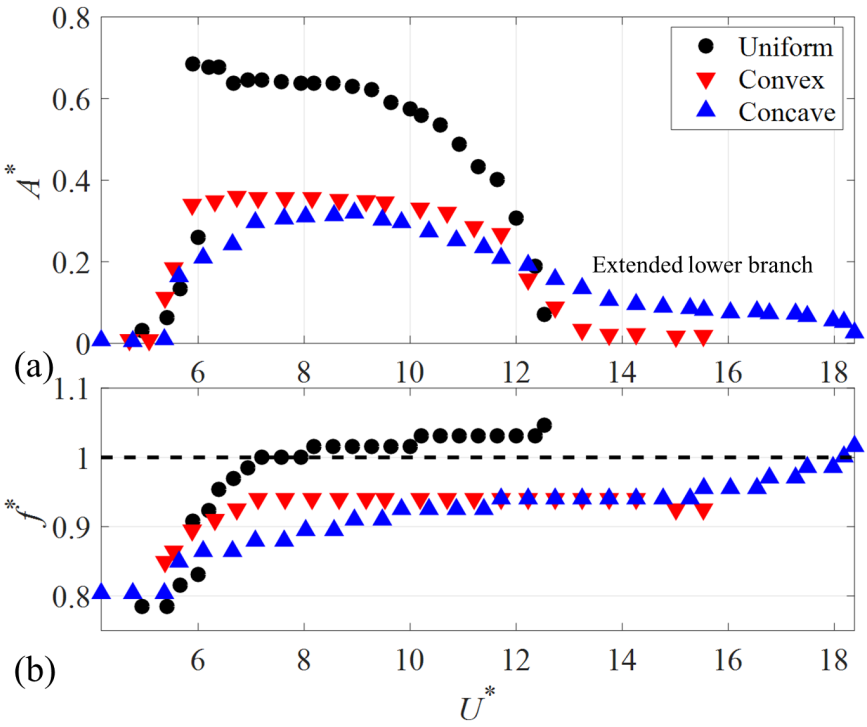

Figure 4.7. Referenced 1D data set from Seyed-Aghazadeh et al., figure reproduced from [90].

synchronization along the curvature of the downstream portion of the cylinder. Seyed-Aghazadeh et al. [90] observed that the extended lower branch for the concave case coincides with the occurrence of higher harmonic forces, and do not manifest for the convex orientation which due to this lack has a reduced lock-in range width. Near the maximum amplitude response, the convex case has stronger contributions from higher harmonic forces than the concave case, and responds with higher crossflow amplitudes as well.

4.3.2 The general amplitude response

At each U^* increment the response was allowed to reach steady–state before oscillations were recorded, and this process was repeated for both the concave and convex orientation In Figure 4.8, the oscillation orbits are plotted to-scale: (a) being concave, and (b) convex. Note that all orbits were observed to have counterclockwise directionality (the cylinder rotates into the flow at the peaks of the orbit). Plotted to-scale this is not immediately evident, due to the inline component being mostly suppressed for the concave cylinder. As well, the crossflow amplitude is reduced for the concave cylinder for all U^* compared to the convex cylinder. To examine this change, each amplitude component is separated and plotted in Figure 4.9. Note that the extended lock-in branch reported in Seyed-Aghazadeh et al. [90] for the 1D concave case is again observed in Figure 4.9 for our two-dimensional response, but with significantly less distinction. The concave cylinder crossflow amplitude crosses above the convex case amplitude at $U^* = 12$ (Figure 4.9 (a)), after which a relatively constant amplitude response was observed. Considering the inline oscillation amplitude, the response is sufficiently suppressed for the concave cylinder that the extended lower branch is shown to have little if any influence.

As previously mentioned, despite a significant change in amplitude between cylinder concavities, the orbits were still consistently figure–eight and always responded

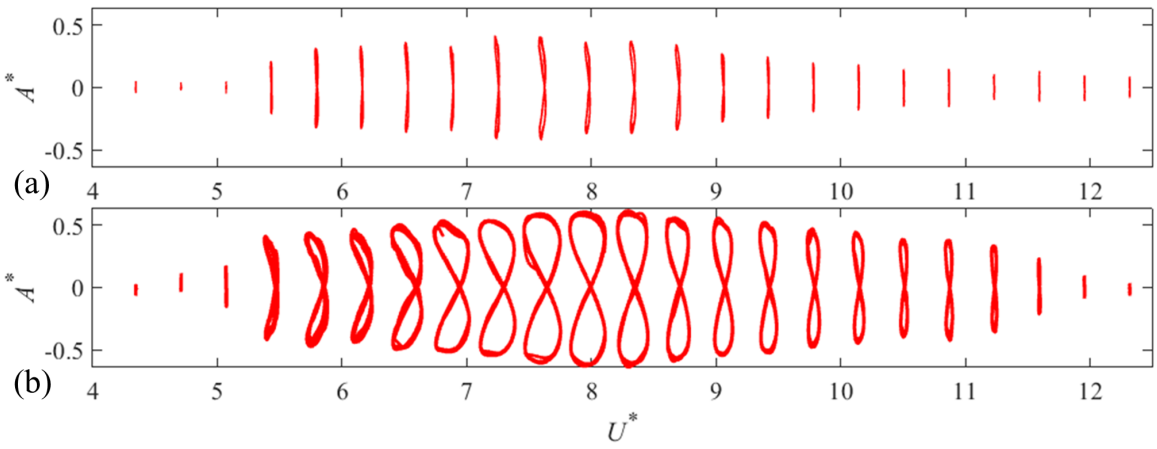

Figure 4.8. Oscillation orbits of the curved cylinder for the (a) concave and (b) convex orientations for increasing U^*.

with a counterclockwise displacement phasing: the mode of oscillation was unchanged. Therefore it would be anticipated that the frequency of oscillation would follow similar trends between the two cases. Thus the frequency response is plotted in Figure 4.10(a). For simplicity, the frequency of crossflow oscillation will be refered to as f_{osCV} for the convex orientation, and f_{osCA} for concave. The oscillation frequency of the uniform cylinder passes the natural frequency in air at approximately $U^* = 6.5$, which in the literature points to a distinct phase jump between the lift force and velocity for traditional 1D VIV [113]. To confirm this, the lift–velocity phase angle ϕ was calculated and used to find the lift coefficient in-phase with velocity, C_{Lv}

$$C_{Lv} = \frac{F_L sin(\phi)}{0.5\rho DLU^2} \tag{4.1}$$

where F_L is the lift force, ρ the fluid density, L and D the cylinder length and diameter, and U the fluid velocity. One can see that removing $\sin(\phi)$ yields the traditional lift coefficient. The uniform cylinder responded with a 90° crossover in Figure 4.10(b) when f_{os} surpasses f_{na} near $U^* = 6.5$. No curved cylinder case reported as clear a transition in the oscillation frequency nor the lift–velocity phase angle. Both

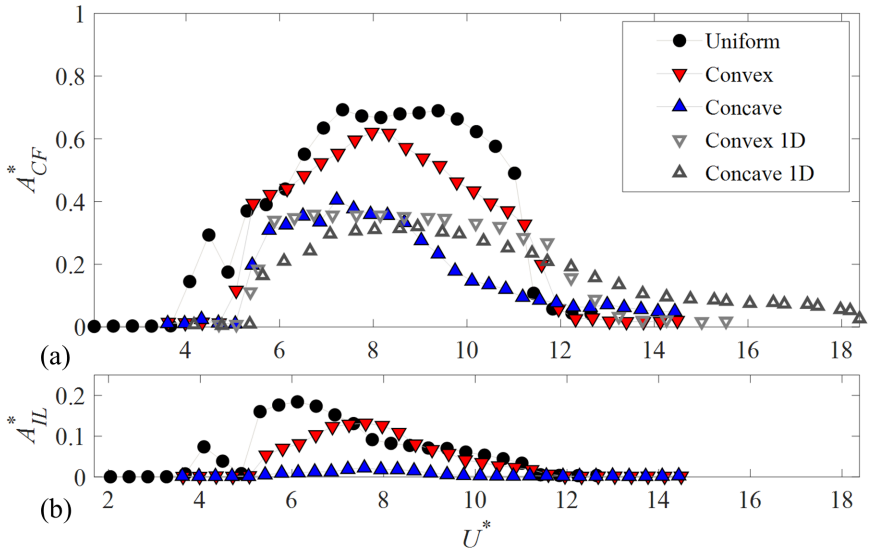

Figure 4.9. Amplitude components for increasing U^*.

the convex and concave curved cylinder oscillated at a frequency close to but below that of f_{air} for all U^* below 11.5, with almost identical trends between the convex and concave orientation. However, note the crossover between the convex and concave crossflow oscillation amplitude which aligns with the start of the concave's extended lower branch. This point occurs at the same U^* as the when f_{osCA} passes f_{na}, the natural frequency in air. For higher U^* f_{osCA} remains above f_{na}, while the oscillation amplitude for the convex cylinder is negligible, leading to f_{osCV} jumping above and below f_{na}.

4.3.3 Force reconstruction

Traditionally, the forces acting on a 1D system can be measured via a force sensor attaching the cylinder to a flexible mounting, with the sensor cabling routed to not affect the linearity of the system's stiffness. For the present work, however it was found that any cabling arrangement added nonlinear structural coupling as the cylinder oscillated about the crossflow-inline plane. Thus it was decided to use force reconstruction, previously used by Seyed-Aghazadeh et al. [90] to be found in agree-

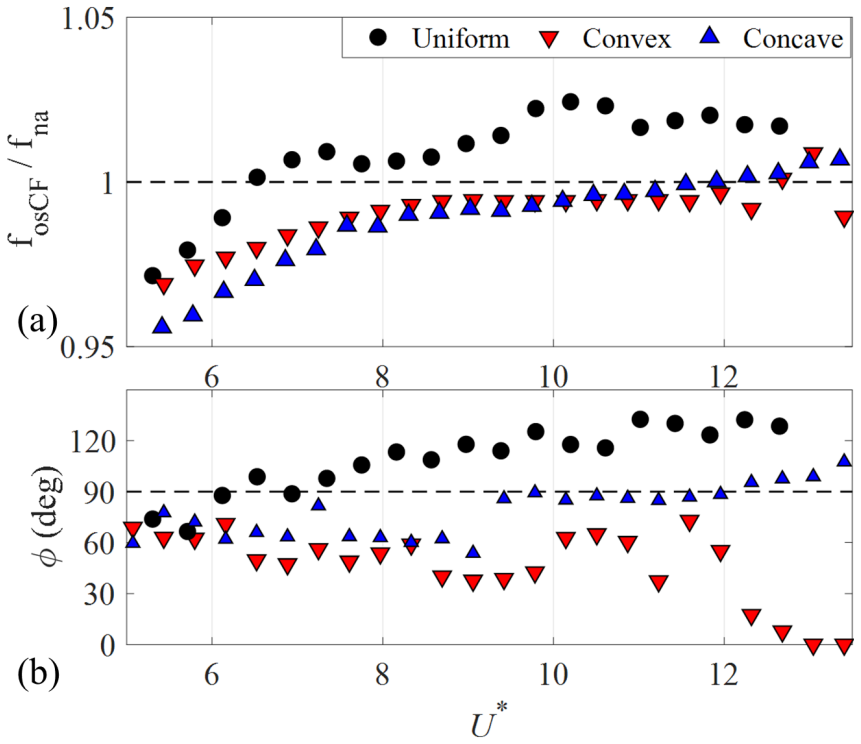

Figure 4.10. (a) Frequency ratio between the crossflow oscillation frequency and the natural frequency in air for the uniform and curved cylinders. (b) ϕ phase angle between lift and velocity.

ment with results of Khalak and Williamson [65]. Between the inline and crossflow directions, the coupling was observed to be at maximum 1.04% (contribution of the opposing component compared to the measured direction, in the spectral domain). The reconstruction process is to feed structural parameters and oscillation time series into

$$F/m = \ddot{y} + 2\zeta\omega_n\dot{y} + \omega_n^2 y \tag{4.2}$$

where F is the lift force, m the moving mass, y the oscillation time series, ζ the damping ratio in air and ω_n the natural frequency in air. Forces were reconstructed for the curved cylinder at sample U^* of 8 and 13 for both convex and concave orientations. Shown in Figure 4.11 are samples of the frequency contents of the lift coefficient time series. At $U^* = 8$, the lift force on the convex cylinder receives a significant 2f contribution likely from a component of drag acting in the lift direction, but the influence of the 2f peak was reduced for the concave orientation, pointing to a damping mechanism. At a higher U^* at 13, the extended lower branch can be examined. In this region, the response of the concave system is dominated by a 3f lift force, though the magnitude of C_L at this frequency is small, approximately 0.09. This high–frequency response is likely due to vortex shedding from the axial tip and interacting with the downstream portion of the concave cylinder. An alternate hypothesis was the 3f peak was due effects at the free surface such a wake–induced oscillation, but given that the convex cylinder had the same boundary conditions this can be ruled out.

By continuing the force reconstruction process for all U^*, the relation between axial tip orientation and higher harmonic forces can be discerned. In figures 4.13 and 4.12 are plotted the force FFT spectra of the curved cylinder for both (a) concave, and (b) convex orientations. Here the FFT coefficients are plotted in log scale, with frequency on the left axis, and oscillation amplitude on the right axis. As well, Strouhal trends for a stationary uniform cylinder ($St = 0.2$), are plotted on the left axis. For both the concave and convex orientations, the Strouhal trend is an indicator of the onset

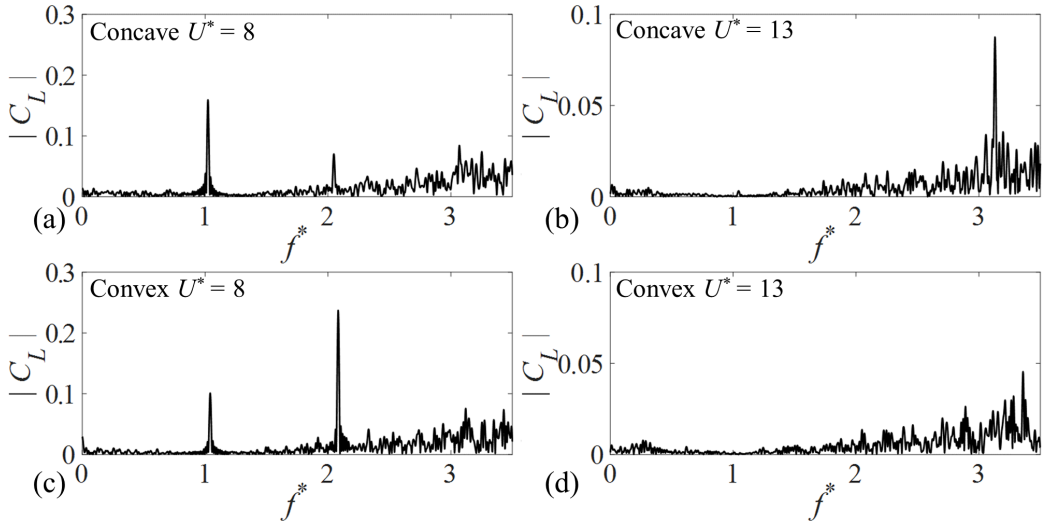

Figure 4.11. Spectral FFT contents of C_L, the lift coefficient for the concave(a, b) and convex (c, d) cylinder at U^* of 8 (a, c) and 13 (b, d)

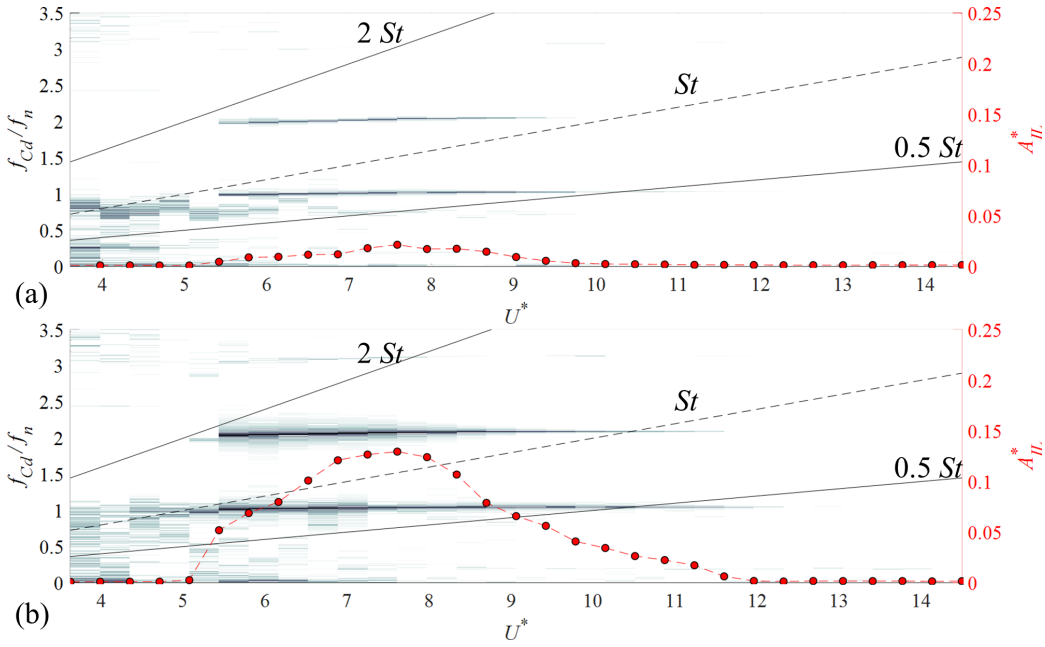

Figure 4.12. Reconstructed lift force spectra for the curved cylinder in (a) concave and (b) convex orientations. Left axis FFT coefficients, right axis crossflow amplitude

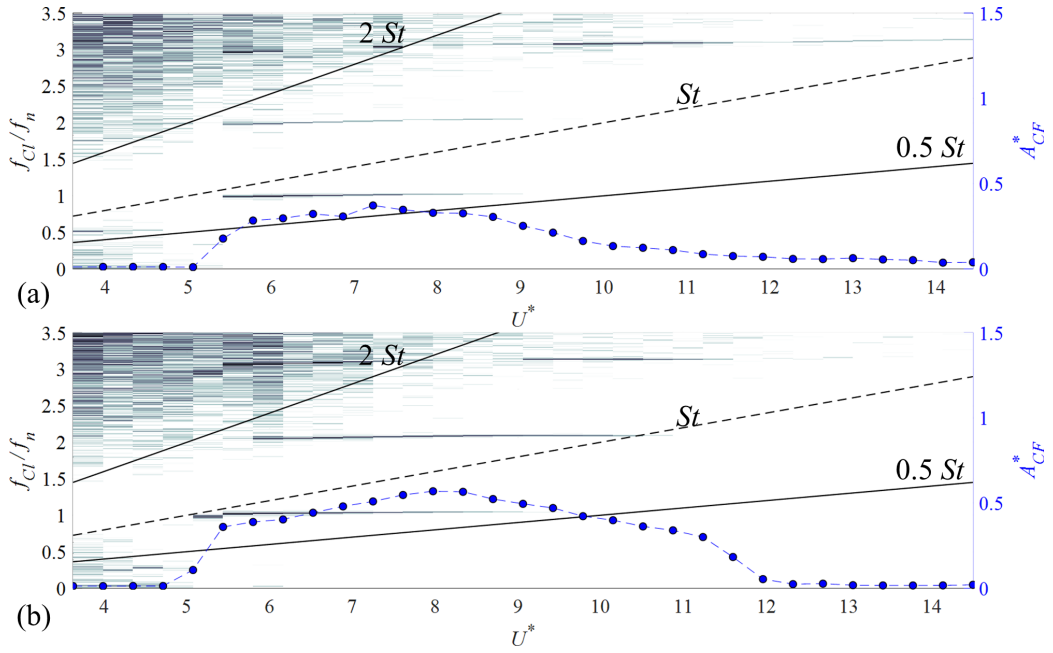

Figure 4.13. Reconstructed lift force spectra for the curved cylinder in (a) concave and (b) convex orientations. Left axis FFT coefficients, right axis crossflow amplitude.

of lock–in, as the first oscillatory case for both occur as $\frac{f_{CL}}{f_n} = \frac{f_{vs}}{f_n}$ (Figure 4.12(a, b)). Between the two cases the spectral contents of the drag force is qualitatively unchanged between the concave and convex cylinder, so it will only be noted that the decreased contribution of all the C_D harmonics for the concave cylinder (Figure 4.12(a)) agrees with the observed collapse of the inline oscillation component for the concave orientation (Figure 4.8).

Compared to the drag force frequency contents, the lift force FFT provides much greater insight into the different response regimes of both cylinders (Figure 4.13(a, b)). Throughout lock–in both concavities maintain a synchronization between the lift force and the natural frequency, staying near a ratio of 1 from $U^* = 5$–9. In the convex case however the harmonics appear with a greater magnitude, indicating stronger forces. The greater question though surrounds the appearance of a 3f band at $U^* = 9.4$ for both orientations. The $2St$ trend is close to the 3f formation and may

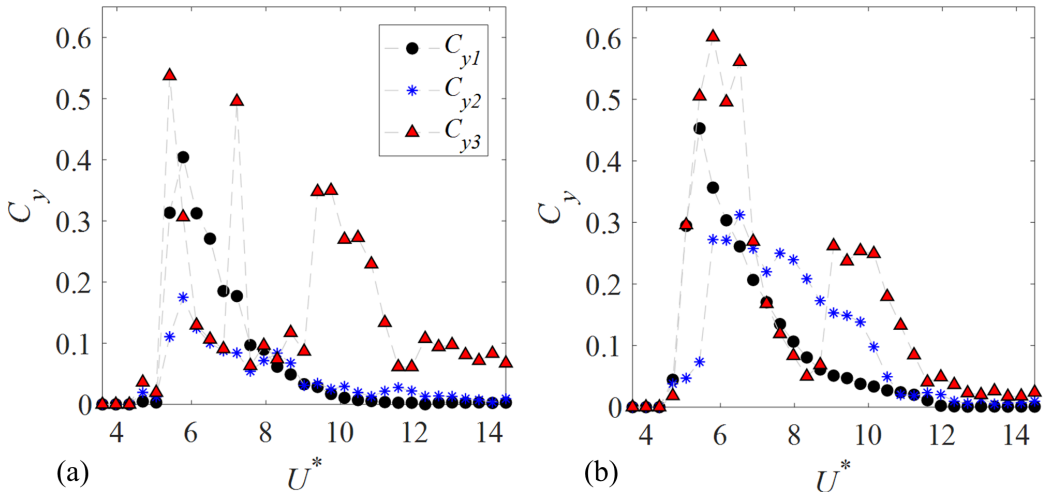

Figure 4.14. Reconstructed lift force harmonics for the (a) concave and (b) convex orientation.

align if an experimental St number is used instead of 0.2 for a uniform cylinder. Due to the continuous curvature of the cylinder and downstream interference however St is likely to change along the length of the cylinder and depend on concavity. In the present work, it was calculated that $St = 0.17$ would align the 3f band with the $2St$ trend, but this is a consideration for future work due to the previously mentioned limitations on measuring St for this geometry. While both concavities form the 3f band at $U^* = 9.4$, it decays towards zero for the convex orientation, dropping the oscillation amplitude towards zero. These trends are also separated as 1st, 2nd and 3rd lift force harmonics in figure 4.14. For the concave cylinder, the 3f band does not have a consistent value but does manifest throughout the higher U^* higher, in agreement with the observation of the extended lower branch. Mentioned earlier in this section, the similar boundary conditions between the concave and convex cylinder rule out this branch being driven by the free surface, so therefore the 3f lift force contribution can be directly linked to the axial tip of the concave cylinder influencing the downstream dynamics.

4.4 Conclusions

Vortex-induced vibration was studied for a curved cylinder with crossflow and inline degrees of freedom in water tunnel flow. The mounting was validated for 2D VIV of a uniform cylinder with a 2:1 crossflow–inline natural frequency ratio and found to be agreement with the amplitude responses reported in literature, as well as found to react properly to changes in mass ratio. The uniform cylinder exhibited counterclockwise figure-eight orbits for all U^*, indicating flow excitation of the structure. A curved cylinder was examined for different modes of flow–induced oscillations and investigated for whether these modes depend on concavity (concave being with an axial tip upstream, and convex with the upright portion of the cylinder upstream). The curved cylinders were tested in both orientations for U^* =2–15 and the crossflow–inline response recorded. The convex cylinder responded with significantly higher amplitudes during lock–in than the concave case, and both the crossflow and inline oscillation amplitudes sustained nearly constant values across the lock-in region. The figure–eight orbits were counterclockwise at all U^* for both orientations. The concave case uniformly saw a reduction in figure-eight amplitudes, but also maintained counterclockwise orbits and sustained an extended lower branch compared to the convex orientation, which did not. Force reconstruction showed the extended lower branch was driven by a 3f lift force. While the convex cylinder also formed at 3f band at $U^* = 9.4$, it decayed to zero magnitude by $U^* = 12$ which due to a lack of other forces eliminates the lower branch.

CHAPTER 5

A BIOMIMETIC ULTRASONIC BAT DETERRENT DRIVEN BY FLOW-INDUCED OSCILLATIONS

In this chapter, the mechanisms of an ultrasound-emitting larynx are studied as a t-shaped oscillator undergoing flow-induced oscillations.

5.1 Introduction

By recent estimates, approximately 600,000 bats were struck by wind turbines in 2012 in the US alone [51]. This is detrimental to overall bat populations, which are attributed to $3.7 billion in agricultural savings each year [23], and are already threatened by white nose syndrome [5]. This has led to the recognition of the need for deterrence techniques to limit bat mortality at wind development sites. The current deterrent technology to have been proven in literature and field studies is an electronic deterrent designed to be mounted on a turbine nacelle. This device consists of 16 transducers in a 4×4 matrix which emits continuous broadband ultrasound from 10-100 kHz [7]. The transducers transmit maximum power at their resonant frequency of 50 kHz, which results in a sound pressure level (SPL) of 122 dB at 1m. This prototype device has been shown to reduce bat activity within 12 m of the device by 90%. [8]. However, the device did not have an effect on bat mortality under actual conditions when placed on the nacelle of an operational wind turbine. This result was attributed to the propagation nature of ultrasound, which decayed such that it was only of sufficient SPL to deter within 30 m of the device (Figure 5.1, reproduced from [8]). With a 45 cm $\times$ 45 cm frontal area and mass of 0.9 kg the device is overly

Figure 5.1. Calculated effective deterrence zone of a current ultrasonic emitter design on a 2 MW wind turbine [7].

massive for placement on the turbine blades, the region where deterrence is needed but not covered by current devices.

Other studies have shown that the broadband nature of current ultrasonic emitters is another factor in how ineffective they are, in that artificial approximations of natural sonar pulses are effective as long as they are biomimetic in terms of duration, bandwidth, and frequency of occurrence [56]. This finding is supported by studies on free-tailed bats ([19], [58], [57], [105]) which suggest that bats respond much more strongly to sounds mimicking conspecific sonar pulses than to continuous tones or broadband noise stimuli. In these studies, artificial pulses needed to be roughly 60 dB-SPL or louder to evoke behavioral responses from the bats, indicating that bats show behavioral responses to other bats at distances of approximately 20 meters or less [58].

These findings are consistent with acoustic models which suggest ultrasonic deterrents would have to be at least 65 dB SPL to mask bat echolocation calls, effec-

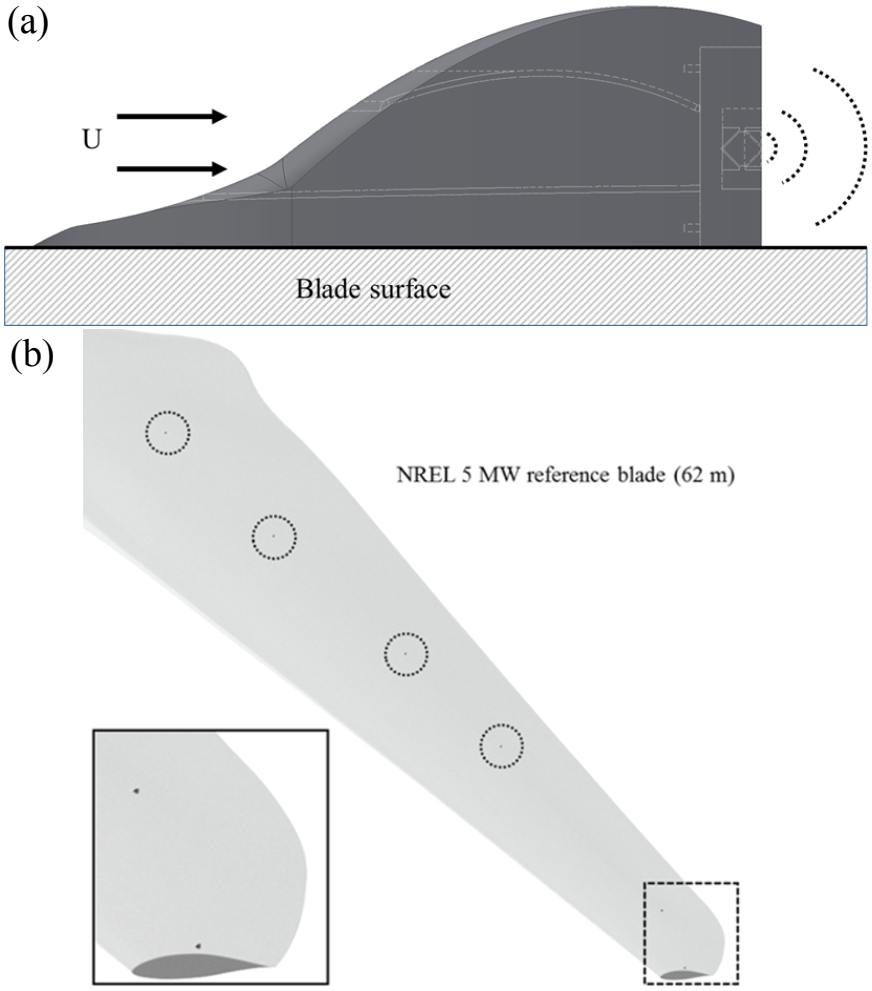

Figure 5.2. Scale of (a) bat deterrent schematic on (b) a full-scale NREL 5 MW wind turbine blade.

tively jamming their navigational abilities [8]. Little brown bats (*Myotis lucifitgus*) show a hearing threshold of 10-22 dB in the 20-60 kHz range [33], while Big brown bats (*Eptesicus fuscus*) show a threshold of 7-46 dB for 20-60 kHz, with relatively lower sensitivity (closer to 30 dB) for 32-46 kHz range [33]. Eastern red bats (*Lasiurus borealis*) are less sensitive, with a threshold of 30 dB in the 20-55 kHz range [76]. Together, these studies of different *Vespertilionidae* species can be reduced to a mutually-inclusive 20-55 kHz range.

To generate a deterrent ultrasonic pulse as described by Jarvis [58], without the range and placement limitations of current devices [8], the present work proposes a series of ultrasonic whistles to be affixed to a wind turbine blade (Figure 5.2(a)), which produce broadband ultrasonic noise through mechanical means. These whistles are intended to be operated passively, blown by the relative flow about a rotating turbine blade (Figure 5.3), and to be positioned at intervals along a turbine blade (Figure 5.2(b)). As previously discussed, bats have been shown to be susceptible to imitations of naturally occurring ultrasonic pulses, thus the mechanisms of the proposed deterrent will take a biomimetic approach by applying the fundamentals of how biological larynxes generate ultrasound. In other words, the internal structure of the whistles is based after that of a bat larynx, which responds in a non-linear fashion to small changes in air pressure, allowing for aperiodic changes in frequency and volume of sound produced. This permits a deterrent device that produces short, broadband ultrasound pulses in the sensitivity range of most bats most impacted by wind turbines (20-55 kHz). In addition, a biomimetic approach allows the design to take advantage of the various nonlinear phenomena which occur for an oscillating vocal fold in flow, such as hysteresis and frequency jumping, to approximate the duration and frequency of occurrence (i.e. chirps) requirements found by Jarvis [58].

Because the source of sound generation would be mechanically driven, this device would not need the power routing which limits current pulse generator placement [8], and if sufficiently low-profile could be placed in an array at intervals along the turbine blade, addressing the problem of rapid attenuation of ultrasound in the atmosphere. As a future outreach of the present work, the profile of such a deterrent could be made compatible to that of turbulence generators, which are placed on wind turbine blades to delay flow separation and increase efficiency ([103], [107]).

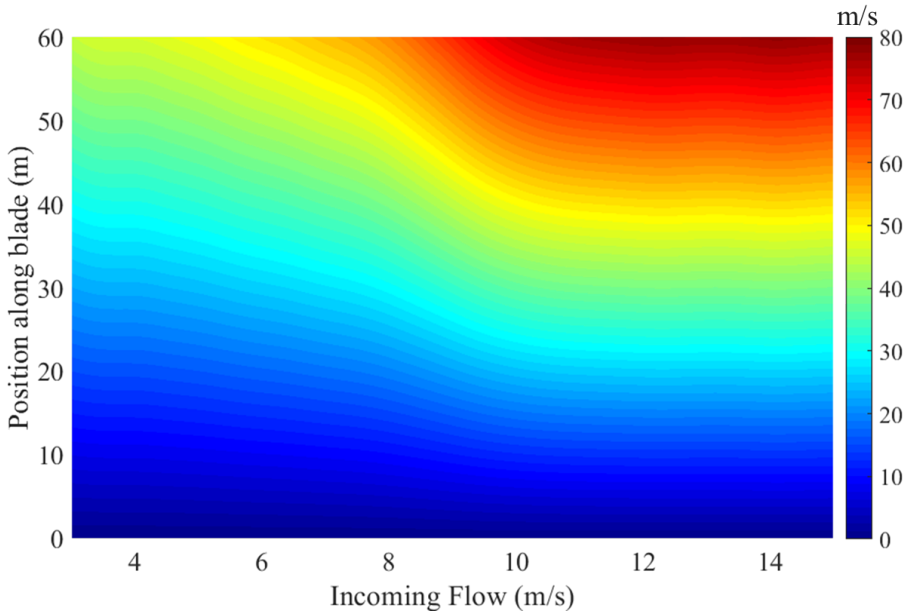

Figure 5.3. Calculated incoming flow velocity distribution along an NREL 5MW blade under operating conditions.

5.2 Methods

The excised larynx of the greater horseshoe bat (*Rhinolophus ferrumequinum*) provides a model for the generation of varying ultrasound across a range of incoming air pressure. Kobayasi et al. [66] observed the horseshoe bat larynx to exhibit non-linear ultrasound production in response to small changes in incoming air pressure. Importantly, Kobayasi et al. found that the acoustic properties of the bat's sonar pulses were not related to any active muscular forcing of the vocal folds. Instead, the emission is dependent solely on the mechanical properties of the larynx. Different pulse types/characteristics were produced by the bat simply by fine adjustments in subglottic pressure changes. This is central to the present work because it illustrates that naturalistic pulses can be generated by a purely mechanical biomimetic device provided with the appropriate air pressure gradient. Between air pressures of 1.5-3 kPa, the sound intensity of the fundamental frequency rises and then decreases with increasing air pressure, but remains fairly high throughout (63-82 dB SPL). At the

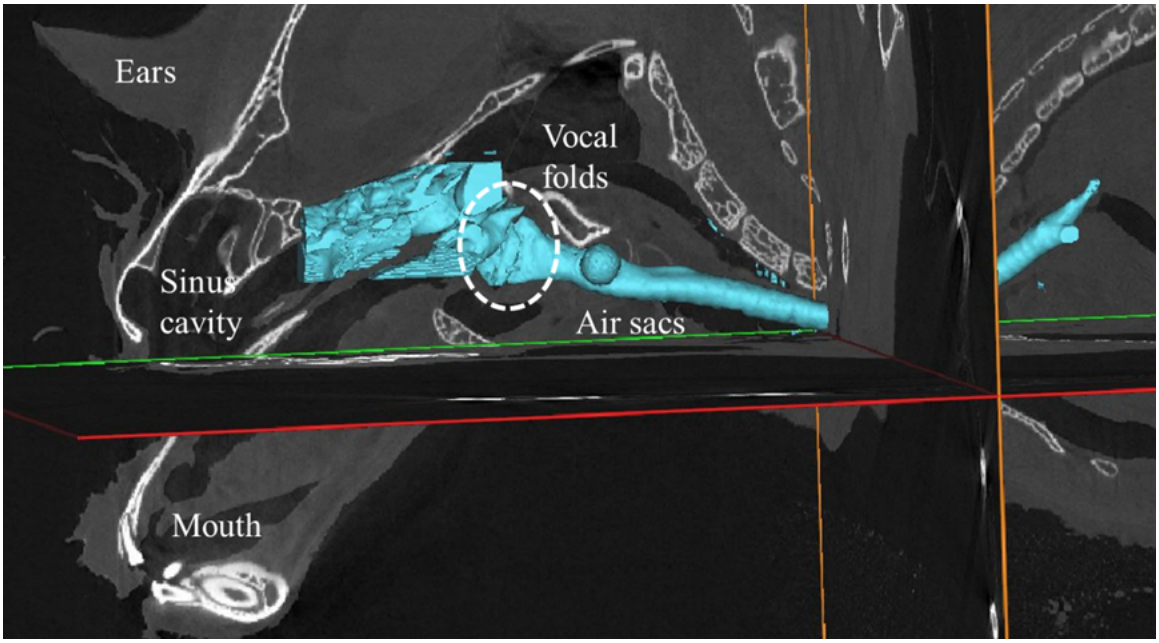

Figure 5.4. Micro Computed Tomography (Micro-CT) scan of a *Rhinolophus clivosusbat larynx*, to serve as reference against axial cross-sections.

low end of this air pressure range, the fundamental frequency begins at or around 32.5 kHz, climbing with increasing pressure to ≈35 kHz. The bat larynx then demonstrates a dramatic frequency jump, with the fundamental frequency dropping ≈13 kHz, to 21-23 kHz range. This frequency jump occurs across a pressure change of less than 0.05 kPa. From this lower frequency, the fundamental frequency again begins to slowly rise. Increasing air pressure above ≈3 kPa leads to aperiodic emission of signals with bandwidths of greater than 10 kHz.

As a preliminary step to reconstructing the geometry of the vocal folds of a typical larynx, an overall view of the respiratory tract was required to check for any possible interference from surrounding structures. To do so, a series of high-resolution image slices of a Geoffroy's horseshoe bat (*Rhinolophus clivosus*) larynx were captured via micro computed tomography (micro-CT) with collaboration from the Harvard Center for Nanoscale Systems. Using a reconstruction program tailored for manipulating

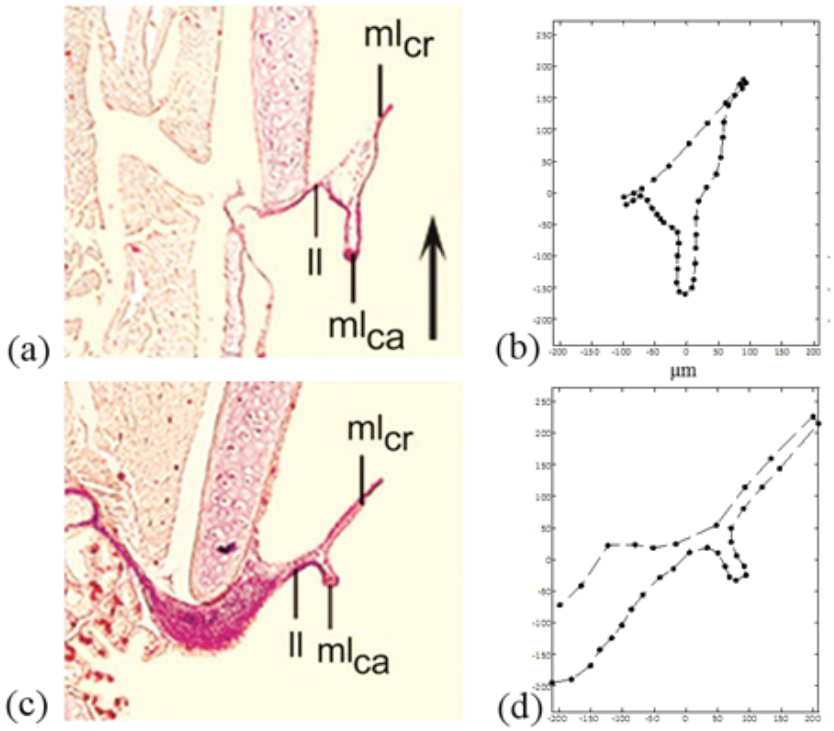

Figure 5.5. One-third and one-half larynx length cross-section (a,c) (From Suthers et al. [101]) with their respective digitized coordinates (b,d).

these images, we isolated the negative spaces of each CT slice, leaving just the air voids within the volume and interpolated the slices to make a fully three dimensional stereolithographic (STL) body. This STL geometry was then filtered to reduce superficial variance inherited from the digitization process. The final result is an accurate portrayal of the interior mechanisms of a bat larynx as a model of the structural conditions which permit ultrasound generation (Figure 5.4). However, the inherent coarseness of the procedure eliminates the fine details needed to ascertain the actual vocal fold cross-sections.

For the high resolution needed for the vocal folds, alternative larynxes with similar mechanisms were considered, such as the concave-eared torrent frog (*Amolops tormotus*) which has been studied more extensively in published literature. Though frequency of calls generally scales with body mass ([42], [100]), the average body mass

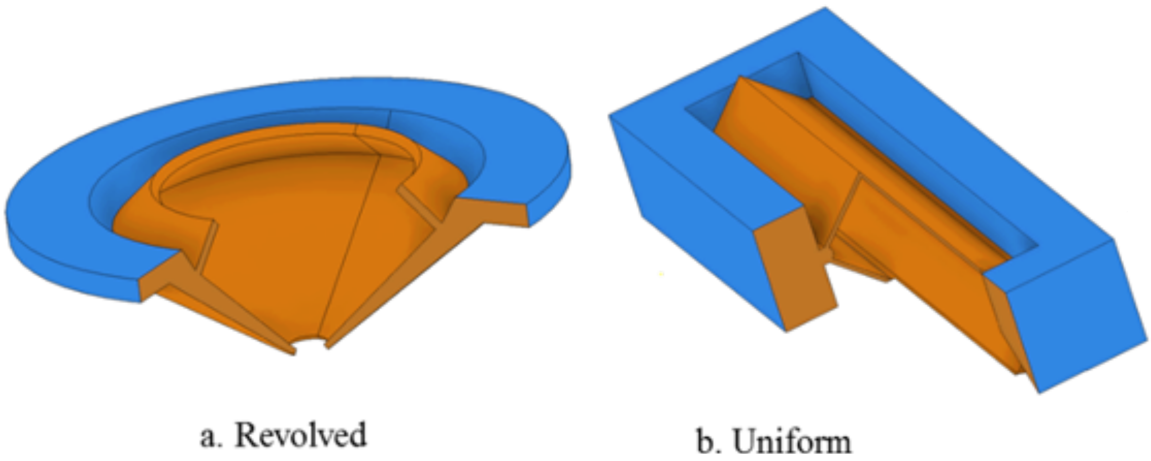

Figure 5.6. Variations of extrapolating the larynx and interpolating between cross-sections

of both the candidate bat larynx and candidate frog are within the same magnitude, in additional to both at minimum having been observed to phonate ultrasonically. In the literature, the interaction of the asymmetry from the various sections is thought to be mechanism behind the ultrasonic communications this species utilizes [101], while for the bat larynx less is known. As a preliminary simplification, the one-half and one-third axial larynx length cross-sections studied by Suthers et al. [101] were digitized for the outline of the vocal ligaments, Figure 5.5. The scale of this larynx is on the order of millimeters, so it was determined to apply an initial scaling factor to bring the overall length to an appropriate size for experimental analysis (and increasing the tension and flow velocity to compensate). This is in line with the anticipated need for a greater flow power than the natural size would provide. By scaling the cross-sections and applying interpolation schema of varying complexity, different larynx prototypes can be constructed. Figure 5.6 shows two fundamental versions: (a) revolving the half cross-section about itself and (b) uniformly extruding the one-half cross-section.

By taking the larynx geometries as negative volumes from a solid, a series of molds were designed and 3D printed on a Stratasys Eden260. An appropriate silicone blend to use as the larynx material was found via subjecting 1 mm $\times$ 10 mm $\times$ 25 mm silicone sheets to incoming uniform 20 m/s airflow. By measuring the acoustic "flapping" noise of the sheet, the appearance of ultrasonic peaks indicate whether that particular silicone blend were flexible and low-damping enough to sustain ultrasonic vibrations. The silicone compound used in the present work was manufactured by Smooth-On, Inc., Easton, PA., with an additional 10% silicone thinner by weight. Instron tests of a uniform cylinder of the material yielded an average elasticity modulus of E = 300 kPa.

5.3 Response of the revolved larynx to incoming flow

The revolved-section larynx was scaled to an inlet diameter of 17.5 mm and cast from the silicone blend. The body was then mounted to a flow diffuser attached to a continuous air source. The diffuser was made of ABS plastic with an inlet diameter of 3 mm, outlet diameter of 17.5 mm and a linearly tapered length between the two faces of 10D, or 175 mm. This serves to condition and stabilize the airflow. 10 cm downstream of the larynx fixture there was an AR125 ultrasonic-capable microphone, to capture any acoustic emissions in a continuous WAV file (Figure 5.7). The flow velocity at the outlet was calibrated using an Omega FMA-905a hot wire probe.

The revolved larynx was recorded for increasing flow velocities until it was observed to reach steady-state, at which point the velocity was held constant for a period of time and then decreased back through zero. For this case no ultrasound was recorded at any flow velocity tested (up to 60 m/s). It was observed that the conical shape of the revolved larynx did not provide interaction between opposing vocal folds, and theorized that the lack on interaction prohibited the frequency jumps seen in excised larynxes. Thus it was decided to apply an external displacement on

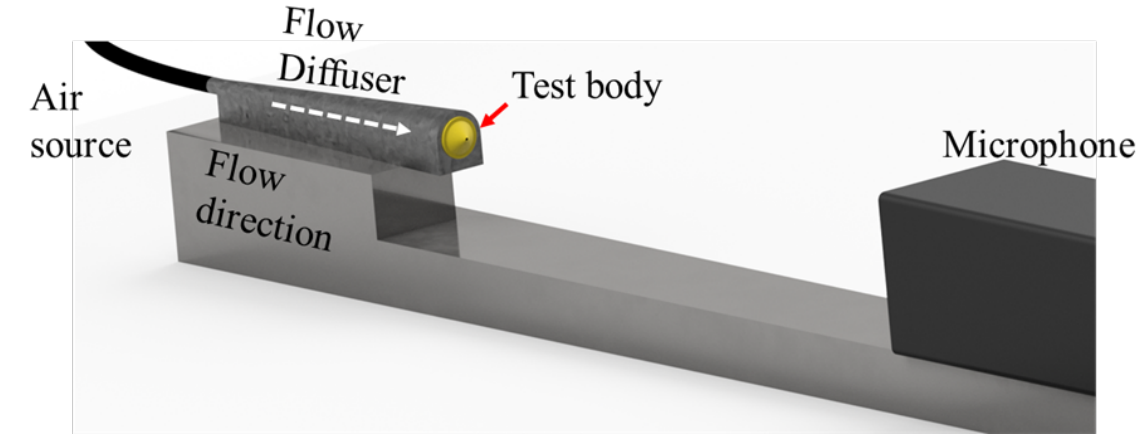

Figure 5.7. Experimental setup used to test the silicone larynx models. The microphone is placed 10 cm from the outlet of the larynx.

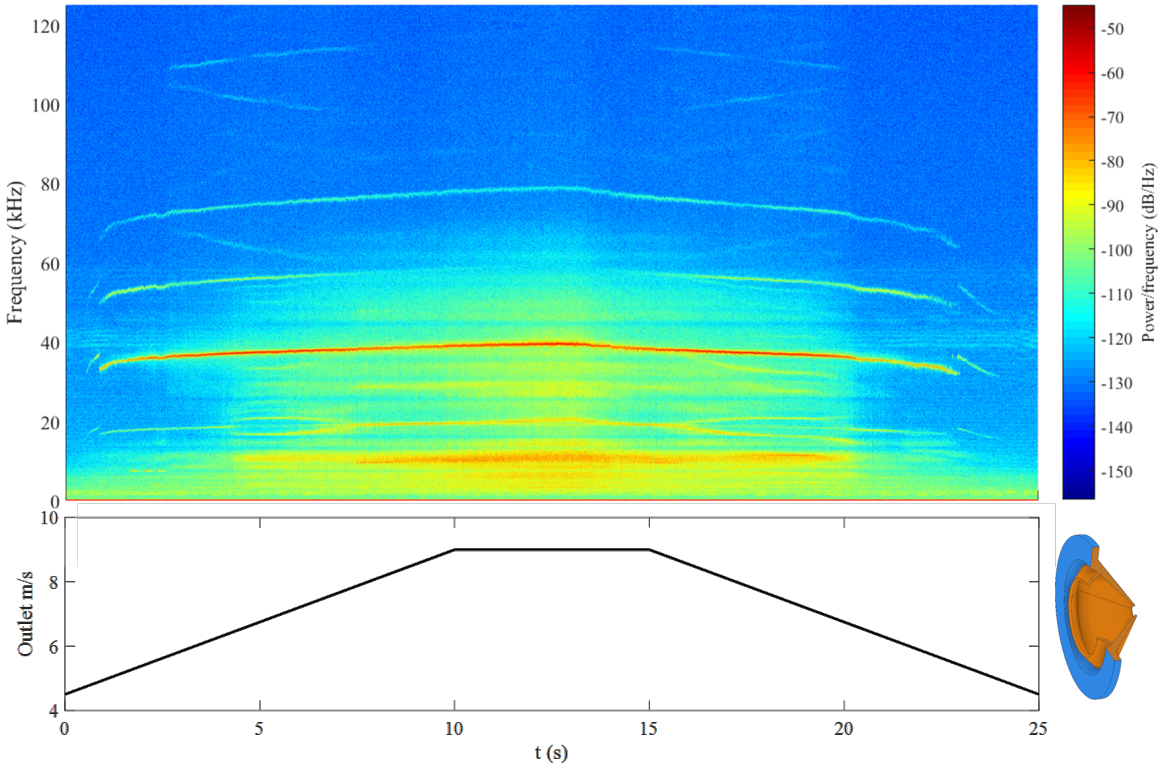

Figure 5.8. Response of the revolved larynx to increasing and decreasing velocities

the larynx outlet, deforming half the cone such that the folds meet in the middle. In doing so, the folds can interact in a manner more similar to the excised larynx. Seen in Figure 5.8 is the summary of this response. The audio signal is reported as normalized power spectral density (PSD), to more readily compare cases which might vary in absolute power. Note distinct bands of ultrasound at approximately 35 kHz, 50 kHz and 75 kHz, which saw frequency-modulation towards higher frequencies at higher flow velocities. However, for decreasing velocities this behavior was did not change and the hysteresis observed in excised larynxes by Suthers et al. [101] was not generally seen here. The only hysteretic spectral formation was a very low-power band near 85 kHz which did not form for the decreasing case. Frequency jumping was observed for both increasing and decreasing cases when the flow was near 6 m/s. As a harmonic diverges from the 75 kHz band at the 3 second mark (approximately 6 m/s) an additional harmonic forms, splits, and diverges in the 110 kHz range. Of interest is that the 75 kHz divergent harmonic is also hysteretic, while the 110 kHz divergence is not.

5.4 Response of the linear larynx to incoming flow

A linearly extruded larynx was cast to a scale of 40 mm $\times$ 10 mm which had both upstream and downstream sets of ligaments touching under zero flow, similar to the configuration seen in the micro-CT scans. To place the larynx in flow a different flow diffuser was constructed with a similar taper ratio as the conical one, but an adapted rectangular section of the same 40 mm $\times$ 10 mm as the linear larynx. The response of the linear larynx, as seen in Figure 5.9, did not have the same effect as the external blockage. The ultrasonic peaks become more broad-banded with increasing velocity, but no clear hysteretic effects are seen for decreasing velocities. The interpolated larynx exhibited similar broad-bandedness.

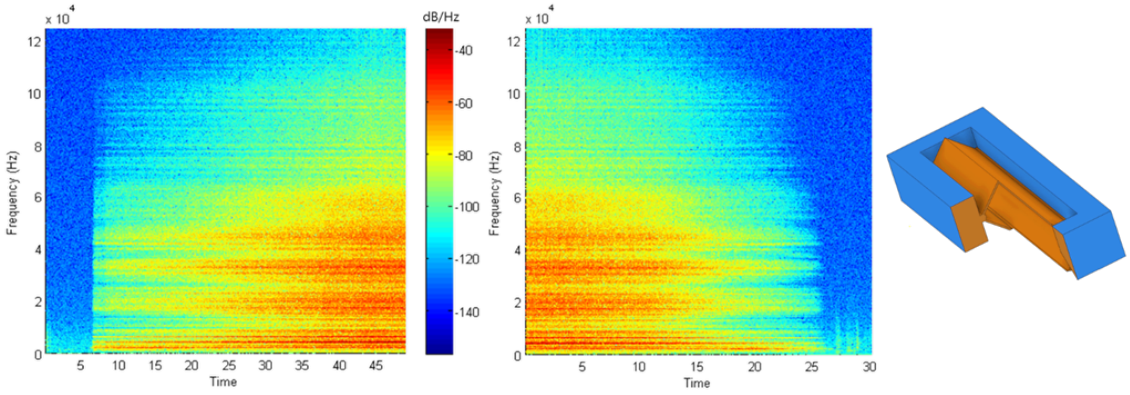

Figure 5.9. Response of the linear larynx to velocity increasing linearly from 0-15 m/s, and decreasing through the same range.

5.5 The influence of tension and the leading edge

Thus far the only the geometrical and velocity parameters have been studied. However, referencing again literature such as Kobayasi et al. [66], an important distinction of larynxes which emit ultrasound is that the emission is not imposed on the vocal ligaments by the surrounding muscles, but rather controlled via tension.

To study the effect of tension on the larynx model response we constructed an apparatus to apply variable displacements to a clamped-clamped film of low-density polyethylene (LDPE). An AR125 ultrasonic microphone was deployed 10 cm downstream of the mounted film to record the ultrasonic response and save it as a WAV file. The initial length of the film measured 12.7 $\times$ 6 $\times$ 0.1 mm, with a material density of 0.92 g/cm^3 and an elastic modulus of 300 MPa (the prior silicone samples had an elastic modulus of $\approx$0.3 MPa). The film had one end clamped to a lab stand, and the other to a mount on a worm gear-driven Velmex XSlide positioning stage to enforce changes in length of the LDPE film (Figure 5.10). This configuration was capable of reaching material strains of 150% before tears in the film propagated. Note that the incoming flow encounters the leading edge of the film. The flow velocity was first increased quasi-statically to determine the point of onset for any acoustic response,

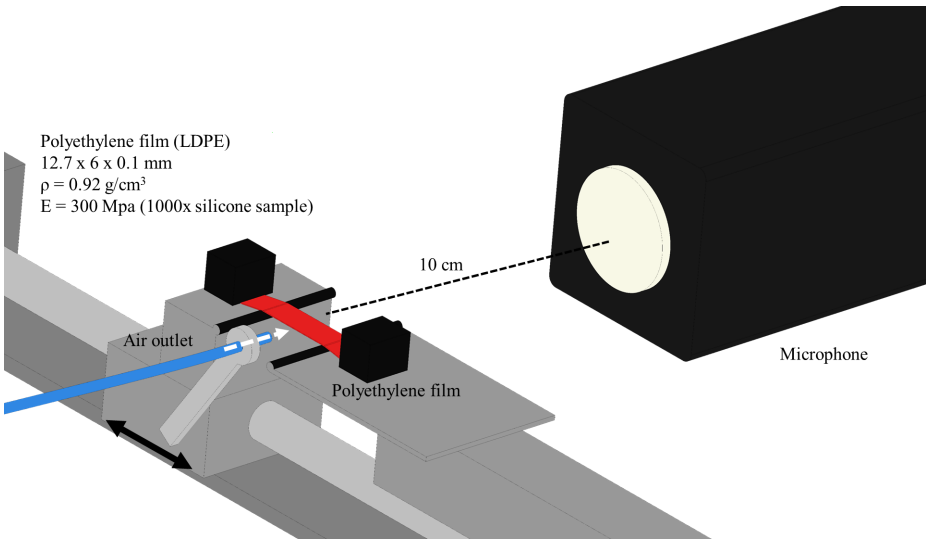

Figure 5.10. Apparatus used to apply strain to LDPE film via a wormgear positioning stage.

as well as any upper velocity limit to the response (actual larynxes eventually buckle at certain flow velocities, as seen by Kobayasi et al. [66]).

Seen in Figures 5.11, 5.12 and 5.13 are the transient responses of the 12.7 mm-long LDPE film to increasing strain. The acoustic power for these cases are reported in Sound Pressure Level decibles as recorded from the microphone 10 cm away from the setup. The initial case is just with enough displacement to remove any visible slack (referenced hereon as 0% increase) from the system, and the higher cases are noted by their percent length increase relative to that initial slackless length. What we see is that in particular for the 0% case the system exhibits very similar frequency jumping and doubling as the actual excised larynxes studies by Kobayasi et al. [66], but with the dominant harmonic in the audible range (below 20 kHz).

At film tensions of 30% and 70% added strain, there are noticeably fewer frequency jumps than observed in the 0% case, and only sporadic frequency doublings. Instead the frequency of the dominant harmonic increases approximately linearly for increasing flow velocity, and any frequency jumps are into a higher frequency of the

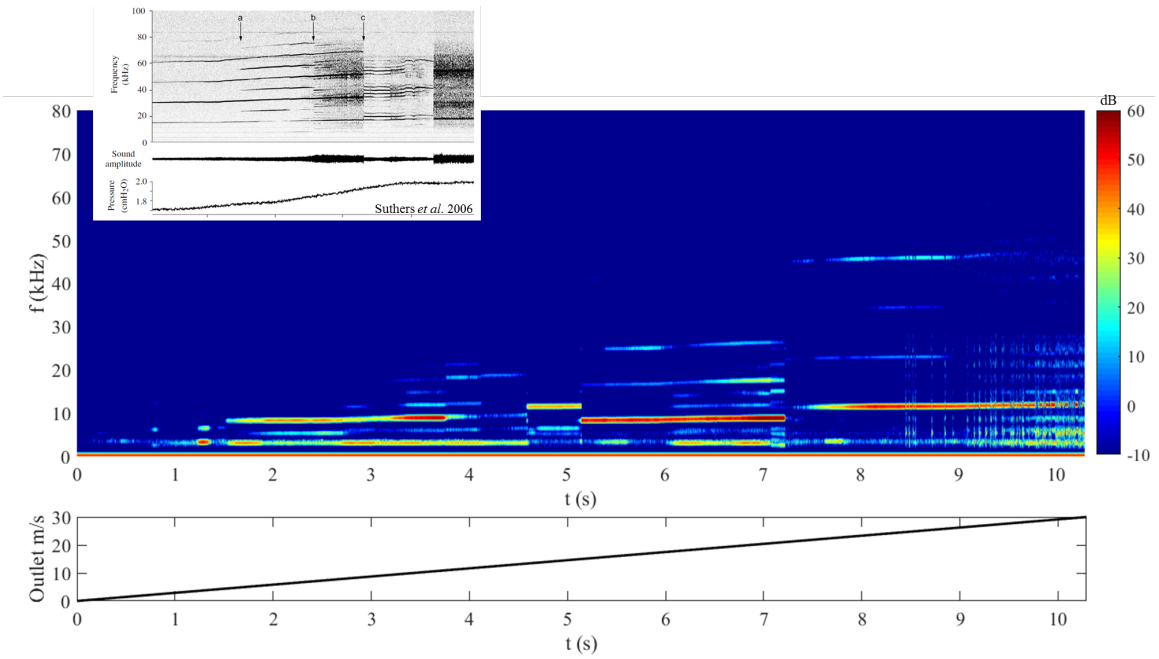

Figure 5.11. Response of an LDPE film to edgewise ramped flow velocity on the order expected for a rotating turbine blade.

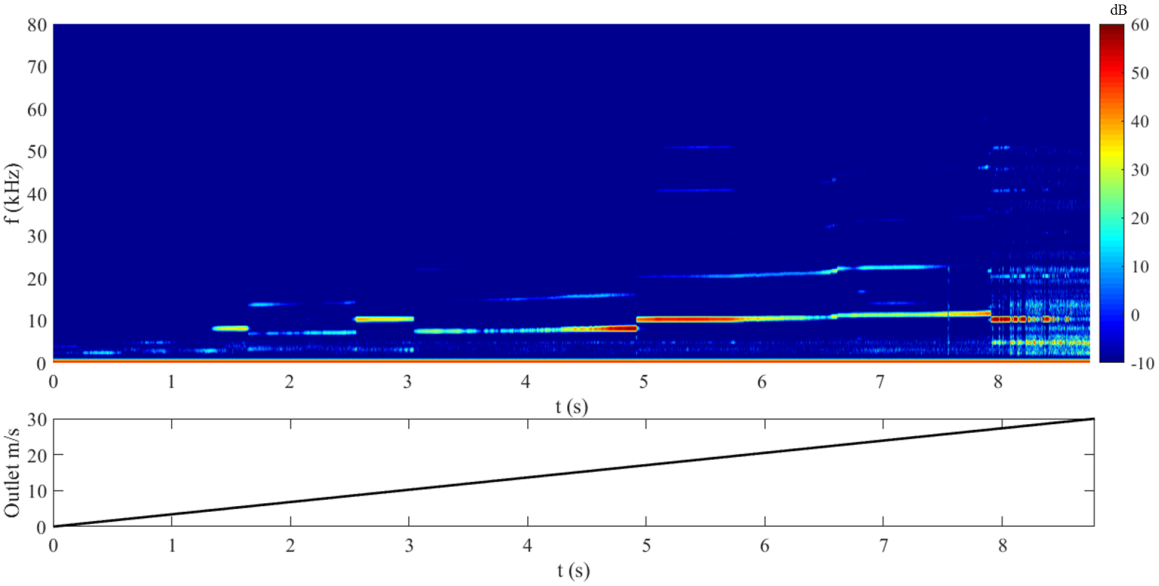

Figure 5.12. Response of an LDPE film with strain increased 30% from slackless to edgewise ramped flow velocity on the order expected for a rotating turbine blade.

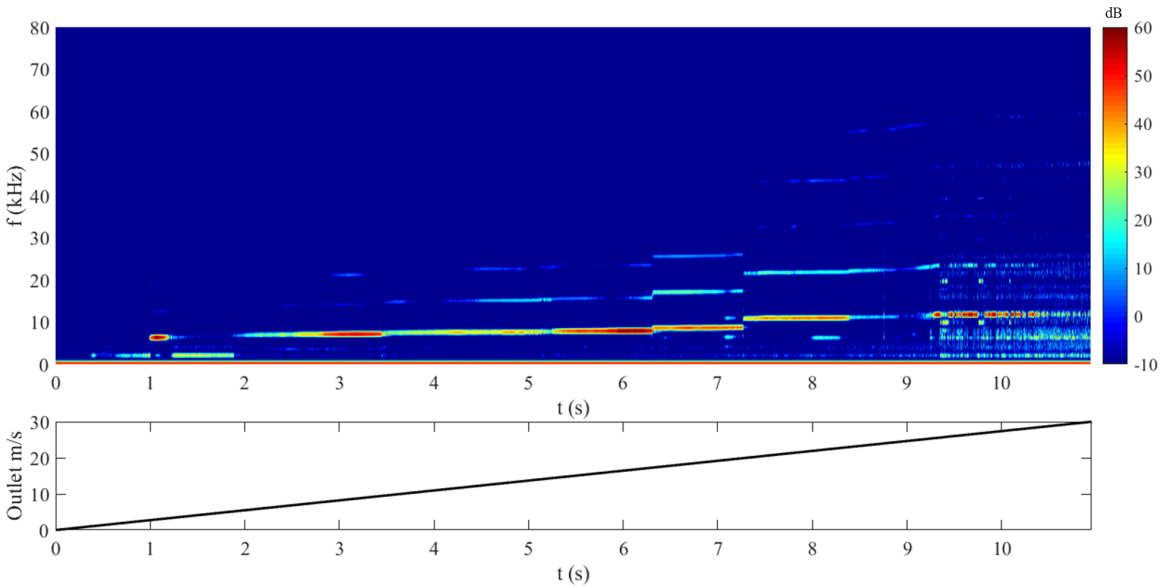

Figure 5.13. Response of an LDPE film with strain increased 70% from slackless to edgewise ramped flow velocity on the order expected for a rotating turbine blade.

same mode (i.e. same general trend to the harmonic bands as before the jump but at a higher frequency). This phenomenon is accompanied by a build-up in the acoustic power immediately leading up to the jump. Clearly seen in Figure 5.12 between the 5 and 8 second marks: the power builds before the jump at t = 5 s, decays to a local minimum at approximately t = 6.75 s, then builds again before the final jump at t = 8 s. The same can be seen at 70% strain (Figure 5.13) for jumps to higher modes at t = 3.5 s, 5.25 s and 6.25 s. Given the similarities to the excised larynxes studied by Kobayasi et al. [66], the trend emerges that larynx mechanics can be represented as a tensioned film with edgewise flow. However, with the leading edge and flow-induced tension both influencing the response, an additional experiment whereby the leading edge is eliminated is required to determine the significance of initial film tension.

5.6 The role of flow-induced tension

To separate flow-induced tension from the effects of pre-tension and the asymmetry from having a leading edge, a second film-based model was built to the same dimensions as the axial-flow film, but now with the incoming jet orientated perpendicular to the film (Figure 5.14). With the flow impacting the center of the film, the higher drag force deflects the film and increases the tension buch more uniformly than for the axial case, where flow-induced tension is focused on the leading edge. A minimal pre–tension was applied to the film to elimate any sag, and referred to as null pre–tension hereafter as per the axial case. At 0% tension an approximate peak increase of 40 dB can be seen (Figure 5.15) compared to the axial-flow film (Figure 5.11). However, without interaction between the leading edge of the film and the flow, the system lacks the requisite coupling of a larynx resonator to permit significant frequency jumping. Flow-induced tension is dominant and results in acoustic bands linearly scaling with velocity and minimal hysteresis. 15% pre-tension was the highest strain for which the acoustic frequency showed any linearity with velocity (Figure 5.16), only noticeable in the 75 kHz band and nearly constant tones for lower frequencies. The peak tension tested before rupture was 60% (Figure 5.17), where it was observed the films pre-tension is entirely dominant over flow-induced tension, resulting in a constant tone but at a higher acoustic power, as well as more numerous harmonic bands up to 120 kHz.

5.7 Acoustic response as a hypothetical bat deterrent

The strongest signal generated thus far was for a tensioned film with in-plane flow, and strain increased by 60% (Figure 5.17). The dominant harmonic was at 20 kHz and measured to be 95 dB at 0.1 m, and both the power level and frequency range is agreed upon by field studies to be an effective deterrent ([19], [58], [105]). . To estimate the effective range we start with a simplified propagation relationship,

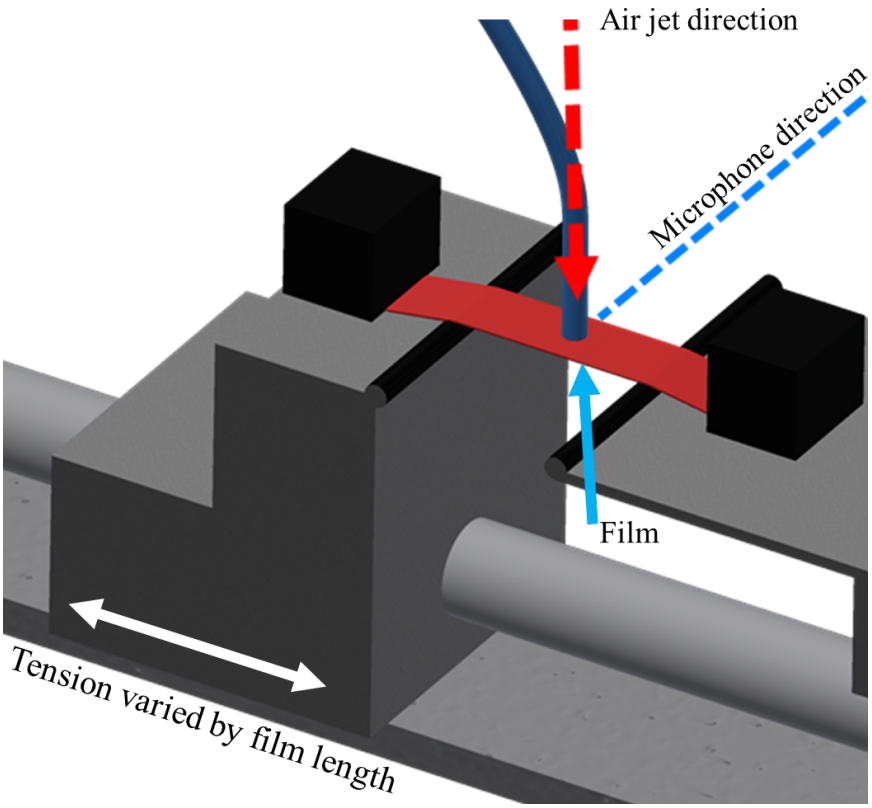

Figure 5.14. Apparatus used to apply strain to LDPE film via a wormgear positioning stage, with flow orientated for in-plane impingement.

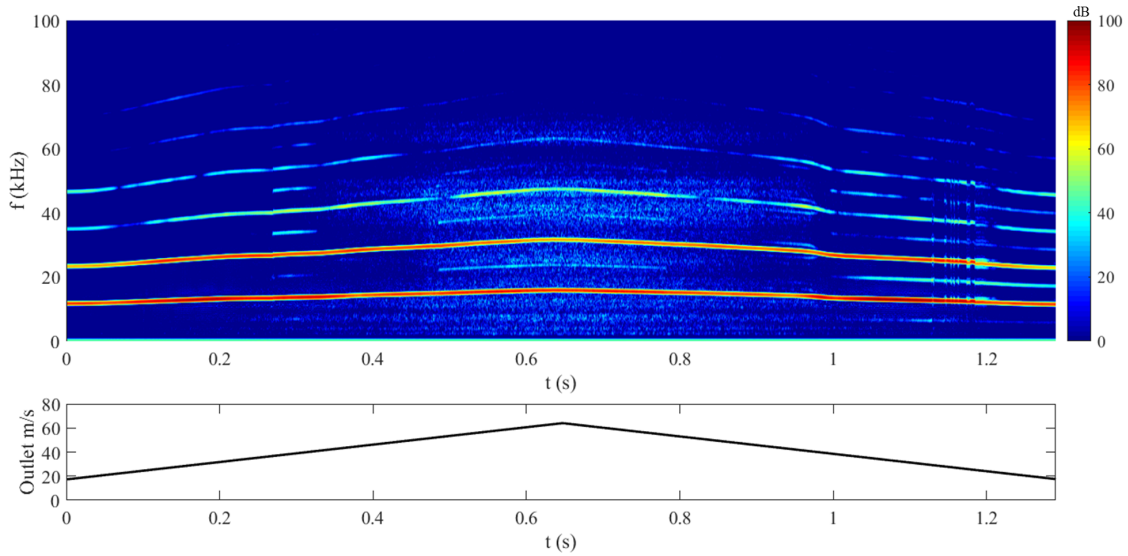

Figure 5.15. Response of an LDPE film to an in-plane fully reversed ramped flow velocity on the order expected for a rotating turbine blade.

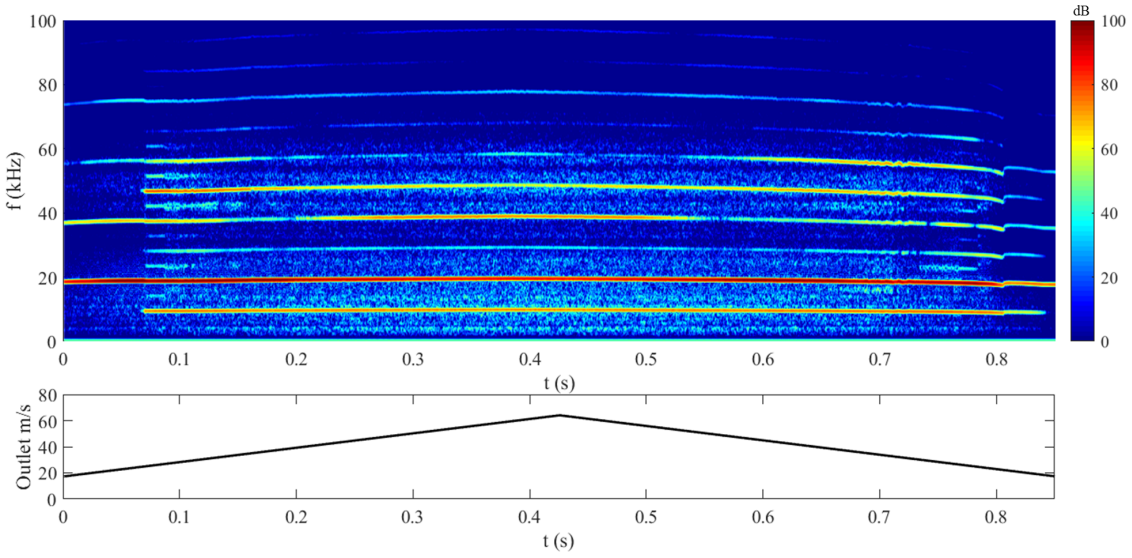

Figure 5.16. Response of an LDPE film with strain increased 15% from slackless to an in-plane fully reversed ramped flow velocity on the order expected for a rotating turbine blade.

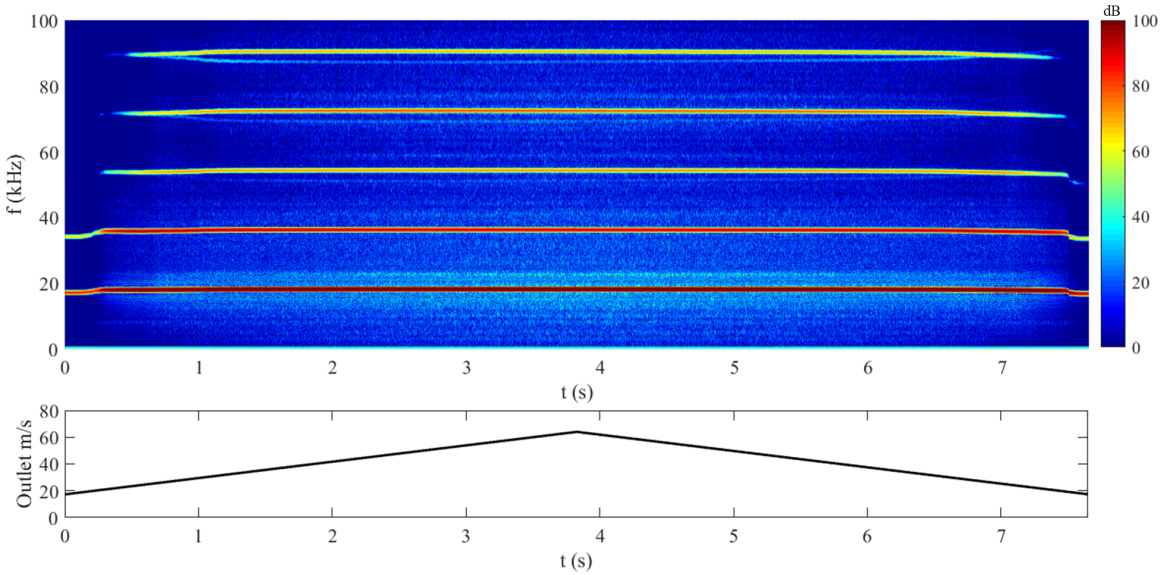

Figure 5.17. Response of an LDPE film with strain increased 60% from slackless to an in-plane fully reversed ramped flow velocity on the order expected for a rotating turbine blade.

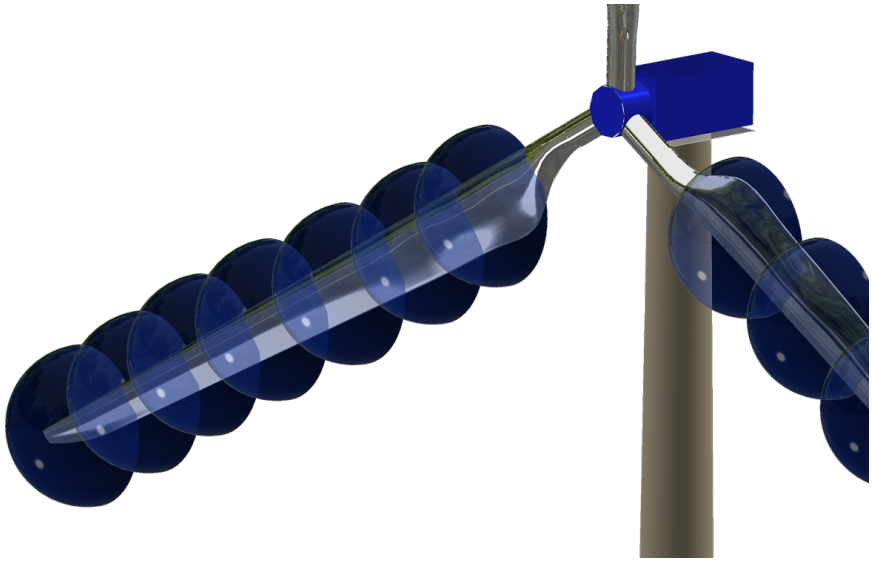

Figure 5.18. Scale of peak accoustic output range given that literature reports 55 dB as the minimum sound power level to deter bats. This estimation indicates our strongest emission (20 kHz at 95 dB at 10 cm) will deter bats from up to 10 m away.

whereby the power decreases by the inverse square of distance. In log-scale, this results in a 6 dB decrease per doubling of distance. Literature on bat deterrent ([57],[58],[105], [19]) indicate 55-60 dB is the lower bound for signals strong enough to influence bat behavior. Combining this sensitivity threshold with the propagation relationship gives an effective range of 10.1 m for the 20 kHz signal. To understand how this relates to wind turbine deployment of the deterrent, let us consider the 5 MW reference turbine from NREL [61]. At a cut-in flow velocity of 3 m/s, the rotor is at approximately 7 rpm [61], with a tip-speed ratio of 3 yielding a relative flow velocity of 45 m/s at the tip of the blade. With the simplified hemispherical sound propagation model, spacing deterrents every 8.7 meters such that there is 7 deterrents per blade (Figure 5.18) results in a maximum range decrease of 10% for points immediately between two deterrents. If spacing is decreased to 5 m (12 per blade), the peak loss drops to 3%.

5.8 Conclusions

A simplified model for larynx phonation is devised based on flow-induced oscillations of a tensioned film. For cases with opposing larynx geometries, an acoustic response was only noted for scenarios whereby the mock vocal folds were offset towards the center, such that under zero flow the outlet is fully blocked. Under these conditions, ultrasonic harmonics manifest and scale in frequency with increasing flow velocity. Therefore alternate models were designed which create similar fluid-structure coupling, whereby minute changes in flow can have significant impact on the stiffness and oscillation of the structure. Two canonical examples are a film in axial flow, and with in–plane flow. For axial flow, the incoming jet hits the leading edge of the film first, meaning that any change in the shape of the leading edge has significant influence on how the flow encounters the downstream body. Different pre-tensions were applied to a thin low-density polyethylene film in this orientation for both constant

and ramped incoming flow velocity. Without any pre-tension, remarkably similar frequency jumping phenomena were observed to those of an excised larynx, and the harmonics scaled in frequency with velocity, implying the flow is also stiffening the film. This was confirmed at higher tensions, where the pre-tension dominates the flow-induced tension, and the acoustic response is relatively constant with fewer frequency jumps.

To confirm that a flexible leading edge is the source of the frequency jumping and separable from the pre-tension, the subsequent larynx model was the same thin film but with flow impacting the center, such that the drag experienced by the film is distributed throughout instead of just at the leading edge. Under this orientation, without pre-tension only minimal frequency jumps were observed and there was not significant hysteresis. As with the axial case however, the frequency of the acoustic bands had a proportionality to velocity. For higher pre-tensions this proportionality decreased to almost zero at 15% tension, and purely constant tones beyond that. The maximum case tested, 60%, also had the strongest power output and the highest frequency 1st harmonic at 20 kHz and 95 dB from 10 cm. This was constant across the 20-65 m/s range.

CHAPTER 6

CONCLUSIONS AND FUTURE WORK

Flow-induced oscillations are well studied for simple geometries, but for symmetry-breaking structures with more than one degree of freedom, their complexity has lead to a relative lack of understanding as there was simply not enough supporting literature, but such complexity is required to better match actual engineering applications. This was the inspiration for this thesis, to better apply fundamental experiments to the offshore wind environment by creating flexibly-mounted structures with more similarity to their full-scale counterparts versus existing flow-induced oscillation literature which tend to be simpler in focus.

In this thesis, we experimentally studied the structural dynamics, wake interaction, and fluid forces acting on the multiple degree of freedom systems typical of floating wind turbine components undergoing flow-induced oscillations. The applications are novel, and the fundamental fluid-structure interactions are new to science. A separate biomimetic study is also discussed. The passive flow-induced oscillations found in bat larynxes for ultrasonic echolocation is studied, and the role of pre-tension versus flow-induced tension on frequency doubling is examined. The mechanisms are replicated as a device which generates ultrasound using the flow over a turbine blade, for eventual deployment on wind turbine blades as a bat deterrent.

6.1 Conclusions

Chapter 2 presented experimental analysis of cylinders and prisms in flow with crossflow-inline flexibility, and the role of vortex-surface alignment as the angle of attack changes is examined. It was concluded that

- For a triangular prism with an angle of attack of $\alpha = 60°$, all U^* for which the prism oscillated exhibited CCW figure-eight orbits.
- The greatest inline amplitude contribution (highest CF-IL phase angle) was 30° at $U^* = 7.2$ and 7.9, equal to one-half the normal angle of the afterbody
- The vortex attaches further downstream on the trailing face of the afterbody for decreasing α, for cases at the same U^*.
- At 30° the vortex on the side of the trailing face of the afterbody is entirely detached from the prism, and no oscillations are observed.
- For a square prism at 45° angle of attack. The symmetry of the prism permits shedding patterns similar to those of a circular cylinder undergoing VIV, and thus the square prism responds with classical vortex-induced vibrations across a similar U^* range as the uniform cylinder.
- At an intermittent angle of attack of 22.5°, once the cylinder begins to oscillate, the relative component of flow velocity suddenly moves the shedding point from the edge preceding the trailing face to the leading edge on the leading face. Thus, despite being fully exposed to flow, a vortex forms on the leading face. The motion of the cylinder leads to the vortex "rolling" down the face as the cylinder reaches an oscillation apex, and on the return rolls over the preceding edge of the trailing face, where it is caught by the wake and attaches to the trailing face of the afterbody.

- Also for a square at 22.5°, the 2D oscillation collapses to a single lobe past $U^* > 9$. Here a vortex was observed to still form on the leading edge and get caught on the trailing face of the afterbody, but on the opposing side (leading face of afterbody) flow separates as a jet which remains parallel to the surface, preventing vortex formation.

- For a square prism at 0° angle of attack, as U^* increase velocities vortices remain attached to the afterbody progressively longer through the oscillation cycle before shedding. The progression is approximately linear with increasing velocity, until $U^* = 9.4$ beyond which for higher velocities the vortex rolls over the trailing edge of the prism and attaches to the trailing face.

- For all U^* tested where a vortex attaches to the trailing face, the vortex detaches as the cylinder approaches the midpoint of crossflow oscillation, imparting an impulse in the inline direction as it does so. This galloping kink has been previously observed for pure crossflow freedom, but only calcuated for 2D flexibility.

- The galloping kink results in a third lobe in the oscillation orbit, and manifests in the recorded drag force as odd-integer harmonics.

- The outer lobes have opposing CW/CCW rotation, and are CCW if a vortex can form on the side of cylinder at the peak crossflow displacement before attaching to the afterbody, and CW when the flow remains attached until forming a vortex on the trailing face. The orientation competitively swaps between CW and CCW, but both the CW lobe and the CCW lobe have a vortex attach to the trailing face, and thus the middle lobe appears regardless of whether the prism returning the midpoint of crossflow is coming from the CW side or the CCW side.

In chapter 3 a model spar platform was designed to-scale as the Hywind demo turbine, with similar moorings points to match the three-dimensional rigid body motion

flexibility permitted by the actual design. As well, the model spar was designed with the appropriate ballast to match the metacentric height of the Hywind turbine. Orthogonal cameras tracks the pitching, yaw, and heave of the structure for increasing U^*. It was found that:

- For the scaled model, counterclockwise figure–eight orbits of the lower portion of the turbine were observed for all U^*, despite having $f_{nCF} = f_{nIL}$. The upper portion of the turbine (above the mooring point, with the center of mass of the whole structure below the mooring point), had opposite phase and experienced clockwise orbits as the cylinder oscillated with a node at the mooring point.

- Synchronization between the crossflow oscillation frequency and the vortex shedding frequency confirmed lock–in and vortex–induced vibration was present.

- Numerical studies predicted that for continuously flexible structures, counterclockwise orbits can only indicate excitation by the flow, while clockwise can mean either excitation or damping. By suppressing vortex shedding along either just the top or bottom of the cylinder (with the middle being the node which does not oscillate), we confirmed this hypothesis.

- Helical strakes along the entire cylinder suppressed all motion for all U^*, but strakes above the node only inverted the phase of the lower portion of the cylinder, and actually increased the oscillation amplitude at peak U^*. Suppressing the lower half of the cylinder, which was previously undergoing CCW orbits eliminated the vibration of the entire structure. This confirms that vortex shedding suppression methods can be applied to only portions of a structure undergoing counterclockwise figure–eight orbits, and still be effective because excitation of those parts is dominant in driving the response of the structure as a whole.

Chapter 4 presents an expanded view on the influence of mooring cable concavity on hydrodynamic damping. An existing dataset (Seyed-Aghazadeh et al. [89]) with pure crossflow freedom is compared to new results using the same cylinder, but with dual crossflow-inline flexibility. In 1D it was reported that when the free end of a cylinder curved into a semicircle is upstream of the rest of the body (concave, convex being with an axial tip downstream), the axial tip trips the flow and reduces correlation along the length of the afterbody.

- Vortex–induced vibration occurs for both orientations. Notably, the third harmonic of lift manifested with significant contribution in the convex orientation, increasing the crossflow and inline oscillation amplitudes significantly compared to the concave cylinder. Both cylinders responded to a 3f harmonic at higher U^* (above 9), but the band decayed for the convex cylinder near $U^* = 11.5$. The concave cylinder sustained the 3f band and resulted in an extended lower branch.

- Additional stiffness ratios were tested for all U^* and for both convex and concave. It was observed that vortex-induced vibration has a significant effect at 2:1 and 1:1 IL:CF ratios. Non-integer ratios resulted in a collapse of both the crossflow and inline component, while 2:1 saw stable figure–eight orbits and 1:1 had circular orbits.

- The additional degree of freedom permitted an extended lock-in region particularly for the concave case, in agreement with a 1D system.

- Force reconstruction showed dominant third harmonics in the lift force for high A^* convex cases, a new find over previous 1D systems which were apparently too constrained to observe this.

- The extended branch was also shown to be attributed to third harmonic forcing.

In Chapter 5 a new application of flow–induced oscillations is discussed. By recent estimates, 600,000 bats are killed by wind turbine blades in the US each year [51]. To mitigate this, we studied natural mechanisms which produce ultrasound in order to create an air–driven bat deterrent to mount on turbine blades, as field surveys have shown that ultrasound in the 55–60 dB range disorientates bats and can therefore deter them from an area. This chapter studies different simplified larynx geometries in an attempt to mimic their echolocation calls, and compares the results to excised larynxes receiving similar incoming flow.

- A revolved silicone cone has the most basic similarities to larynx vocal folds. For an open outlet exposed to 0–10 m/s ramped flow though, no acoustic response was observed. We noticed that the outlet of the cone only buckled outward and did not oscillate. Thus it was decided to apply an external displacement on the larynx outlet, deforming half the cone such that the folds meet in the middle. In doing so, the folds can interact in a manner more similar to the excised larynx. With this variation, distinct bands of ultrasound at approximately 35 kHz, 50 kHz and 75 kHz were recorded, which saw frequency-modulation towards higher frequencies at higher flow velocities. Similar frequency-modulation was seen in the literature for excised larynxes [101].

- A low-density polyethylene film (LDPE) was devised as an alternate model which was more flexible than the silicone, and arranged in such a way that flow-induced oscillations were guaranteed: with flow approaching axially and in-plane (whereas the silicone was permitted to buckle). The LDPA. Arranged axially, almost identical frequency jumps were observed over the 0-10 m/s range when compared to the excised larynx. By increasing the tension, the ultrasonic bands could be made constant across different velocities, with less frequent jumps. This significance the influence of the leading edge as a dominant source of frequency jumping.

- To confirm that frequency jumps in the larynx model were predominantly from the edge, an in-plane orientation for approaching flow was constructed. In this orientation, the entire drag force of the incoming flow is applied to the film (under the edgewise arrangement, the pre-tension of the film was dominant). At zero slack, the LDPE rarely shows any frequency jumps, with harmonics with increase linearly with velocity and minimal hysteretic features. The peak acoustic output was actually observed for this orientation, with a 12.7 mm initial length strained 60% to 20.2 mm. Here the 20 kHz band is the strongest at 95 dB from 10 cm, but constant across all velocities. While the least "natural" compared to an excised larynxes, this case is certainly applicable as a long-distance bat deterrent if it were coupled with lower-tension cases which act on a shorter distance.

6.2 Recommendations for future work

This thesis covered a number of topics regarding applications of flow–induced oscillations in offshore wind turbines. Therefore there are a number of possible research avenues which could build upon this work, both in the sense of fundamental fluid–structure interactions but also more industrial projects.

- The main area for expansion after Chapter 2 is the inclusion of extra facets to the prisms. We previously emphasized the importance of having both crossflow and inline flexibility, but the progression of an N-sided cylinder going to a perfectly round circular is unknown for this type of setup. Namely, the question remains whether the galloping kink seen for the square prism at $\alpha = 0°$ is only possible with a bluff trailing face purely in the wake of the cylinder. Whether it also occurs for other even-sided polygons also at $\alpha = 0°$ with inline flexibility would certainly be an interesting pursuit.

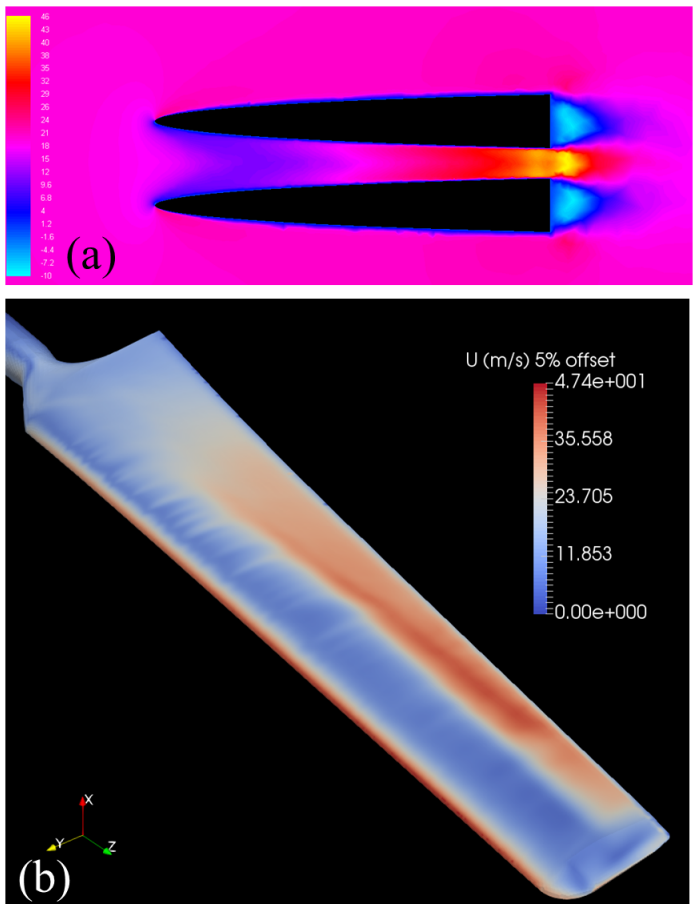

Figure 6.1. (a) Sample openFOAM [112] simulation of the flow about a proposed bat deterrent housing. (b) RANS simulation data from Song and Perot [96] for the NREL Phase VI rotor, post-processed to generate a flow velocity surface offset from the turbine blade. The offset surface is approximately the zone in which the proposed deterrent would operate.

- Chapter 3 discussed only the influence of flow on a floating turbine hull, without a turbine analogue attached. If larger facilities had the capabilities to supply both a constant flow velocity, as well as wind and waves, the nature of VIV in an environment with complete full-scale similitude could be understood. As currently the only floating offshore wind farm consists of spar-type turbine hulls, seeing how subsea strakes operate in conjunction with wind and wave-induced motion would be the next logical step.

- At the current stage, the premise of using flow–induced oscillations as a bat deterrent is a prototype based on simplifications of the larynx geometry. If a fully-resolved micro-CT scan can be taken of a bat larynx, computational methods may have success in modeling the geometry as a deformable mesh with a fluid–structure coupling. The phonation mechanism of bat echolocation is poorly understood in terms of the mechanics, so a numerical approach may be required to validate whether, as we determined here, frequency jumping is primarily reliant on having a leading geometry to trip the axial flow over the downstream ligaments. Additionally, a CFD approach may refine a housing (figure 6.1(a,b)) for the proposed bat deterrent to conduct field trials of the device.

APPENDIX

INSTRUMENTATION

This section details the specifications of the instruments used in the experiments.

A.1 Force Sensor

The force sensor used was a six-axis ATI Nano17/IP68, with an SI-25-0.25 calibration which is suitable for capturing small forces, with a F_{xyz} resolution of 6.25 mN and T_{xyz} resolution of 31.25 mN-mm.

A.2 Displacement Sensors

To capture displacements in 2D, two orthogonal laser displacement sensors were used. With crossflow amplitudes generally larger than inline, a long-range sensor was used in crossflow and a higher resolution sensor for inline. The crossflow unit was an ILD 1402-600 from Micro-epsilon, and in inline a Panasonic HLG-112. The ILD 1402-600 had a measurement range of 600 mm, and an average resolution of 80 μm, and could sample at up to 1.5 kHz (Figure A.2). The Panasonic HL-G112 had a measurement range of 120 mm, and an average resolution of 8 μm (Figure A.3).

A.3 Flow velocity probe

To determine the airspeed for the tests of Chapter 5, a hotwire probe was used. The probe is an Omega FMA-905a, capable of measuring flow velocities up to 50.8 m/s to within 2% (Figure A.4).

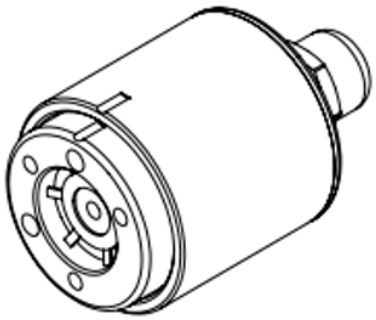

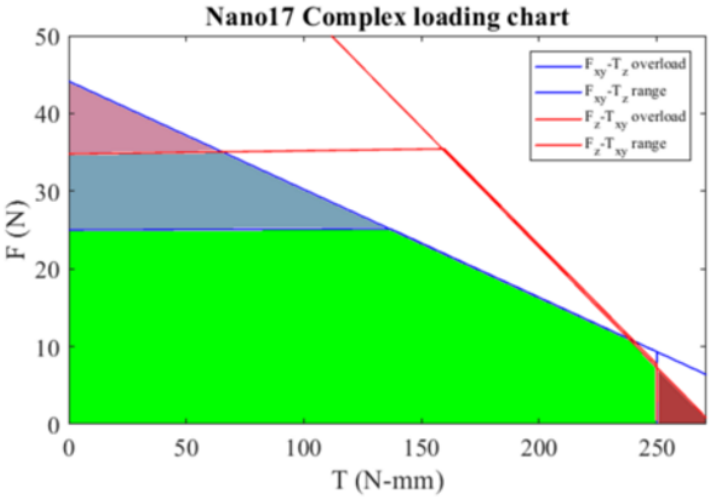

Calibration	Fx,Fy	Fz	Tx,Ty	Tz	Fx,Fy	Fz	Tx,Ty	Tz
SI-12-0.12	12 N	17 N	120 Nmm	120 Nmm	1/320 N	1/320 N	1/64 Nmm	1/64 Nmm
SI-25-0.25	25 N	35 N	250 Nmm	250 Nmm	1/160 N	1/160 N	1/32 Nmm	1/32 Nmm
SI-50-0.5	50 N	70 N	500 Nmm	500 Nmm	1/80 N	1/80 N	1/16 Nmm	1/16 Nmm
	SENSING RANGES				RESOLUTION			

Figure A.1. Specifications for the ATI Nano17/IP68 force sensor. The present thesis used an SI-25-0.25 calibration. Reproduced from ATI-IA.com

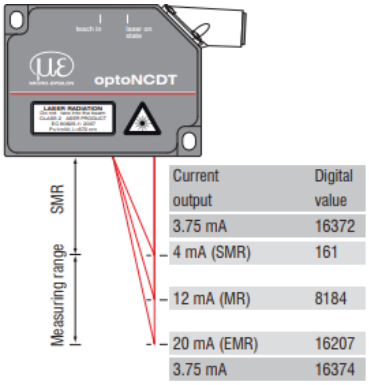

3.3 Technical Data ILD 1402-x

Model	ILD	1402-5	1402-10	1402-20	1402-50	1402-100	1402-200	1402-250VT	1402-400	1402-600
Measuring range	mm	5	10	20	50	100	200	250	400	600
Start of range	mm	20	20	30	45	50	60	100	200	200
Midrange	mm	22,5	25	40	70	100	160	225	400	500
End of range	mm	25	30	50	95	150	260	350	600	800
Linearity	µm	5 ... 9	5 ... 18	7 ... 36	12 ... 90	20 ... 180	40 ... 360	50 ... 1200	120 ... 2000	120 ... 3000
		≤ 0.18 % FSO						≤ 0.5 % FSO		
Resolution	Averaged over 64 values, µm	0.6	1	2	5	10	13	32	80	80
	dynamic, µm	1 ... 3	2 ... 5	5 ... 10	6 ... 25	12 ... 50	13 ... 100	32 ... 300	80 ... 480	80 ... 600
	1.5 kHz	0.02 ... 0.05 % FSO						0.02 ... 0.12 % FSO		
	digital	14 bit								
Measurement rate, programmable		1.5 kHz; 1 kHz; 750 Hz; 375 Hz; 50 Hz								
Light source		Semiconductor laser 1 mW, 670 nm (red)								
Laser class		Class 2 (II) acc. to IEC 60825-1: 2007								
Spot diameter	SMR, µm	110	110	210	1100	1400	2300	5000	2.6 x 5 mm	2.6 x 5 mm
	MR, µm	380	650	530	110	130	2200	5000	2.6 x 5 mm	2.6 x 5 mm
	EMR, µm	650	1200	830	1100	1400	2100	5000	2.6 x 5 mm	2.6 x 5 mm
Protection class		IP 67								
Vibration		15 g / 10 Hz ... 1 kHz						20 g / 10 Hz ... 1 kHz	15 g/ 10 Hz ... 1 kHz	
Shock		15 g / 6 ms (DIN EN 60068-2-29)								
Weight (without cable)		approx. 83 g						approx. 130 g		
Temperature stability		0.03 % FSO/°C				0.08 % FSO/°C				
Operation temperature		0 ... 50 °C								

Figure A.2. Specifications for the Micro-epsilon 1402-600 laser displacement sensor. Reproduced from micro-epsilon.pl

Model No.	Standard Type	HL-G103-A-C5	HL-G105-A-C5	HL-G108-A-C5	HL-G112-A-C5	HL-G125-A-C5
	High-function Type	HL-G103-S-J	HL-G105-S-J	HL-G108-S-J	HL-G112-S-J	HL-G125-S-J
Supply voltage		24 VDC ±10% including ripple 0.5 V (P-P)				
Current consumption		100 mA max.				
Measurement method		Diffuse reflection				
Measurement center distance		30 mm	50 mm	85 mm	120 mm	250 mm
Measurement range		±4 mm	±10 mm	±20 mm	±60 mm	±150 mm
Beam source		Red semiconductor laser Class 2 (JIS/IEC/GB/FDA laser notice No. 50) Max output: 1 mW, Emission peak wavelength: 655 nm				
Beam diameter (*1)		0.1×0.1 mm	0.5×1 mm	0.75×1.25 mm	1.0×1.5 mm	1.75×3.5 mm
Beam receiving element		CMOS image sensor				
Resolution		0.5 µm	1.5 µm	2.5 µm	8 µm	20 µm
Linearity		±0.1% F.S.				±0.3% F.S.
Temperature characteristics		±0.08% F.S./°C				
Sampling cycle		200 µs, 500 µs, 1 ms, 2 ms				
Analog output	Voltage	Output range: 0 to 10.5 V (normal), 11 V (at alarm) Output impedance: 100Ω				
	Current	Output range: 3.2 to 20.8 mA (normal), 21.6 mA (at alarm) Load impedance: 300Ω max.				

Figure A.3. Specifications for the Panasonic HL-G112 laser displacement sensor. Reproduced from panasonic.biz

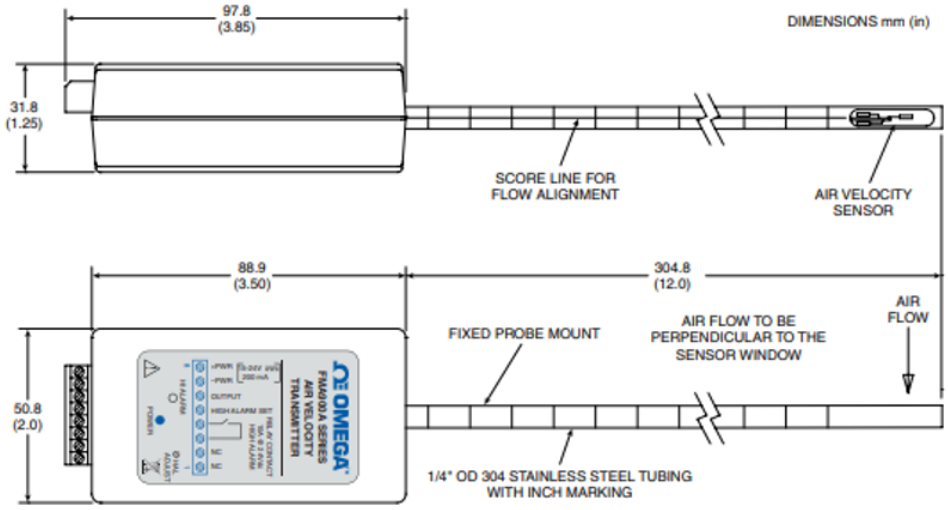

Air Velocity Range:	0 to 500 (0 to 2.54), 0 to 1000 (0 to 5.08), 0 to 2000 (0 to 10.16), 0 to 5000 (0 to 25.4), 0 to 10,000 (0 to 50.8), 0 to 12,000 (0 to 60.9) FPM (m/sec)
Accuracy:	2% of Full Scale
Sensor Probe	
Standard:	6.3 OD x 305 mm (1/4 OD x 12") – 304 Stainless Steel
Remote:	Standard probe connected via 15' of shielded cable
-S (Short Probe):	6.3 OD x 95 mm (1/4 OD x 3.75") – 304 Stainless Steel
Velocity Sensor:	One 100 ohms RTD, Two 1000 ohms RTD
Response Time:	250 msec, 0 to 90% of final value
Analog Output	
Voltage:	0 to 5 Vdc, 1K min. Load
Current:	4 to 20 mA, 400 Ohms Load Max.
High Alarm Set Point:	0 to 100% adjustable, 0 to 5 Vdc
Alarm Indication:	Red LED
Alarm Deadband:	5% of FS
Built-in Relay:	One 12V SPST NO relays
Contact Rating:	10A @ 24 Vdc, 10A @ 250 Vac (Resistive)
Operating Ambient Temperature	
Sensor Probe:	-40 to 93°C (-40 to 199°F)
Electronic Case:	0 to 50°C (32 to 122°F)
Power:	15 to 24 Vdc @ 200 mA
Power Indicator:	Green LED
Dimensions:	89 H x 51 W x 32 mm D (3.5 x 2 x 1.25")
Weight:	160 g (5.6 oz)

Figure A.4. Specifications for the Omega FMA905a hotwire probe. Reproduced from omega.com

BIBLIOGRAPHY

[1] Alawadhi, Esam M. Numerical simulation of fluid flow past an oscillating triangular cylinder in a channel. *Journal of Fluids Engineering 135*, 4 (2013), 041202.

[2] Alonso, G., and Meseguer, J. A parametric study of the galloping stability of two-dimensional triangular cross-section bodies. *Journal of Wind Engineering and Industrial Aerodynamics 94*, 4 (2006), 241 – 253.

[3] Alonso, G., Meseguer, J., and Pérez-Grande, I. Galloping instabilities of two-dimensional triangular cross-section bodies. *Experiments in Fluids 38*, 6 (Jun 2005), 789–795.

[4] Alonso, G., Sanz-Lobera, A., and Meseguer, J. Hysteresis phenomena in transverse galloping of triangular cross-section bodies. *Journal of Fluids and Structures 33* (2012), 243 – 251.

[5] Alves, D.M.C.C., Terribile, L.C., and Brito, D. The potential impact of white-nose syndrome on the conservation of North American bats. *PLoS ONE 9(9)* (2014), e107395.

[6] Arie, M., Kiya, M., Moriya, M., and Mori, H. Pressure fluctuations on the surface of two cylinders in tandem arrangement. *Journal of Fluids Engineering 105(2)* (1983), 161–166.

[7] Arnett, E.B., Hein, C.D., Schirmacher, M.R., Baker, M., Huso, M.M.P., and Szewczak, J.M. Evaluating the effectiveness of an ultrasonic acoustic deterrent for reducing bat fatalities at wind turbines. A final report submitted to the Bats and Wind Energy Cooperative. Bat Conservation International. Austin, Texas, USA., 2011.

[8] Arnett, E.B., Hein, C.D., Schirmacher, M.R., Huso, M.M.P., and Szewczak, J.M. Evaluating the effectiveness of an ultrasonic acoustic deterrent for reducing bat fatalities at wind turbines. *PLoS ONE 8(6)* (2013), e65794.

[9] Assi, G.R. Wake-induced vibration of tandem and staggered cylinders with two degrees of freedom. *Journal of Fluids and Structures 50* (2014), 340–357.

[10] Assi, G.R. Wake-induced vibration of tandem cylinders of different diameters. *Journal of Fluids and Structures 50* (2014), 329–339.

[11] Assi, G.R., Srinil, N., Freire, C.M., and Korkischko, I. Experimental investigation of the flow-induced vibration of a curved cylinder in convex and concave configurations. *Journal of Fluids and Structures 44* (2014), 55–66.

[12] A.W.E.A. U.S. wind industry annual market report year ending 2015, 2016.

[13] Bearman, P.W. Vortex Shedding from Oscillating Bluff-Bodies. *Annual Review of Fluid Mechanics 16* (1984), 195–222.

[14] Bearman, P.W., and Curie, I.G. Pressure fluctuation measurements on an oscillating circular cylinder. *Journal of Fluid Mechanics 91* (1979), 661–677.

[15] Bearman, PW, and Davies, ME. The flow about oscillating bluff structures. In *Proc. 4th Int. Conf. Wind Effects Build. Struct.* (1977), pp. 285–295.

[16] Bearman, P.W., Gartshore, I.S., Maull, D.J., and Parkinson, G.V. Experiments on flow-induced vibration of a square-section cylinder. *Journal of Fluids and Structures 1*, 1 (1987), 19 – 34.

[17] Bernard, H. Comptes rendus de l'Académie des Sciences (Paris). 839–842.

[18] Blevins, R.D. *Flow-induced vibration*, second edition ed. Hrieger Publishing Company, Malabar, Florida, 1990.

[19] Bohn, K.M., Smarsh, G., and Smotherman, M.S. Social context evokes rapid changes in bat song syntax. *Animal behavior 85* (2013), 1485–1491.

[20] Bonou, A., Laurent, A., and Olsen, S.I. Life cycle assessment of onshore and offshore wind energy-from theory to application. *Applied Energy 180* (2016), 327–337.

[21] Bourguet, R., Karniadakis, G.E., and Triantafyllou, M.S. On the validity of the independence principle applied to the vortex-induced vibrations of a flexible cylinder inclined at 60°. *Journal of Fluids and Structures 53* (2015), 58–69.

[22] Bourguet, R., Modarres-Sadeghi, Y., Karniadakis, G.E., and Triantafyllou, M.S. Wake-body resonance of long flexible structures is dominated by counter-clockwise orbits. *Physical Review Letters 107* (2011), 134502.

[23] Boyles, J.G., Cryan, P.M., McCracken, G.F., and Kunz, T.H. Economic importance of bats in agriculture. *Science 332* (2011), 41–42.

[24] Brooks, Peter Noel Hamilton. *Experimental investigation of the aeroelastic instability of bluff two-dimensional cylinders.* PhD thesis, University of British Columbia, 1960.

[25] Cagney, N., and Balabani, S. Streamwise vortex-induced vibrations of cylinders with one and two degrees of freedom. *Journal of Fluid Mechanics 758* (2014), 702–727.

[26] Cagney, N., and Balabani, S. Fluid forces acting on a cylinder undergoing streamwise vortex-induced vibrations. *Journal of Fluids and Structures 62* (2016), 147 – 155.

[27] Carlson, D.W., and Modarres-Sadeghi, Y. Flow-induced oscillations of a floating moored cylinder. *Wind Energy* (2018), 1–8.

[28] Constantinides, Y., and Oakley, O.H. Numerical prediction of bare and straked cylinder VIV. Proceedings of 25th International Conference on Offshore Mechanics and Arctic Engineering, OMAE. Hamburg, Germany, 2006.

[29] Cruz, J., and Atcheson, M. *Floating Offshore Wind Energy: The Next Generation of Wind Energy*. Springer, Switzerland, 2016.

[30] Dahl, J.M., Hover, F.S., and Triantafyllou, M.S. Two-degree-of-freedom vortex-induced vibrations using a force assisted apparatus. *Journal of Fluids and Structures 22* (2006), 807–818.

[31] Dahl, J.M., Hover, F.S., and Triantafyllou, M.S. Resonant vibrations of bluff bodies cause multivortex shedding and high frequency forces. *Physical Review Letters 99* (2007), 144503.

[32] Dahl, J.M., Hover, F.S., Triantafyllou, M.S., and Oakley, O.H. Dual resonance in vortex-induced vibrations at subcritical and supercritical Reynolds numbers. *Journal of Fluid Mechanics 643* (2010), 395–424.

[33] Dalland, J.I. Hearing sensitivity in bats. *Science 150(3700)* (1965), 1185–1186.

[34] de Vecchi, A., Sherwin, S.J., and Graham, J.M.R. Wake dynamics of external flow past a curved circular cylinder with the free-stream aligned to the plane of curvature. *Journal of Fluids and Structures 24* (2008), 1262–1270.

[35] de Vecchi, A., Sherwin, S.J., and Graham, J.M.R. Wake dynamics past a curved body of circular cross-section under forced cross-flow vibration. *Journal of Fluids and Structures 25* (2009), 721–730.

[36] Dinh, V.N., and Basu, B. Passive control of floating offshore wind turbine nacelle and spar vibrations by multiple tuned mass dampers. *Structural Control and Health Monitoring 22(1)* (2015), 152–176.

[37] Du, L., Jing, X., and Sun, X. Modes of vortex formation and transition to three-dimensionality in the wake of a freely vibrating cylinder. *Journal of Fluids and Structures 49* (2014), 554–573.

[38] Esteban, M., and Leary, D. Current developments and future prospects of offshore wind and ocean energy. *Applied Energy 90* (2012), 128–136.

[39] Every, M.J., King, R., and Weaver, D.S. Vortex-excited Vibrations of Cylinders and Cables and Their Suppression. *Ocean Engineering 9(2)* (1982), 135–157.

[40] Facchinetti, M.L., de Langre, E., and Biolley, F. Coupling of structure and wake oscillators in vortex-induced vibrations. *Journal of Fluids and Structures 19* (2004), 123–140.

[41] Feng, C.C. The measurements of vortex induced effects in flow past a stationary and oscillating circular and D-section cylinders. Master's thesis. Univ. BC, Vancouver, Can.

[42] Fitch, W. Production of vocalizations in mammals. *Visual Communication 3* (2006), 145.

[43] Gagnon, J.O., and Paidoussis, M.P. Fluid Coupling Characteristics and Vibration of Cylinder Cluster in Axial Flow. Part II: Experiments. *Journal of Fluids and Structures 8*, 3 (1994), 293–324.

[44] Goncalves, R.T., Freire, C.M., Franzini, G.R., Fujarra, A.L.C., and Meneghini, J.R. Experimental comparisons to assure the similarity between VIM (vortex-induced motion) and VIV (vortex-induced vibration) phenomena. ASME 2011 30th International Conference on Ocean, Offshore and Arctic Engineering, Rotterdam, The Netherlands, 2011.

[45] Goncalves, R.T., and Fujarra, A.L.C. Experimental study on vortex-induced vibration of floating circular cylinders with low aspect ratio. ASME 2014 33rd International Conference on Ocean, Offshore and Arctic Engineering, San Francisco, California, 2014.

[46] Gopalkrishnan, R. Vortex induced forces on oscillating bluff cylinders. Ph.D. Thesis, Department of Ocean Engineering, MIT, Cambridge, MA, USA.

[47] Govardhan, R., and Williamson, C.H.K. Modes of vortex formation and frequency response for a freely-vibrating cylinder. *Journal of Fluid Mechanics 420* (2000), 85–130.

[48] Govardhan, R., and Williamson, C.H.K. Defining the 'modified griffin plot' in vortex-induced vibration: revealing the effect of Reynolds number using controlled damping. *Journal of Fluid Mechanics 561* (2006), 147–180.

[49] Griffin, O.M., Skop, R.A., and Ramberg, S.E. The resonant vortex-excited vibrations of structures and cable systems. *7th Offshore Technology Conference, Houston TX. OTC Paper 2319* (1975).

[50] Hartlen, R.T., Baines, W.D., and Currie, I.G. Vortex-excited oscillations of a circular cylinder. *Journal of Engineering Mechanics Division ASCE 96* (1970), 577–591.

[51] Hayes, M. Bats killed in large numbers at United States wind energy facilities. *BioScience 12* (2013), 975–979.

[52] Huera-Huarte, F.J., Bangash, Z.A., and Gonzalez, L.M. Multi-mode vortex and wake-induced vibrations of a flexible cylinder in tandem arrangement. *Journal of Fluids and Structures 66* (2016), 571–588.

[53] Huera-Huarte, F.J., and Bearman, P.W. Vortex and wake-induced vibrations of a tandem arrangement of two flexible circular cylinders with near wake interference. *Journal of Fluids and Structures 27*, 2 (2011), 193–211.

[54] Huera-Huarte, F.J., and Gharib, M. Vortex and wake-induced vibrations of a tandem arrangement of two flexible circular cylinders with far wake interference. *Journal of Fluids and Structures 27*, 5-6 (2011), 824–828.

[55] Jain, A., and Modarres-Sadeghi, Y. Vortex-induced vibrations of a flexibly-mounted inclined cylinder. *Journal of Fluids and Structures 43* (2013), 28–40.

[56] Jarvis, J. Ph.D thesis, Texas A&M University.

[57] Jarvis, J., Bohn, K.M., and Smotherman, M.S. A mechanism for antiphonal echolocation by Free-tailed bats. *Animal behavior 79(4)* (2010), 787–796.

[58] Jarvis, J., Jackson, W., and Smotherman, M.S. Groups of bats improve sonar efficiency through mutual suppression of pulse emissions. *Frontiers in Physiology 4* (2013), 140.

[59] Jauvtis, N., and Williamson, C.H.K. The effect of two degrees of freedom on vortex-induced vibration at low mass and damping. *Journal of Fluid Mechanics 509* (2004), 23–62.

[60] Jhingran, V., and Vandiver, J.K. Incorporating the higher harmonics in VIV fatigue predictions. *26th International Conference on Offshore Mechanics and Arctic Engineering.* (2007), 891–899.

[61] Jonkman, J., and Laboratory, National Renewable Energy. Definition of the floating system for phase IV of OC3, 2010.

[62] Jonkman, J.M. Dynamics of offshore floating wind turbines—model development and verification. *Wind Energy 12(5)* (2009), 459–492.

[63] Jonkman, J.M., and Matha, D. Dynamics of offshore floating wind turbines—analysis of three concepts. *Wind Energy 14(4)* (2011), 557–569.

[64] Khalak, A., and Williamson, C.H.K. Investigation of the relative effects of mass and damping in vortex-induced vibration of a circular cylinder. *Journal of Wind Engineering and Industrial Aerodynamics 69-71* (1997), 341–350.

[65] Khalak, A., and Williamson, C.H.K. Motions, forces and mode transitions in vortex-induced vibrations at low mass-damping. *Journal of Fluids and Structures 13* (1999), 813–851.

[66] Kobayasi, K.I., Hage, S.R., Berquist, S., Feng, J., Zhang, S., and Metzner, W. Behavioral and neurobiological implications of linear and non-linear features in larynx phonations of horseshoe bats. *Nature Communications 3* (2012), 1184.

[67] Lienhard, J.H. Synopsis of lift, drag and vortex frequency data for rigid circular cylinders. *Washinton State University, College of Engineering. Research Division Bulletin 300.* (1966).

[68] Ltd., Xodus Group. Hywind Scotland pilot park project: Environmental impact assessment scoping report. Document number: A-100142-S00-REPT-001., 2013.

[69] Miliou, A., Sherwin, S.J., and Graham, J.M.R. Fluid dyanmic loading on curved riser pipes. *Journal of Offshore Mechanics and Arctic Engineering 125* (2003), 176–182.

[70] Mittal, S., and Kumar, V. Finite element study of vortex-induced cross-flow and in-line oscillations of a circular cylinder at low reynolds numbers. *International Journal for Numerical Methods in Fluids 31*, 7 (1999), 1087–1120.

[71] Modarres-Sadeghi, Y., Chasparis, F., Triantafyllou, M.S., Tognarelli, P., and Beynet, P. Chaotic response is a generic feature of vortex-induced vibrations of flexible risers. *Journal of Sound and Vibration 330* (2011), 2565–2579.

[72] Modarres-Sadeghi, Y., Hover, F.S., and Triantafyllou, M.S. Fatigue calculation of risers using a van der pol wake oscillator model with random parameters. *International Conference on Offshore Mechanics and Arctic Engineering 5*, 757-763 (2008).

[73] Modarres-Sadeghi, Y., Mukundan, H., Dahl, J.M., Hover, F.S., and Triantafyllou, M.S. The effect of higher harmonic forces on fatigue life of marine risers. *Journal of Sound and Vibration 329* (2010), 43–55.

[74] Myhr, A., Bjerkseter, C., Agotnes, A., and Nygaard, T.A. Levelised cost of energy for offshore floating turbines in a life cycle perspective. *Renewable Energy 66* (2014), 714–728.

[75] Nemes, András, Zhao, Jisheng, Jacono, David Lo, and Sheridan, John. The interaction between flow-induced vibration mechanisms of a square cylinder with varying angles of attack. *Journal of Fluid Mechanics 710* (2012), 102–130.

[76] Obrist, M.K., and Wenstrup, J.J. Hearing and hunting in red bats (Lasiurus borealis, Vespertilionidae): audiogram and ear properties. *Journal of Experimental Biology 201* (1998), 143–154.

[77] Paidoussis, M.P. *Slender structure and axial flow.* Academic Press, London, 1998.

[78] Paidoussis, M.P., Price, S.J., and Mark, B. Current-induced oscillations and instabilities of a multi-tube flexible riser. *Journal of Fluids and Structures 2*, 5 (1988), 503–513.

[79] Parkinson, Geoffrey. Phenomena and modelling of flow-induced vibrations of bluff bodies. *Progress in Aerospace Sciences 26*, 2 (1989), 169–224.

[80] Parkinson, GV, and Smith, JD. The square prism as an aeroelastic non-linear oscillator. *The Quarterly Journal of Mechanics and Applied Mathematics 17*, 2 (1964), 225–239.

[81] Reynolds, Osborne. An experimental investigation of the circumstances which determine whether the motion of water shall be direct or sinuous, and of the law of resistance in parallel channels. *Philosophical Transactions of the Royal Society 174* (1883), 935–982.

[82] Roshko, A. On the wake and drag of bluff bodies. *Journal of Aeronautical Science 22* (1955), 124–135.

[83] Sarpkaya, T. Fluid forces on oscillating cylinders. *Journal of Waterway Port Coastal and Ocean Division 104* (1978), 275–290.

[84] Sarpkaya, T. Vortex-induced oscillations, a selective review. *Journal of Applied Mechanics 46* (1979), 241–258.

[85] Sarpkaya, T. Hydrodynamic damping, flow-induced oscillations and biharmonic response. *Offshore Mechanics and Arctic Enginering 117* (1995), 232–238.

[86] Sarpkaya, T. A critical review of the intrinsic nature of vortex-induced vibrations. *Journal of Fluids and Structures 19* (2004), 389–447.

[87] Sarpkaya, Turgut. Transverse oscillations of a circular cylinder in uniform flow, part 1. revised. Tech. rep., NAVAL POSTGRADUATE SCHOOL MONTEREY CA, 1977.

[88] Sarpkaya, Turgut. Fluid forces on oscillating cylinders. *Nasa Sti/recon Technical Report A 78* (1978), 275–290.

[89] Seyed-Aghazadeh, B., Budz, C., and Modarres-Sadeghi, Y. The influence of higher harmonic flow forces on the response of a curved circular cylinder undergoing vortex-induced vibration. *Journal of Sound and Vibration 353* (2015), 395–406.

[90] Seyed-Aghazadeh, B., Carlson, D.W., and Modarres-Sadeghi, Y. The influence of taper ratio on vortex-induced vibrations of tapered cylinders in the crossflow direction. *Journal of Fluids and Structures 53* (2015), 84–95.

[91] Seyed-Aghazadeh, B., Carlson, D.W., and Modarres-Sadeghi, Y. Vortex-induced vibration and galloping of prisms with triangular cross-sections placed in water flow. *Journal of Fluid Mechanics 817* (2017), 590–618.

[92] Seyed-Aghazadeh, B., and Modarres-Sadeghi, Y. Reconstructing the vortex-induced-vibration response of flexible cylinders using limited localized measurement points. *Journal of Fluids and Structures 65* (2016), 433–446.

[93] Skop, R.A. On modelling vortex-excited oscillations. *NRL Memo. Rep. 2927* (1974).

[94] Skop, R.A., and Griffin, O.M. An heuristic model for determining flow-induced vibrations of offshore structures. *Offshore Technology Conference, Houston, TX, OTC Paper 1843* (1973).

[95] Smith, A., Stehly, T., Musial, W., and Laboratory, National Renewable Energy. 2014-2015 Offshore wind technologies market report, 2015.

[96] Song, Y., and Perot, J.B. CFD Simulation of the NREL Phase VI Rotor. *Wind Engineering 39* (2015), 299–310.

[97] Staino, A., and Baseu, B. Dynamics and control of vibrations in wind turbines with variable rotor speed. *Engineering Structures 56* (2013), 58–67.

[98] Strouhal, V. Ueber eine besondere art der tonerregung. *Annalen der Physik und Chemie 5(10)* (1878), 216–251.

[99] Surry, J., and Surry, D. The effect on inclination on the Strouhal number and other wake properties of circular cylinders at subcritical Reynolds numbers. *Institute for Aerospace Studies, University of Toronto* (1967).

[100] Suthers, R.A., and Fattu, J.M. Mechanisms of sound production by echolocating bats. *American Zoology 13* (1973), 1215–1226.

[101] Suthers, R.A., Narins, P.M., Lin, W., Schnitzler, H., Denzinger, A., Xu, C., and Feng, A.S. Voices of the dead: complex nonlinear vocal signals from the larynx of an ultrasonic frog. *Journal of Experimental Biology 209* (2006), 4984–4993.

[102] Takamoto, M., and Izumi, K. Experimental observation of stable arrangement of vortex rings. *Physics of Fluids 24* (1981), 1582–1583.

[103] Tian, Q., Corson, D., and Baker, J. Application of vortex generators to wind turbine blades. *Frontier Wind 34th Wind Energy Symposium San Diego, California, USA.* (2016).

[104] Tong, K.C. Technical and economic aspects of a floating offshore wind farm. *Journal of Wind Engineering and Industrial Aerodynamics 74-76* (1998), 399–410.

[105] Tressler, J., and Smotherman, M.S. Context-dependent effects of noise on echolocation pulse characteristics in free-tailed bats. *Journal of Comparative Physiology A. 195(10)* (2009), 923–934.

[106] van der Veen, D.J., Couchman, I.J., and Bowyer, R.O. Control of floating wind turbines. *American Control Conference, Fair Mont Queen Elizabeth June 27 - June 29* (2012).

[107] van Rooij, R.P.J.O.M., and Timmer, W.A. Roughness sensitivity considerations for thick rotor blade airfoils. *ASME Journal of Solar Engineering 125* (2003), 468–478.

[108] Vandiver, J.K. Dimensionless parameters important to the prediction of vortex-induced vibration of long, flexible cylinders in ocean currents. *Journal of Fluids and Structures 7* (1993), 423–455.

[109] Vandiver, J.K., Jaiswal, V., and Jhingran, V. Insights on vortex-induced, traveling waves on long risers. *Journal of Fluids and Structures 25* (2009), 641–653.

[110] Vandiver, J.K., Swithenbank, S., and Jaiswal, V. The effectiveness of helical strakes in the suppression of high mode number VIV. *Offshore Technology Conference, Houston, TX, OTC Paper No. 18276.* (2006).

[111] von Karman, T. Nachr. Ges. Wissenschaft. Göttingen Math. Phys. Klasse. 547–556.

[112] Weller, Henry G, Tabor, Gavin, Jasak, Hrvoje, and Fureby, Christer. A tensorial approach to computational continuum mechanics using object-oriented techniques. *Computers in physics 12*, 6 (1998), 620–631.

[113] Williamson, C.H.K., and Govardhan, R. Vortex-Induced Vibrations. *Annual Review of Fluid Mechanics 36* (2004), 413–455.

[114] Williamson, C.H.K., and Jauvtis, N. A high-amplitude 2t mode of vortex-induced vibration for a light body in XY motion. *European Journal of Fluid Mechanics 23* (2004), 107–114.

[115] Williamson, C.H.K., and Roshko, A. Vortex formation in the wake of an oscillating cylinder. *Journal of Fluids and Structures 2* (1988), 355–381.

[116] Zdravkovich, M.M. Review and classification of various aerodynamic and hydrodynamic means for suppressing vortex shedding. *Journal of Wind Engineering and Industrial Aerodynamics 7(2)* (1981), 145–189.

[117] Zdravkovich, M.M. The effects of interference between circular cylinders in cross flow. *Journal of Fluids and Structures 1*, 2 (1987), 239–261.

[118] Zhao, J., Hourigan, K., and Thompson, M. C. Flow-induced vibration of d-section cylinders: an afterbody is not essential for vortex-induced vibration. *Journal of Fluid Mechanics 851* (2018), 317–343.

[119] Zhao, Jisheng, Leontini, Justin S., Lo Jacono, David, and Sheridan, John. Fluid–structure interaction of a square cylinder at different angles of attack. *Journal of Fluid Mechanics 747* (2014), 688–721.

[120] Zhao, Jisheng, Nemes, Andras, Jacono, D Lo, and Sheridan, John. The effect of incidence angle variation of a square cylinder on its dynamic response and wake states. In *Proceedings of the 17th Australasian Fluid Mechanics Conference* (2010), AFMC Auckland, New Zealand, pp. 724–727.

[121] Zhao, M., Cheng, L., and Zhou, T. Direct numerical simulation of three-dimensional flow past a yawed circular cylinder of infinite length. *Journal of Fluids and Structures 25* (2009), 831–847.

[122] Zhao, Ming. Flow-induced vibrations of square and rectangular cylinders at low reynolds number. *Fluid Dynamics Research 47*, 2 (2015), 025502.

[123] Zhao, Ming, Cheng, Liang, and Zhou, Tongming. Numerical simulation of vortex-induced vibration of a square cylinder at a low reynolds number. *Physics of Fluids 25*, 2 (2013), 023603.